Master's thesis

NTNU
Norwegian University of Science and Technology
Faculty of Natural Sciences
Department of Physics

André konarboland

Coherent Anti-Stokes Raman Scattering (CARS) microscopy of calcium phosphate minerals and bone samples

Master's thesis in MTNANO
Supervisor: Pawel Sikorski
Co-supervisor: Astrid Bjørkøy
June 2024

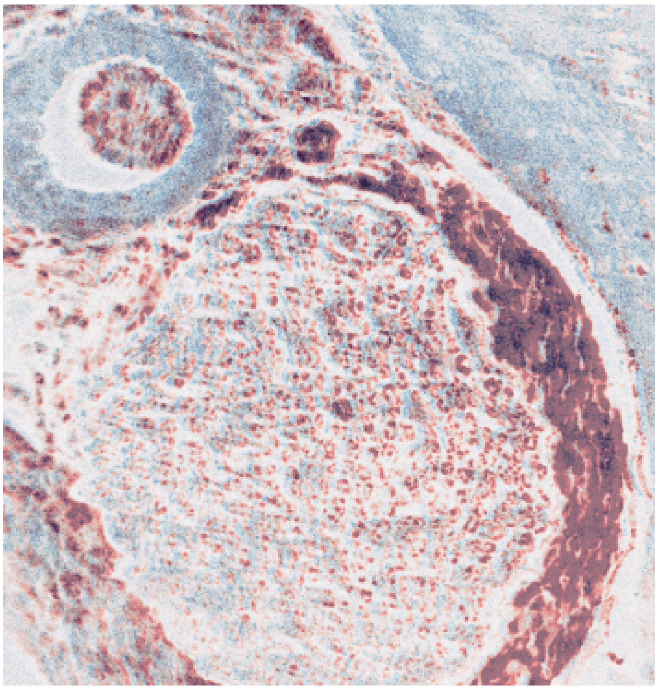

NTNU
Norwegian University of
Science and Technology

André konarboland

Coherent Anti-Stokes Raman Scattering (CARS) microscopy of calcium phosphate minerals and bone samples

Master’s thesis in MTNANO
Supervisor: Pawel Sikorski
Co-supervisor: Astrid Bjørkøy
June 2024

Norwegian University of Science and Technology
Faculty of Natural Sciences
Department of Physics

NTNU
Norwegian University of
Science and Technology

ABSTRACT

Bone is an an essential and multifunctional organ, but, due to an an ageing population, there has been an increase in diseases such as osteoporosis or similar conditions. There is therefore a need for further study of the nanoscale processes in bone mineralization, so that we can use our understanding of these to further the development of tissue engineering aimed at healing bone diseases. Unfortunately, the current methods for studying bone samples have some major disadvantages, being either time consuming and/or requiring chemical labelling that permanently alters the sample. New techniques for the study of bone samples is therefore desirable. One technique that shows promise is Coherent Anti-Stokes Raman Scattering (CARS) spectroscopy, a two laser microscopy technique based on Raman active vibrational modes of molecules, that allows for real-time imaging at a high spatial resolution. In this technique, the signal is generated by photons that undergoes anti-Stokes Raman scattering when interacting with a molecule. The goal of this master's thesis was therefore to see if CARS spectroscopy could be used for imaging of bone samples.

Imaging was done on multiple different samples. This was done by collecting anti-Stokes photons with particular wavelengths that corresponded to a particular vibration primarily from hydroxyapatite in the samples, though images were also collected using photons generated from the CH-bonds vibrations. From the resulting images, it was found that samples between 5-20 µm were imaged without problem using the CARS microscopy when looking at spongy/trabecular bone or structures such as nerve bundles and arterioles. When trying to image cortical bone, or samples of much higher thickness, the signal strength, and therefore the image quality, became noticeably worse. It was also shown that CARS signals from different Raman shifts could be used to differentiate between different types of tissue. This was done by comparing the signals from hydroxyapatite and CH vibrations.

When looking at the CARS signal from hydroxyapatite, the signal strength as a function of the delay between the pulses of the two lasers, as well as the signal strength as a function of the probed vibration frequency, were collected from multiple samples. Similar spectra were made for the signal strength from the CH-bonds vibrations. Results obtained using CARS were also compared with Raman spectra collected using Raman spectroscopy.

SAMMENDRAG

Bein er et viktig og multifunksjonelt organ, men på grunn av en aldrende befolkning har det vært en økning i sykdommer som osteoporose eller lignende tilstander. Det er derfor behov for videre studier av nanoskalaprosessene i beinmineralisering, slik at vi kan bruke vår forståelse av disse til å videreutvikle vevsteknikk rettet mot å helbrede beinsykdommer. Dessverre har dagens metoder for å studere beinprøver noen store ulemper. De er enten tidkrevende og/eller krever kjemisk merking som permanent endrer prøven. Nye teknikker som kan brukest til å studere beinprøver er derfor ønskelige. En teknikk som viser seg lovende er Koherent Anti-Stokes Raman Spredning (CARS) spektroskopi, en to lasermikroskopiteknikk basert på Raman aktive vibrasjonsmoduser i molekyler, som muliggjør sanntidsavbildning med høy romlig oppløsning. I denne teknikken genereres signalet fra fotoner som gjennomgår anti-Stokes Raman-spredning når de interagerer med et molekyl. Målet med denne masteroppgaven var derfor å se om CARS-spektroskopi kunne brukes til avbildning av beinprøver.

Avbildning ble gjort på flere ulike prøver. Dette ble gjort ved å samle anti-Stokes fotoner med spesifikke bølgelengder som tilsvarte en bestemt vibrasjon, primært fra hydroksyapatitt i prøvene, selv om avbildning også ble oppnådd ved bruk av fotoner generert fra CH-bindingsvibrasjonene. Fra de resulterende bildene ble det funnet at prøver mellom 5-20 µm ble avbildet uten problemer ved bruk av CARS-mikroskopi når man så på svampete/trabekulære bein, eller på strukturer som nervebunter og arterioler. Når man prøver å avbilde kortikalt bein, eller prøver med mye høyere tykkelse, ble signalstyrken, og dermed bildekvaliteten, merkbart dårligere. Det ble også vist at CARS-signaler fra ulike Raman-skift kunne brukes til å skille mellom ulike typer vev. Dette ble gjort ved å sammenligne signalene fra hydroksyapatitt og CH-vibrasjoner.

Når man så på CARS-signalet fra hydroksyapatitt, ble signalstyrken som en funksjon av forsinkelsen mellom pulsene til de to laserne, så vel som signalstyrken som en funksjon av den sonderte vibrasjonsfrekvensen, samlet inn fra flere prøver. Lignende spektre ble laget for signalstyrken fra CH-bindingsvibrasjonene. Resultater oppnådd ved bruk av CARS ble også sammenlignet med Raman-spektre samlet ved bruk av Raman spektroskopi.

PREFACE

The research presented in this master's thesis was conducted in the Department of Physics at the Faculty of Natural Sciences of the Norwegian University of Science and Technology (NTNU). It was done under the supervision of Pawel Sikorski, and co-supervised by Astrid Bjørkøy. I would like to thank them both for their continued guidance during the master's. I would also like to thank Catherine A. Heyward and Hanna Tiainen from the University of Oslo's Faculty of Dentistry for providing me with bone and tooth samples, and thank Marie Eline Ullevålseter from NTNU's Faculty of Natural Sciences for preparing bone cell samples for me. Lastly, I want to thank Johannes Ofstad for the help operating the Raman spectroscope used during the master's.

As this master's thesis is an continuation of the author's specialisation project (TFY4520) [1], certain parts are adapted from this project. This includes the first paragraph of the abstract, parts of the Introduction, parts of 2.1-2.5 and 2.12 from Background and Theory, and parts of Material and Methods. Some parts are taken verbatim, while others has been changed. If any results were taken from the specialisation project, this is disclosed in the text.

All images used in this thesis not made by the author are either distributed under the Creative Commons license, or the author have been given explicit permission to use the image through Copyright Clearance Center, Inc. (see Appendix C).

André Konarboland

André Konarboland
June 17, 2024

CONTENTS

LIST OF FIGURES

LIST OF TABLES

ABBREVIATIONS

List of all abbreviations in alphabetic order:

- **ARS** Alizarin Red S
- **CARS** Coherent Anti-Stokes Raman Scattering
- **CRM** Confocal Raman Microscope
- **DCPD** Dicalcium Phosphate Dihydrate
- **HAp** Hydroxyapatite
- **MMA** Methyl Methacrylate
- **PDL** Peridontal Ligament
- **PMMA** Polymethyl Methacrylate
- **SRS** Stimulated Raman Scattering
- **µRS** Micro-Raman Spectroscope

CHAPTER
ONE

INTRODUCTION

Bone is an essential and multifunctional organ, important not only in bearing the weight of the body and assisting in its locomotion, but also for its biological roles such as the physical protection of vital organs like brain or heart, the generation of blood cells, and the storage of minerals and growth factors [2]. Unfortunately, due to the ageing of the population, there has been an increase in diseases such as osteoporosis or similar conditions. Osteoporosis is characterised by low bone mineral density and structural deterioration of bone tissue, leading to an increased risk of fractures. There is also a general lack of understanding for other bone diseases, such as Paget's disease, as many of them either are underdiagnosed, or occurs as complications for other conditions, and thus are not counted separately. [3, 4]

There is therefore a need to study the nanoscale processes in bone mineralization in order to increase our understanding of them, and from there be able to use this knowledge to further the development of tissue engineering aimed at healing bone diseases. The current methods for studying bone samples unfortunately have some major disadvantages. Many of them are either time consuming, requires the use of chemical labels, meaning the samples are permanently altered, or both. Finding new methods which are both fast and doesn't require chemical labels are therefore desirable.

A solution to this problem might be the use of coherent Raman microscopy techniques, which allows for chemical label-free optical imaging [5]. One of these techniques is Coherent Anti-Stokes Raman Scattering (CARS) spectroscopy, a nonlinear process that involves the use of two lasers with different wavelengths. Other than allowing for label-free study of molecules, CARS also allows for real time imaging at a high spatial resolution. [6]

Bone can be split up into an organic and inorganic portion. The organic component primarily consists of collagen, and constitute approximately 30% bone weight. The inorganic component is primarily composed of hydroxyapatite (HAp), a calcium phosphate mineral with the formula $Ca_5(PO_4)_3(OH)$. Up to 40% of the volume and 60% of the weight of human bone is made up of HAp crystals interspersed in a matrix of collagen. [7, 8, 9]

Many different bone samples are here studied, including fully grown animal bone tissue (both normal and decalcified), bone marrow biopsied, cultured pre-osteoblast samples, as well as tooth sections, as teeth has a similar tissue structure to bone. The study of hydroxyapatite in bone using CARS is the main focus, but the organic component is also studied as well. All samples were also studied using Micro-Raman spectroscopy, in order to compare the results collected with those obtained using the CARS technique. The end goal of this master's thesis is to see if it is possible to study bone samples using the CARS technique through both imaging and signal analysis, and if so, to find the optimal settings and circumstances for this procedure.

CHAPTER

TWO

BACKGROUND AND THEORY

2.1 Spectroscopy

Spectroscopy is the study of the interactions between matter and electromagnetic radiation. Furthermore, a distinction can be made between absorption, reflection, scattering and luminescence/emission spectroscopy. The essential principle of spectroscopy is that atoms and molecules only are able to absorb or emit light at specific wavelengths. [10]

2.1.1 Electromagnetic Radiation

There are two ways to describe electromagnetic radiation, either the classical or quantum mechanical description. The classical description considers electromagnetic radiation to be a transverse wave, where the oscillating electric and magnetic field, as well as the propagation direction, all are perpendicular to each other. In the quantum mechanical description, electromagnetic radiation is instead described as quantized packets of energy called photons. Both of these descriptions are necessary in order to understand electromagnetic radiation to its fullest. [11] All forms of electromagnetic radiation is characterised by their frequency, and hence their wavelength, and their energy. According to Einstein, the energy of electromagnetic radiation, E, is proportional to the frequency, f, i.e. $E \sim f$. Using the proportionality constant $h = 6.626 \times 10^{-34} Js$, one can obtain the equation

$$E = hf \tag{2.1}$$

In a vacuum, the propagation velocity of electromagnetic radiation is constant ($c = 2997925 \pm 3$ m/s), which means the wavelength and frequency are correlated according to the equations

$$f = \frac{c}{\lambda} \tag{2.2}$$

and

$$E = h\frac{c}{\lambda} \tag{2.3}$$

where λ is the wavelength of the electromagnetic radiation. This can further be used to express the energy of electromagnetic radiation as a reciprocal length, which is referred to as the wavenumber. There are two ways to define wavenumber. In theoretical physics, it is defined as the number of radians per unit distance, and can be found using equation:

$$k = \frac{2\pi}{\lambda} \tag{2.4}$$

In spectroscopy, it is however defined as the number of wavelengths per unit distance, and can be found using equation:

$$\bar{v} = \frac{1}{\lambda}. \tag{2.5}$$

[12]

2.1.2 Types of Spectroscopy

There are many different types of spectroscopy techniques. Broadly speaking, they can be divided based on what type of interaction happens between matter and electromagnetic radiation, or at which region of the electromagnetic spectrum the radiation generated and/or detected finds itself. When looking at interactions, the different techniques can furthermore be divided up into two new categories; those involving energy transfer between matter and electromagnetic radiation, and those which do not involve energy transfer. Different energy-transferring interactions include absorption, emission, photoluminescence and chemiluminescence. Non-energy transferring interactions include diffraction, refraction, scattering and dispersion. Of course, not all techniques can be neatly divided based on their interaction. For example, while Raman spectroscopy occurs because of *absorption* of energy by molecules from electromagnetic radiation, what is measured is *scattered* photons *emitted* by the molecules. Because of this, only the first interaction is considered when dividing the different techniques in Table 2.1.1. When dividing based on the region of the electromagnetic spectrum, it could be tempting to divide the different spectroscopy techniques based solely on the type of electromagnetic radiation which is generated/detected (X-ray, infrared etc.). However, since many different spectroscopy techniques span multiple types of electromagnetic radiation, like how UV/VIS spectroscopy spans both ultraviolet and visible light, it is easier to just look at the usual wavelength range, which is done in Table 2.1.2. [13, 14]

2.1.3 Basic Components of Spectroscopic Instruments

All spectroscopic techniques in Table 2.1.1 and Table 2.1.2 use instruments that share several basic components. These include: [14]

- **Source of Energy**: The source of electromagnetic radiation used to promote the analyte to a suitable excited state. Can be classified as either continuum (emits radiation over a broad range of wavelengths) or line (emits radiation at selected wavelengths) sources.
- **Detector**: Used to measure the signal emitted or scattered from the sample.
- **Wavelength Selector**: A way to isolate a narrow range of wavelengths. Used for narrowing both the range of radiation from the source that radiates

Table 2.1.1: Different spectroscopy techniques divided based on the first type of interaction happening between matter and electromagnetic radiation.

Type of Interaction	Energy Transfer	Spectroscopy Techniques
Absorption	Yes	Mossbauer spectroscopy, X-ray absorption spectroscopy, UV/Vis spectroscopy, atomic absorption spectroscopy, infrared spectroscopy, raman spectroscopy, microwave spectroscopy, electron spin resonance spectroscopy, nuclear magnetic resonance spectroscopy
Emission	Yes	Atomic emission spectroscopy
Photoluminescence	Yes	Fluorescence spectroscopy, phosphorescence spectroscopy, atomic fluorescence spectroscopy
Chemiluminescence	Yes	Chemiluminescence spectroscopy
Diffraction	No	X-ray diffraction
Refraction	No	Refractometry
Scattering	No	Nephelometry, turbidimetry
Dispersion	No	Optical rotary dispersion

Table 2.1.2: Different spectroscopy techniques divided based on the usual wavelength range of radiation generated and/or detected using the technique.

Type of Spectroscopy	Usual Wavelength Range
Gamma-ray emission	0.005-1.4 Å
X-ray absorption, emission, fluorescence and diffraction	0.1-100 Å
Vacuum ultraviolet absorption	10-180 nm
Ultraviolet-visible absorption, emission and fluorescence	180-780 nm
Infrared absorption and Raman scattering	0.78-300 µm
Microwave absorption	0.75-375 mm
Electron spin resonance	3 cm
Nuclear magnetic resonance	0.6-10 m

the sample, and the range of radiation emitted or scattered from the sample that reaches the detector. It is impossible to isolate a single wavelength of radiation from a continuum source (can only isolate a narrow gap), so some unwanted radiation will be able to pass through both selectors. That is why its important to select for both the radiation that radiates the sample, and the radiation that is detected by the detector. The selector usually works either by absorbing light of certain wavelengths (absorption filter) or by reflecting light of certain wavelengths (dichroic filter). One can also used either a diffraction grating or a prism as a filter. How this works is that the diffraction grating/prism disperses the radiation through either diffraction or refraction [15]. Focusing mirrors and slits are then be used in order to make sure that only the radiation with the wanted wavelengths makes it to the sample/detector.

- **Signal processor**: Processes the signal through e.g. noise filtering, signal amplification or mathematical transformation, and then displays the signal in a way more suitable for analysis.

See figure Figure 2.2.1 for a schematic of a basic spectroscopic instrument.

2.2 Raman Spectroscopy

Raman spectroscopy is an analytical technique where scattered light, caused by interactions between a molecule and radiation in the near infrared or visible range, is used to measure the vibrational energy modes of a sample. [16, 17]

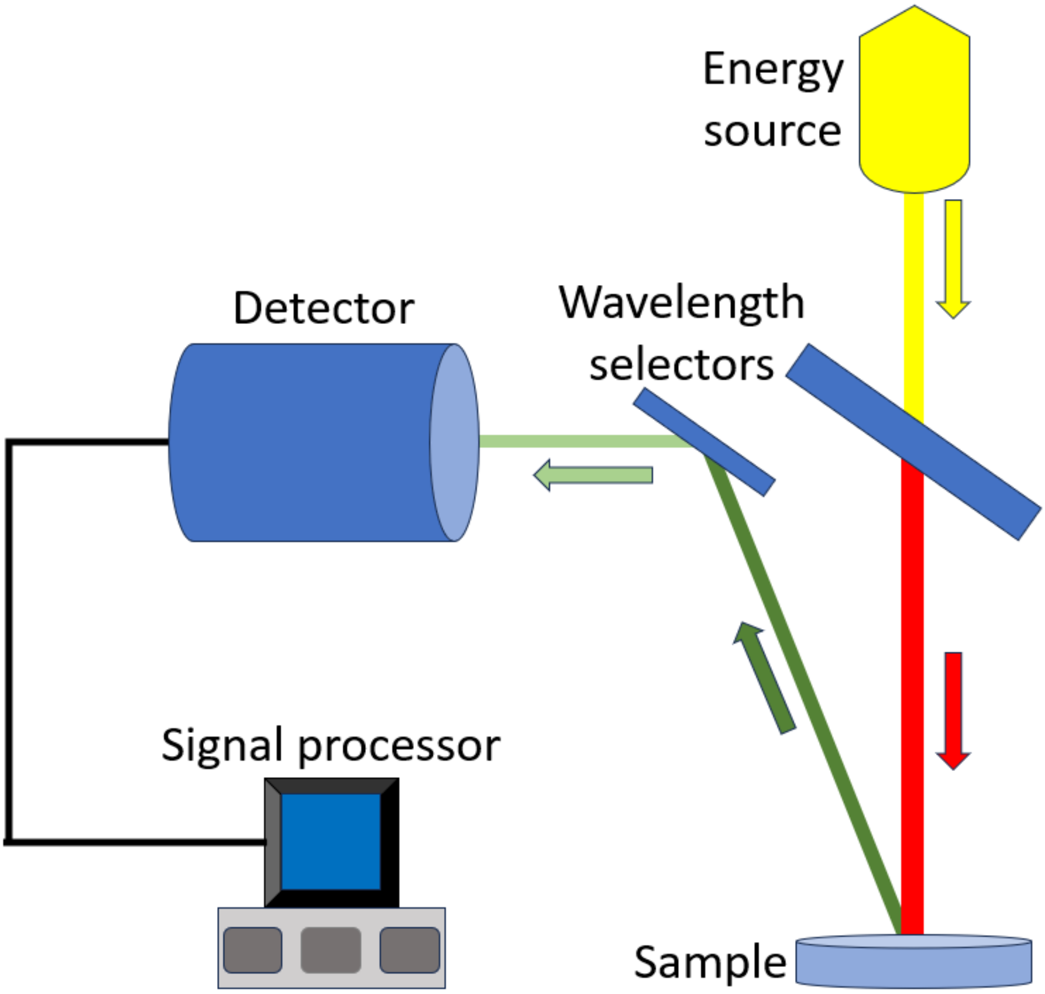

Figure 2.2.1: Schematic of a basic spectroscopic instrument.

A vibrational mode, also known as a normal mode of vibration, is a molecular vibration where some or all atoms in a molecule vibrate together in the same frequency. An example of this can be seen Figure 2.2.2, where the different normal modes of vibration in a water molecule are shown. This vibration occurs without causing movement to any of the other modes, and has itself no components originating from other modes. The number of vibrational modes in a molecule is equal to the number of vibrational degrees of freedom,

$$3N - 6 \tag{2.6}$$

for a molecule with a nonlinear shape, where N is the number of atoms in the molecule, and

$$3N - 5 \tag{2.7}$$

for a linear molecule. [18, 19]

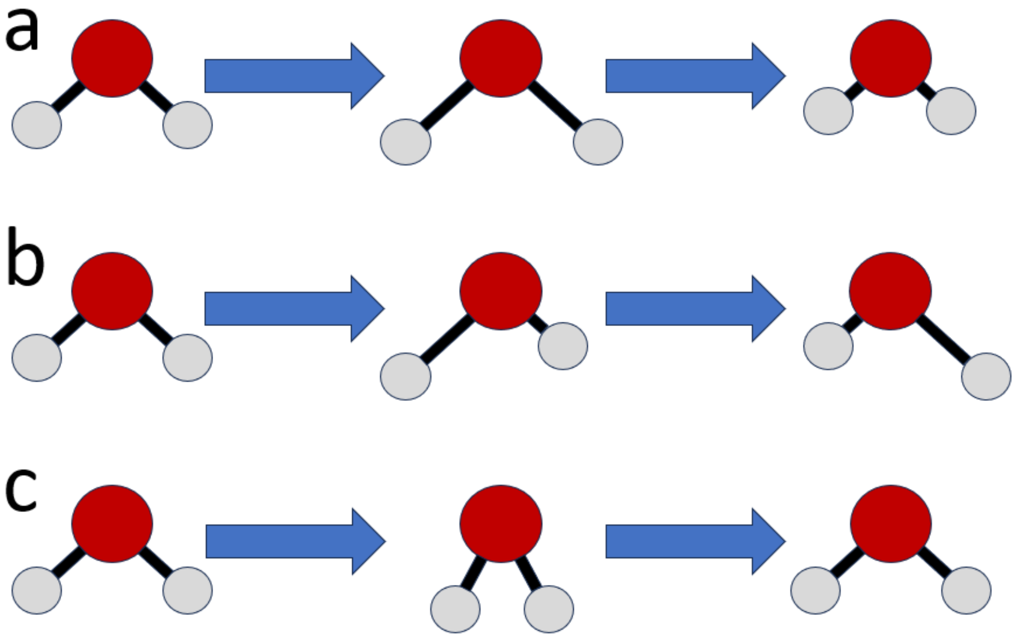

Figure 2.2.2: The three normal modes of vibration of a water molecule: (a) Symmetric stretching, (b) asymmetric stretching, (c) bending.

To explain exactly what vibrational energy levels are, one first has to explain the concept of harmonic oscillators. In classical mechanics, this is a system that, when displaced from equilibrium, experiences a restoring force F proportional to its displacement from the equilibrium position. In one dimension, this would then be:

$$F = -kx \tag{2.8}$$

where k is a positive constant and x is the displacement from equilibrium. By applying Newton's second law (net force is equal to mass times acceleration), one can find the elastic potential energy of a harmonic oscillator, which is given by

$$U(x) = \frac{1}{2}kx^2 \tag{2.9}$$

which when plotted has the shape of a parabola, as shown in Figure 2.2.3. The motion of the harmonic oscillation takes place between $x = \pm A$, where A denotes the amplitude of the motion. For such an idealised system, $E_{tot} = E_k + U(x) =$ constant, $E_{tot} \propto A$, and when $x = 0$ the potential energy of the system equals zero. In quantum mechanics, the potential energy of a system can be approximated as a harmonic potential when close to the equilibrium point. By applying the Scrödinger equation to the one-dimensional harmonic oscillator, one get equation:

$$E_n = (n + \frac{1}{2})hf \tag{2.10}$$

which describes an approximation to the energy levels in a molecule. Here, n is the energy state, h is Planc's constant, and f is the frequency of vibration. At the lowest energy state, $E_0 = \frac{1}{2}hf$, meaning the system is always oscillating (always has kinetic energy). A very important detail is that the amplitude now no longer can take any value, as only some oscillations are allowed in this system. This is what gives the different separated energy levels (see Figure 2.2.3). While this is a decent approximation, bonds in a molecule do not behave like they would do if they truly followed harmonic oscillation. For example will atoms that are too far apart dissociate, unlike the parabola given in the harmonic oscillator approximation. By adding anharmonic perturbations to the harmonic oscillator, which is to say expanding Equation 2.9 as a Taylor series:

$$\begin{aligned} U(x) = U(x_0) + \left.\frac{dV(x)}{dx}\right|_{x_0}^{x} (x - x_0) + \frac{1}{2!}\left.\frac{d^2V(x)}{dx^2}\right|_{x_0}^{x} (x - x_0)^2 \\ + \ldots + \frac{1}{n!}\left.\frac{d^nV(x)}{dx^n}\right|_{x_0}^{x} (x - x_0)^n \end{aligned} \tag{2.11}$$

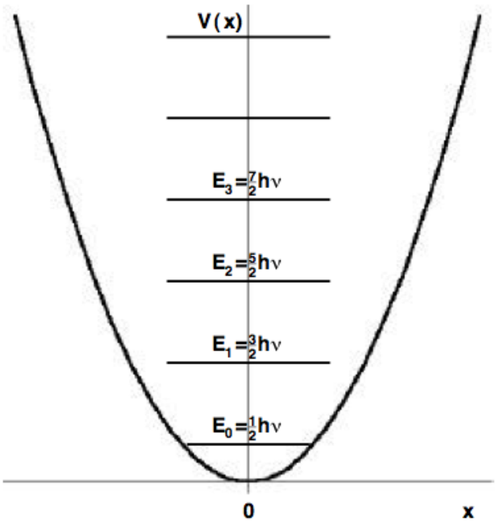

Figure 2.2.3: Potential energy function and first few energy levels for harmonic oscillator. (CC BY-NC; Seymour Blinder via LibreTexts)

one better describes molecular vibrations. Anharmonic oscillation is defined as the deviation of a system from harmonic oscillation, and is when the restoring force no longer is proportional to the displacement. By adding anharmonic perturbations to the harmonic oscillation approximation, one improves the approximation, especially at greater displacements from equilibrium, see Figure 2.2.4. By applying the Scrödinger equation to Equation 2.11, one can then calculate the vibrational energy levels of this model, which is given by:

$$E_v = (v + \frac{1}{2})v_e - (v + \frac{1}{2})^2 v_e x_e + (v + \frac{1}{2})^3 v_e y_e + \text{higher terms} \tag{2.12}$$

where v is the vibrational quantum number, and x_e and y_e are the first and second anharmonicity constants. This potential is less confining than a parabola used in the harmonic oscillator. A consequence of this is that the energy levels become less widely spaced at high excitation. [20, 21, 22, 23, 24]

As explained above, adjacent vibrational energy levels have a difference in energy. These are typically smaller than a molecules electronic states, and the vibrational energy modes can be considered as a sub-structure of the electronic states. A Jablonski diagram is a diagram that illustrates the electronic states and the vibrational levels of a molecule, as well as the transitions between them, and an example of this can be seen in Figure 2.2.5 [25]. The difference in energy between two vibrational states is equal to hv, where v is the difference in frequency of vibration for the two vibrational energy levels. [18, 19]

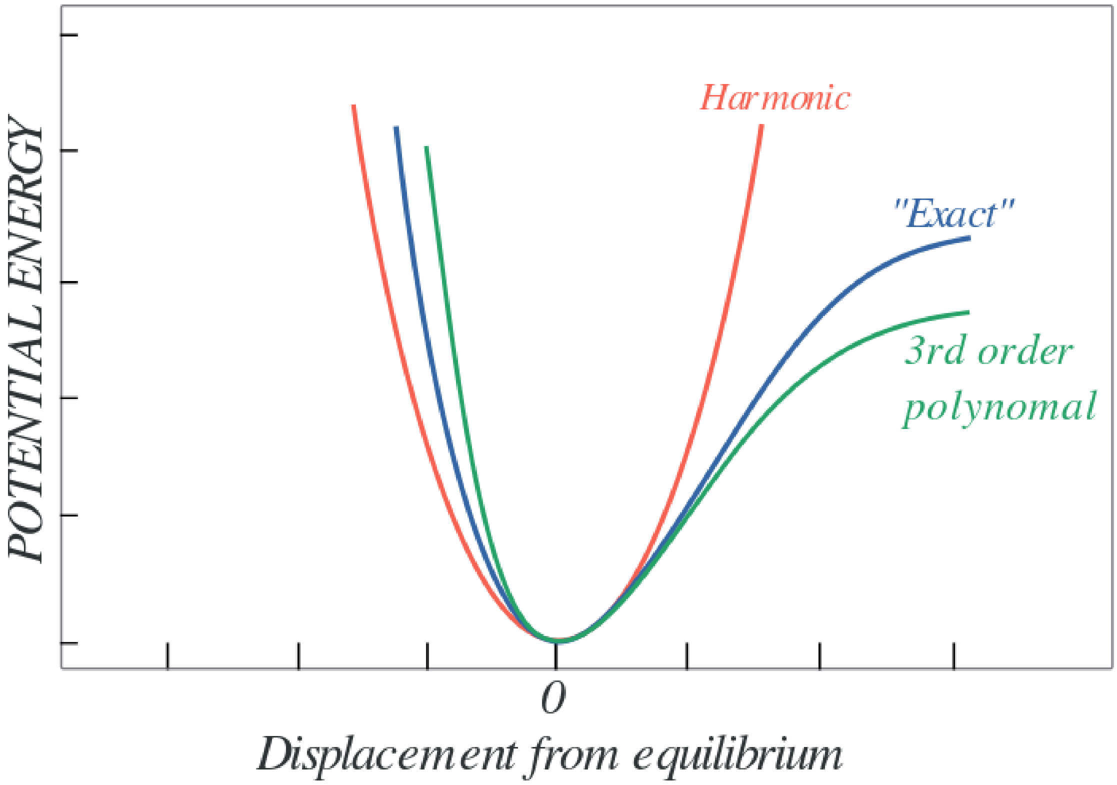

Figure 2.2.4: Simple harmonic potential approximation (red curve) of true/exact potential (blue curve) with anharmonic perturbations (green). (CC BY-NC; Ümit Kaya via LibreTexts)

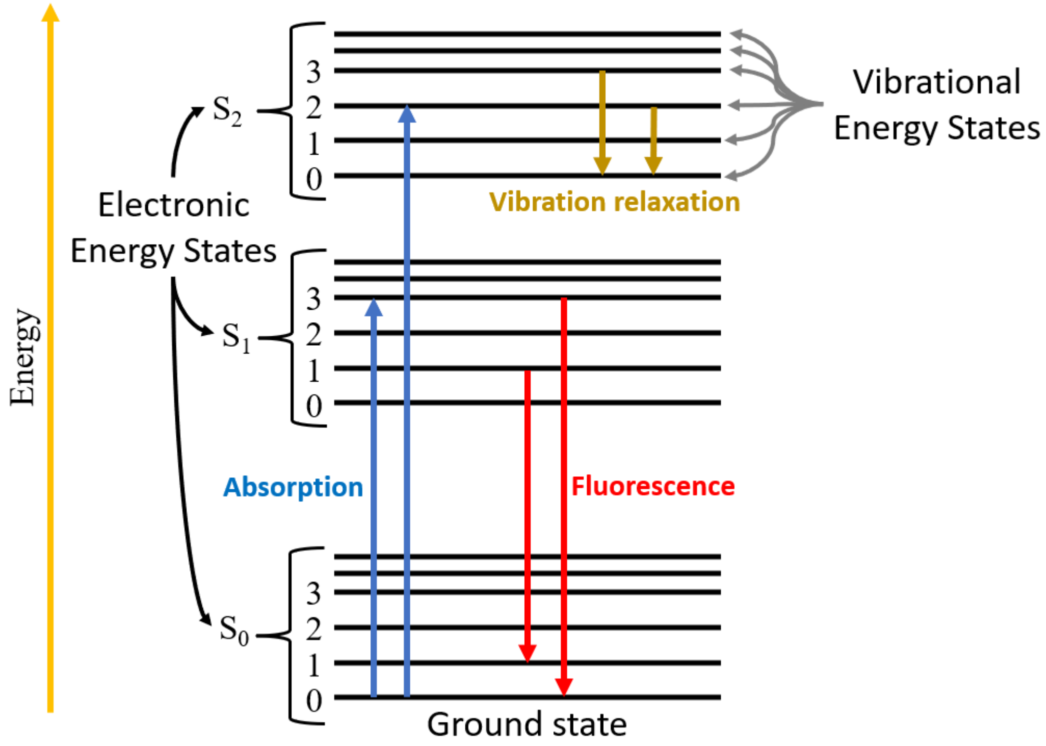

Figure 2.2.5: A Jablonski diagram. Three electronic levels are depicted along with four vibrational energy levels.

E_0 and E_1 is used to represent electronic energy levels, while υ is used to represent the vibrational modes in a molecule. If a sample is illuminated with photons with energy lower than the energy difference between the two energy levels, $\triangle E = E_1 - E_0$, one would expect that non of the photons would be absorbed by by the sample. This is however not 100 % correct, as sometimes, the oscillating electromagnetic field of the photon will induce a polarisation of the molecule's electron cloud (slight relative shift of positive and negative charge within the electron cloud). This then leaves the molecule in a higher energy state, as the photon's energy has been transferred to the molecule. This state of the molecule is called a virtual state, which is not very stable, and the molecule will therefore almost immediately re-emit the photon as scattered light. Several types of scattering can here occur. The most common is Rayleight scattering, in which the molecule returns to its ground state upon emitting the photon. Therefore, the vibrational state and energy of the molecule is unchanged after its interaction with the photon. The photon then is scattered elastically, leaving with the same energy as it had before interacting with the molecule. In a much rarer event, Raman scattering occurs, which is an inelastic scattering process. Here, energy is transferred between the molecule and the scattered photon during the scattering process. If the molecule gains energy from the photon, it will drop down to a higher vibrational energy state (like $\upsilon = 1$) instead of to its ground state ($\upsilon = 0$), meaning the molecule has been excited to a higher vibrational state than it had originally. Here, one gets what is called Stokes scattering, where the scattered photon has lost energy and increased its wavelength. If the photon that induced the polarisation in the molecule had energy E_L, and the scattered photon had energy E_S, then the molecule has gained energy $\hbar\omega_{vib} = E_L - E_S$, where $\hbar\omega_{vib}$ is the energy of the vibration. If however the molecule loses energy by relaxing to a lower vibrational state than the one it started at (like from $\upsilon = 1$ to $\upsilon = 0$), one gets Anti-Stokes scattering. Here, the scattered photon gains energy and decreases its wavelength. The molecule has then lost energy $\hbar\omega_{vib} = E_S - E_L$. As Anti-Stokes scattering requires the molecule to be in an already excited vibrational state (like $\upsilon = 1$), and as the majority of molecules usually are found in their ground state ($\upsilon = 0$) at room temperature, it is normally less common than Stokes scattering, even if both quantum mechanically are equally likely processes. Figure 2.2.6 shows a scheme of the different types of scattering. [16, 17, 26, 27]

Raman spectroscopy use Raman scattering, primarily Stokes scattering, for the identification of molecules in a sample. First, a sample is illuminated by a laser. Then, the energy/frequency difference between the incident laser light and the scattered light, known as the Raman shift, is detected. This difference is only connected to the energetic properties of the sample studied and is therefore independent of the wavelength of the laser. A sample can give many different Raman shifts, which are usually expressed in wavenumbers (the spectroscopic definition). Wavenumber can be converted to wavelength using Equation 2.5, and to energy using equation

$$\bar{\upsilon} = h \times \frac{c}{E} \tag{2.13}$$

Another important value is the so called count rate, which is the number of times per second that the respective Raman shift is registered by the detector. This value is proportional to the intensity of the light released by the respective Raman shift onto the detectors. The higher the light intensity, the more Raman scattering has occurred in the specific wavenumber region. By plotting the Raman shift up against the count rate, one gets what is called a Raman spectrum, a spectrum highly specific to every molecule. It can therefore be used to determine which molecules are in a sample. [28]

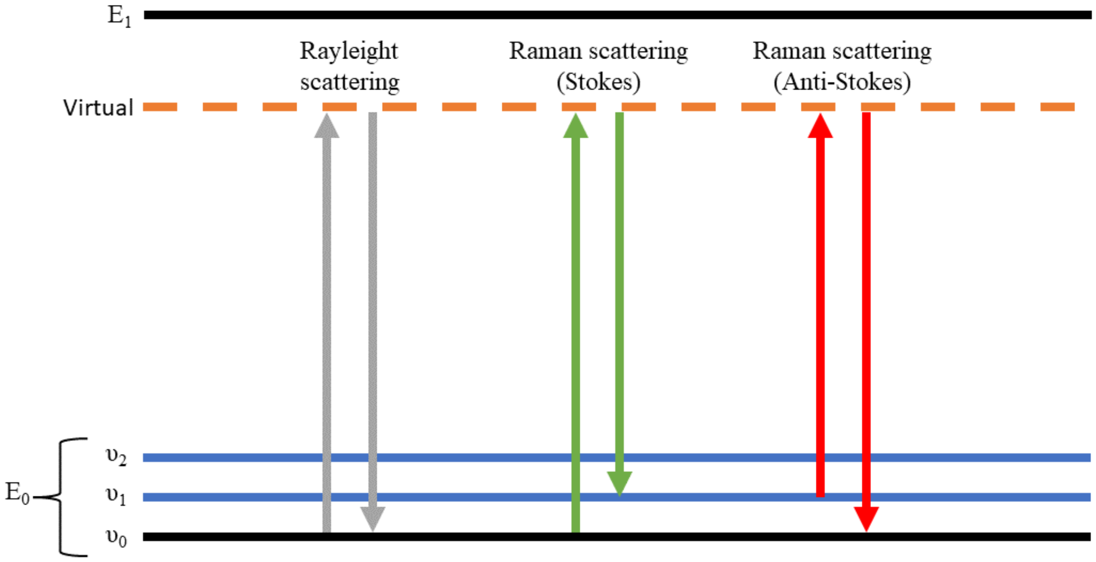

Figure 2.2.6: The three different types of scattering that can occur when a molecule is excited to a virtual state.

There are a number of ways to interpret a Raman spectrum. One of them is to use the Raman spectrum to identify functional groups within the molecule. Distinct subunits all have a characteristic Raman shift, which will appear on the spectrum. This can be used to monitoring reactions that involve different functional groups, as they then provide a direct measure of the progress during the reaction, or it can be used to relate the spectrum of an unknown compound to a class of substances. The carbonyl group in an aldehyde for example always has a Raman shift in the range of 1700-1730 cm^{-1}, so a Raman spectrum that contains this Raman shift might just be an aldehyde. Another way of interpret a Raman spectrum is to look after the so called "fingerprint region" of a molecule. The vibration of the molecular scaffolding (the molecules "skeleton") can be detected in the Raman spectrum, and this creates a substance-specific, characteristic pattern, usually below 1500 cm^{-1}. This region can then be used to identify different compounds. A third way to use Raman spectroscopy for substance identification is by using software the compares the Raman spectrum from the substance with all the Raman spectrums found within a spectral database. This makes it possible to interpret a Raman spectrum within seconds. [28]

There are many advantages of using Raman spectroscopy for characterisation of samples. The technique requires little to no sample preparation, and does not alter or damage the sample (as long as the intensity of the laser illumination isn't too high). It can be used to determine both organic and inorganic compounds, and can be done on aqueous solutions, as water produces very little Raman scattering. There are however some disadvantages. As fluorescent materials also release photons when illuminated by radiation, it becomes more difficult to separate the Raman signal from the fluorescent signal. Raman spectroscopy can also not be used to analyse alloys or metals, and require highly sensitive instrumentation. [29]

2.2.1 Micro-Raman

Micro-Raman spectroscopy is a technique where one acquires a spatially resolved Raman spectra, which shows the intensity of scattered light acquired after a samples is radiated by the incident light. This is done by combining a conventional Raman spectrometer with a microscopic tool, typically an optical microscope. This enables the micro-Raman spectrometer (µRS) the collection of spectral information with a submicron spatial resolution. This allows one to choose the exact area of interest for identification and analysis of physical and chemical properties of the material under investigation. A simplified schematic for a µRS can be seen in Figure 2.2.7. [30]

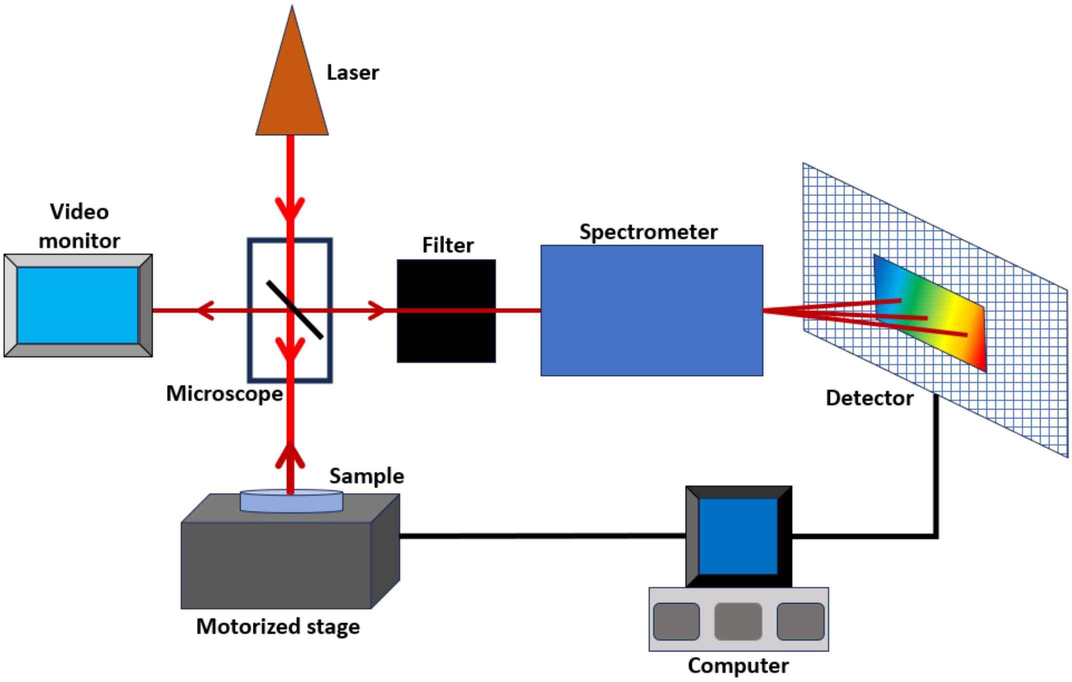

Figure 2.2.7: Simplified schematic of the setup of a micro-Raman spectrometer.

2.2.2 Raman specter for certain molecules

As already mentioned will each molecule have a highly specific Raman spectrum. For example, glass seems to give the strongest Raman signal at around 1100 cm^{-1} [31], while calcium phosphate gives the strongest signal somewhere between 960-990 cm^{-1} [32, 33, 34].

As larger molecules can have complex structures, they can also have more complex Raman spectra. Polymethyl methacrylate (PMMA) for example has many different peaks at varying sizes, among them those at 600, 810-850, 900-1000, 1130-1230, 1330-1390, 1450-1480, 1730 and 2700-3000 cm^{-1} [35, 36, 37, 38, 39]. A Raman spectrum for PMMA can be seen in Figure 2.2.8. It should be noted that the Raman shifts of PMMA seem to change a little based on the material the PMMA is supported by/layered on top of [39].

Certain normal modes of vibration actually have their Raman peaks known. For water, symmetric stretching has a Raman peak at 3685 cm^{-1}, asymmetric stretching has its peak at 3506 cm^{-1}, and bending has its peak at 1885 cm^{-1}. [18] For lipids, the stretch vibrations for the C=O of the fatty acidglycerol ester linkage is observed around 1740 cm^{-1}, while the stretch vibration for the CH in the methylene and terminal methyl groups of the fatty acid chains can be observed around the 2850-3025 cm^{-1} region. [40]

2.3 Confocal Raman Microscopy

Confocal Raman microscopy (CRM) is a microscopy technique that combines the spatial filtering of a confocal optical microscope with the spectral information from Raman spectroscopy for high-resolution chemical imaging of samples. The vibrational modes of the sample provides extensive chemical, physical and structural

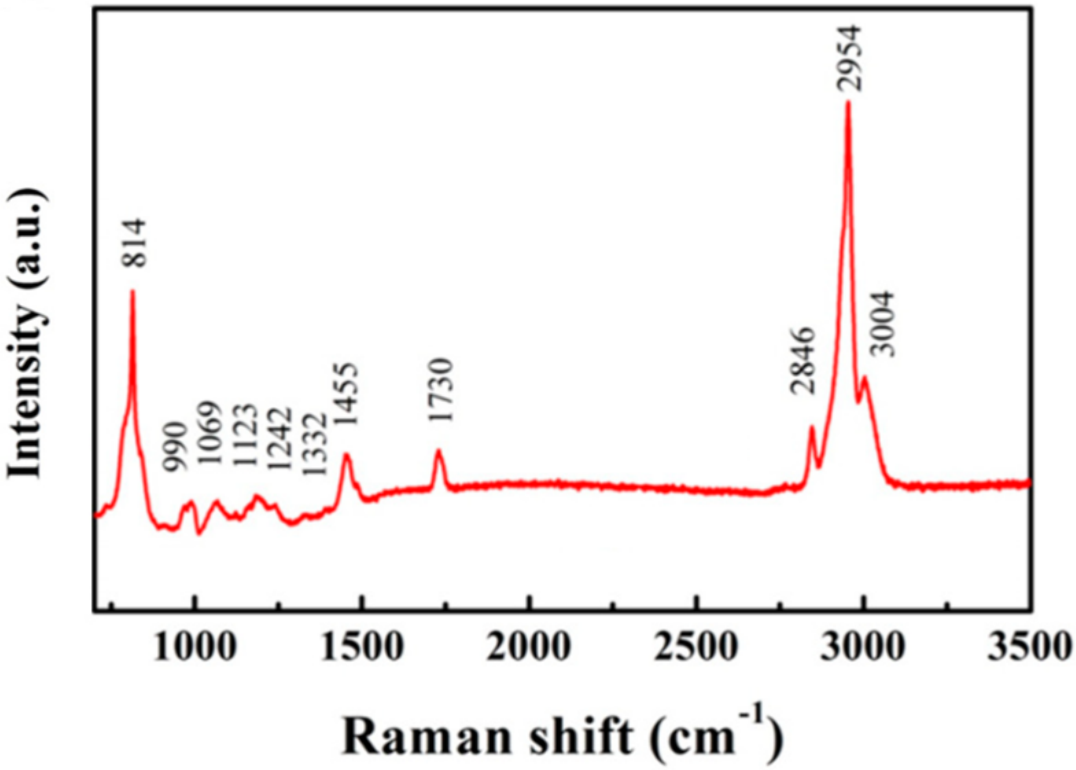

Figure 2.2.8: The Raman spectra of PMMA bulk film (760 nm) on quartz substrate. (CC BY 4.0; Polymer Vol. 11, Iss. 4 via mdpi.com [39])

information, while the confocal optics of the microscope works as a spatial filter for the laser, giving high resolution in lateral and axial directions. A spatial filter is a filter designed to remove random fluctuations from the intensity profile of a laser beam. These fluctuations are created when the laser is scattered by optical defects and particles in the air. [41, 42]

A schematic of an CRM can be seen in Figure 2.3.1. The microscope consists of many different components. The first is the laser, used to illuminate the sample and create Raman scattering. The Raman scattering intensity, spatial resolution and background fluorescence are all affected by the laser's wavelength. The next component is the objective lens. It has the function of both focusing the laser on the sample, and to collect the Raman scattering produced by the sample. The numerical aperture (NA) of the objective lens together with the laser wavelength determines the lateral spatial resolution. The theoretical lateral resolution that can be achieved is given by the Rayleigh criterion:

$$Lateral\ Spatial\ Resolution = \frac{0.61\lambda}{NA} \tag{2.14}$$

As previously mentioned, Rayleigh scattering is the most common type of scattering that occurs when a molecule is excited to a virtual state. This type of scattering gives no information and is therefore just noise that needs to be discarded before detection. This is the function of the rejection filter. It can be one of two types of filter: a long pass optical filter or a notch filter. A long-pass optical filter absorb all wavelengths beneath a certain value, and transmit all wavelengths

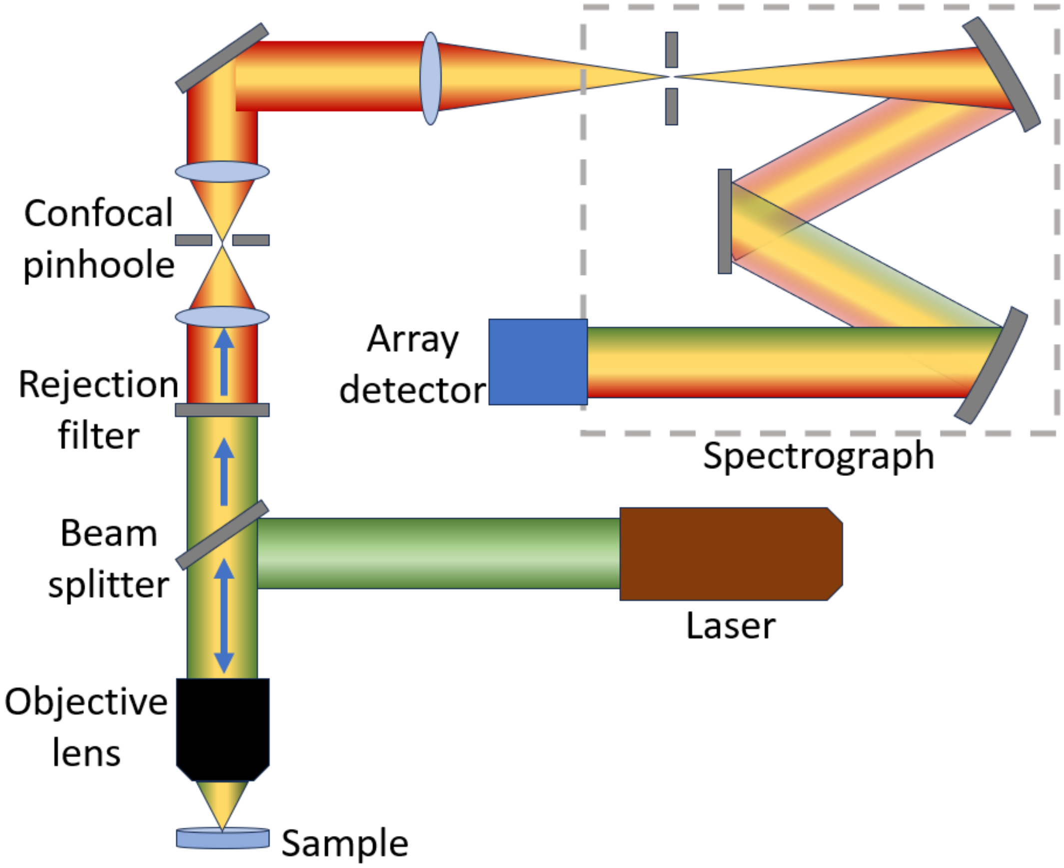

Figure 2.3.1: Optical Layout of a confocal Raman microscope.

above this value. A notch filter on the other hand have a sharp absorption peak at one particular wavelength, which is chosen to coincide with the laser wavelength, with all other wavelengths being transmitted. [41]

The spectrograph spatially separate the different wavelengths of the Raman scattering using a combination of mirrors and one or more diffraction gratings, and image them onto a detector. The spectral resolution of the Raman microscope, or its ability to separate closely spaced Raman peaks, is determined by the focal length of the spectrograph, the width of the entrance slit, and the groove density of the different diffraction gratings.[41] The detector of the CRM is an array detector, which is a detector that can make multiple measurements simultaneously [43].

The defining feature of a confocal microscope, the confocal pinhole, is used to improve the spatial resolution, increase the contrast, and decrease the fluorescence background of the Raman mapping. How it works is that it blocks out all out of focus Raman scattering, that is to say all Raman scatter from above or below the focal plane, from entering the spectrograph and being detected, as shown in Figure 2.3.2. Without the pinhole, there is no axial spatial filtering, and the Raman scattering collected from the sample would therefore have no axial resolution. The pinhole also blocks scatter created from outside the lasers focal point (the area radiated by the laser) and background fluorescence, which enhances the contrast. [41]

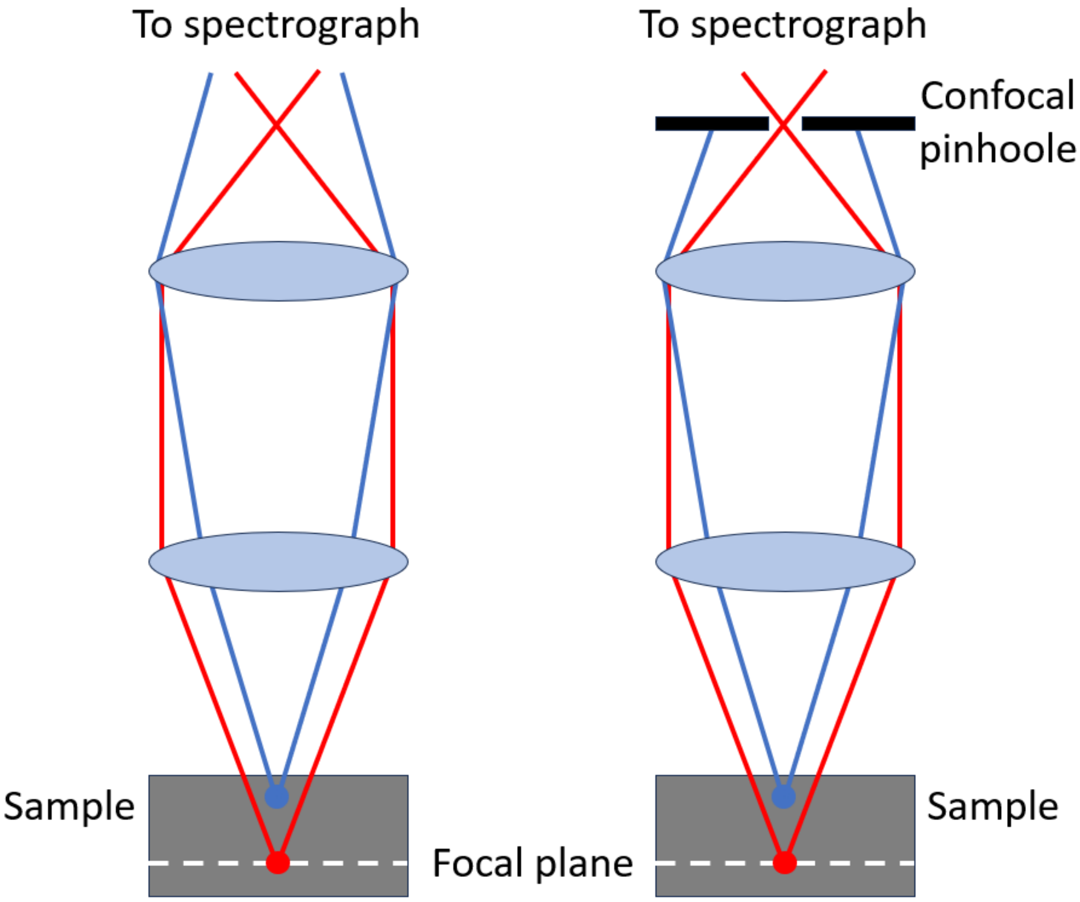

Figure 2.3.2: How the confocal pinhole blocks out of focus Raman scatter.

2.4 Stimulated Raman Scattering Spectroscopy

The major disadvantage with spontaneous Raman scattering described above is a low signal level, which is due to the low spontaneous Raman scattering efficiency per molecule. In order to overcome this weakness, coherent Raman scattering microscopy techniques, based on either stimulated Raman scattering (SRS) or coherent anti-Stokes Raman scattering (CARS) has been developed. [44, 45]

SRS involves two incident lasers: a pump laser at frequency ω_p and a Stokes laser at frequency ω_S. When the difference in frequency between the two lasers, $\triangle\omega = \omega_p - \omega_s$, matches the particular vibrational frequency of a Raman-active vibrational band, an amplification of the Raman signal is achieved by virtue of stimulated emission. This leads to the Stokes beam experiencing a gain in intensity (ΔI_S), while the pump beam experience a loss of intensity ($\triangle I_p$), as shown in Figure 2.4.1. It is this gain/loss across the spectral region of interest that is measured with SRS. SRS does not exhibit a non-resonant background (described in section 2.5), as neither stimulated Raman gain or loss can occur if $\triangle\omega$ does not match any vibrational resonance. [46, 47]

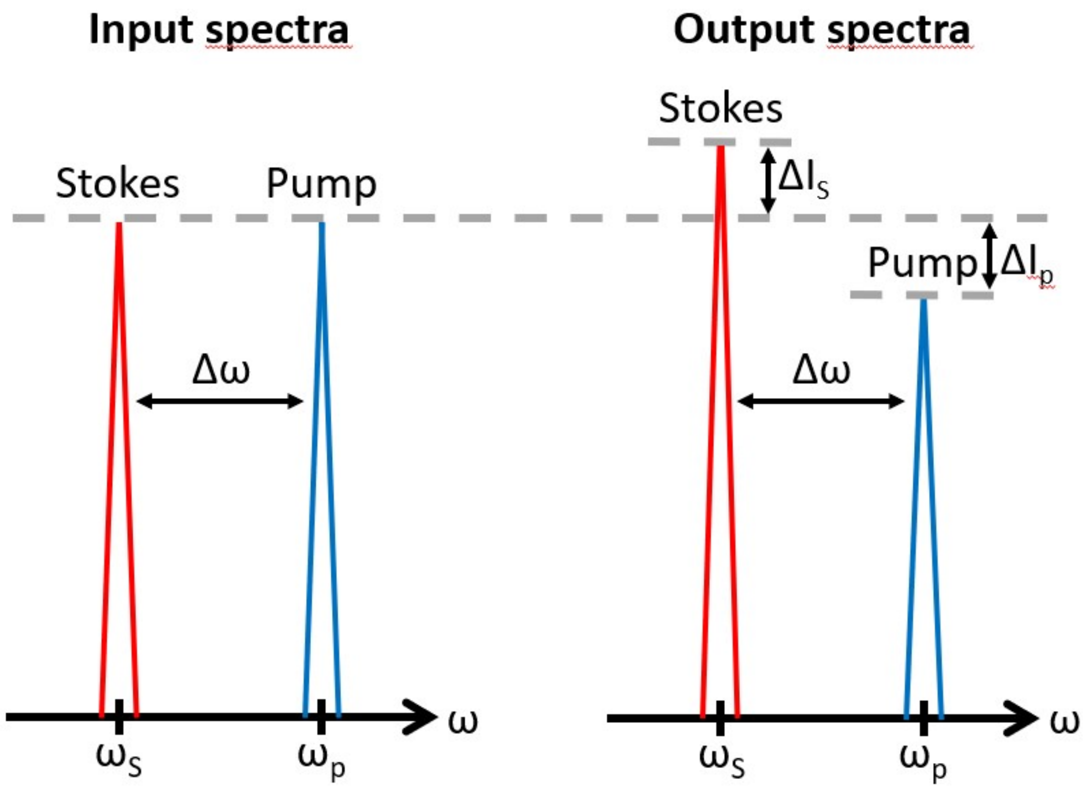

Figure 2.4.1: Input and output spectra of SRS. SRS leads to an intensity increase in the Stokes beam, and an intensity decrease in the pump beam.

2.5 Coherent Anti-Stokes Raman Scattering Spectroscopy

Less technical demanding than SRS, CARS spectroscopy also involves two incident lasers, a pump and a Stokes laser, at different frequencies. Unlike SRS however, the goal of CARS is to study the anti-Stokes scattering created from the interactions between electromagnetic radiation and molecules. However, as already mentioned, anti-stokes scattering has much lower intensity than Stokes scattering under normal conditions, as most molecules finds themselves in their ground state at room temperature ($\upsilon = 0$). Because of this, the molecules first have to be excited up to a higher vibrational energy state before anti-Stokes scattering can be produced. How this process works is that light first is emitted from the pump laser onto the molecules, in order to excite them up to a virtual state. Then, the molecules are radiated by the Stokes laser, which stimulate them into releasing photons with the same frequency as the Stokes beam. This will in turn increase the number of molecules that finds themselves in the higher vibrational state that was desired (e.g. $\upsilon = 1$). For this to work, the Stokes beam needs to have a lower frequency than the pump beam (see Equation 2.3 for the relationship between energy and wavelength). The frequency difference between the two beams that ensure that the molecule ends up in a higher vibrational state is found according to equation

$$v_{vib} = \frac{1}{\lambda_{pump}} - \frac{1}{\lambda_{stokes}} \tag{2.15}$$

where v_{vib} is the Raman shift, which here will have the value of a sizeable Raman shift created by the molecule (usually found by looking at the molecule's Raman spectrum). Furthermore, the molecules are then radiated by a probe beam, which excite them up to a new vibrational state with higher energy than the first. From here, the molecules will then naturally relax down to their ground state by emitting photons. These photons will have a higher frequency/lower energy than all lasers used during the CARS process (this is the reason the second virtual state needs to have higher energy than the first). The pump and probe light are usually provided by the same laser, such that

$$\omega_{CARS} = 2\omega_{pump} - \omega_{stokes} \tag{2.16}$$

where ω_{CARS} is the frequency of the photons making up the CARS-signal, λ_{pump} is the wavelength of pump laser, and λ_{stokes} is the wavelength of the Stokes laser. Using this, one can get the equation

$$\lambda_{CARS} = \frac{1}{\frac{2}{\lambda_{pump}} - \frac{1}{\lambda_{stokes}}} \tag{2.17}$$

which tells the relationship between the wavelength of the anti-Stokes scattering released (λ_{CARS}), and the wavelength of the pump and Stokes lasers. See Figure 2.5.1 for a step by step guide of this process. [46, 48, 49]

By detecting the anti-Stokes radiation emitting from the molecules, CARS can be used for chemical characterisation of samples, as the radiation released is highly specific to a specific molecule, as well as for imaging of samples (such as cells), by processing the intensity of radiation captured from different areas of the sample. The imaging can be done on a scale less than 1 µm. CARS spectroscopy have all the advantages of Raman spectroscopy. As the signal strength is much higher in CARS than in Raman spectroscopy, the time between scanning the sample and receiving chemical information and/or an image is much faster, almost instantaneous. [48, 49, 50]

The CARS process is described as vibrationally resonant. Unfortunately, other interactions, which are described as non-resonant, can occur, which gives rise to what is called a non-resonant background signal. This signal is made when, at the step where the molecule normally would go from a virtual state to a vibrational state higher than the ground state (see Figure 2.5.1b), it instead ends up at another virtual state, either through excitation or emission. See Figure 2.5.2 for a schematic of this process. If the CARS signal is weak, this non-resonant background may overwhelm the resonant CARS signal, especially if the molecule almost was excited up to another electronic energy level during the process, also called being near two-photon resonance (see Figure 2.5.2a). A solution to this problem does however exist. Because the non-resonant process ends up at a virtual state after the second step, it is much shorter lived than the second stage of the CARS process (picoseconds in difference). By increasing the time between when the laser pulse from the probe laser hits the sample after the Stokes laser, also called increasing the delay, one can therefore inhibit the creation of non-resonant background signal. [51]

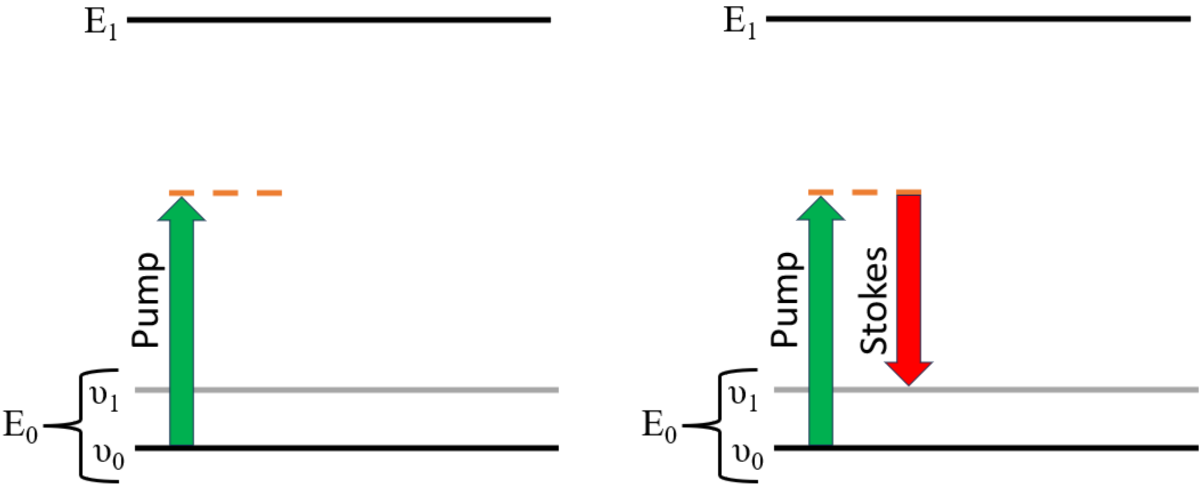

(a) Step 1 **(b)** Step 2

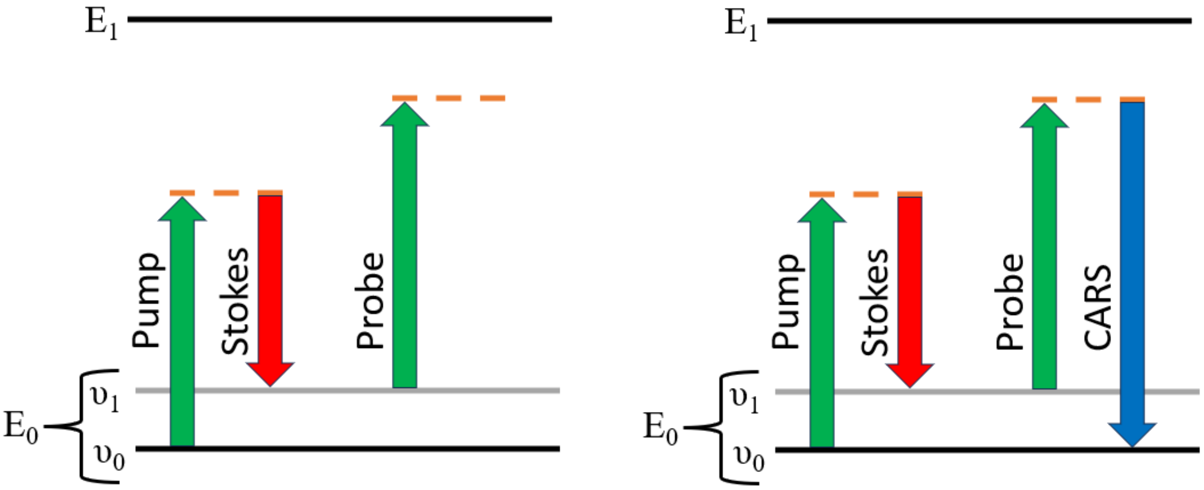

(c) Step 3 **(d)** Step 4

Figure 2.5.1: The four steps of the CARS process. **Step 1:** Light from the pump laser radiates the sample, creating many virtual states. **Step 2:** Light from the Stokes laser radiates the sample, stimulating the molecules to release photons with the same energy as the Stokes laser. The molecules now find themselves in a vibrational state higher than the ground state. **Step 3:** A probe laser is used to excite the molecules up to a new virtual state. The probe and pump beams are usually the same. **Step 4:** The molecules naturally relax from this virtual state to the ground state, releasing a photon with higher energy/shorter wavelength than the pump beam.

CARS signal is generated in two different directions, either forward (Trans signal) or backwards (Epi signal). Generally, the trans signal will be so strong that one clearly can differentiate it from the often strong non-resonant background that arises from the surrounding solvent. This signal is applicable to thin samples, and is detected with transmitted light detectors. If on the other hand the trans signal is overshadowed by the non-resonant background, the contrast can be enhanced by instead detecting the epi signal, which reduces the noise of the image. A sample

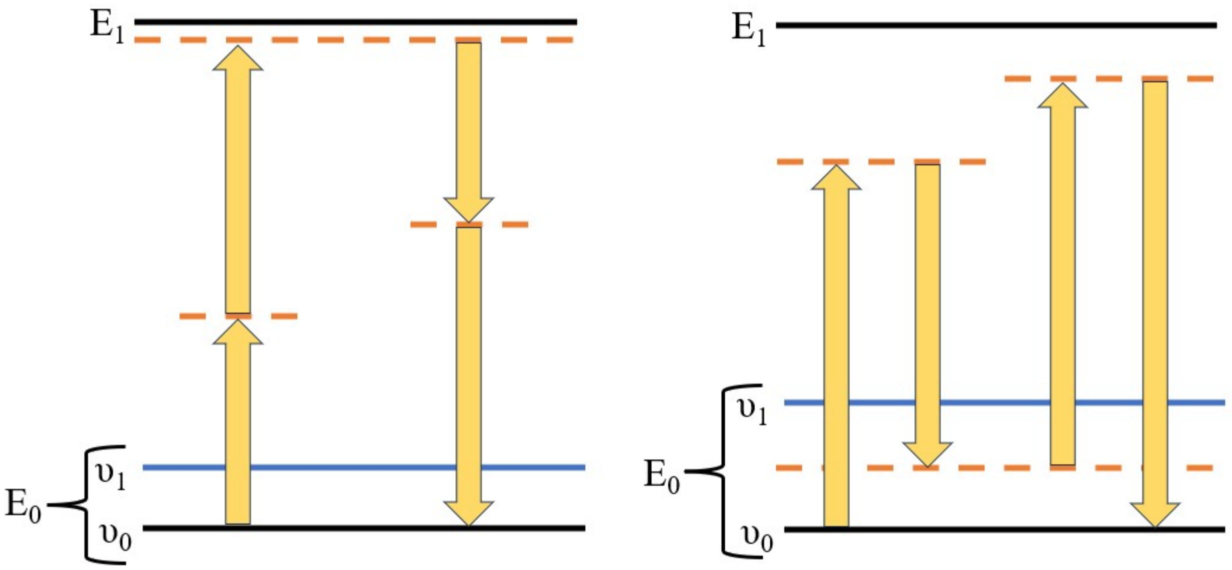

(a) Non-resonance near two photon resonance

(b) Non-resonance far from two-photon resonance

Figure 2.5.2: The two types of non-resonant background signal.

that is highly scattered can lead to a strong epi signal, as the forward propagating CARS signal here can be backscattered. [48]

2.6 Alizarin Red S

Discovered in 1871, Alizarin Red S (ARS) ($C_{14}H_7O_7SNa$) is a water-soluble version of the naturally occurring reddish dye alizarin. [52] In histology, ARS staining is typically used for assessing of calcium salts, like for example the calcium phosphate found in Hydroxyapatite (HAp) made by osteoblastic cell cultures. How it works is that calcium cations interact with the sulfonic acid group on ARS, forming a salt (sometimes called a complex or lake pigment). One calcium cation can react with two sulfonic acid groups at the same time, meaning it can bind to two ARS molecules at the same time. The ARS-calcium salt will have a red colour (just like ARS alone), resulting in a stain that can be observed visually. [53, 54]

The absorption spectrum for ARS shows that the chemical compound has its absorbance peak at 271 nm. The molecule also has the ability to absorb other wavelengths as well, though what these exact wavelengths are seem to depend on the pH of the environment it finds itself in. From approximately pH 1-4 ARS is able to absorb wavelengths at around 410-430 nm, while at pH-values of 5 and above, it instead absorbs wavelengths at around 530-550 nm. [55, 56, 57]

An schematic of the molecular structure of ARS can be seen in Figure 2.6.1.

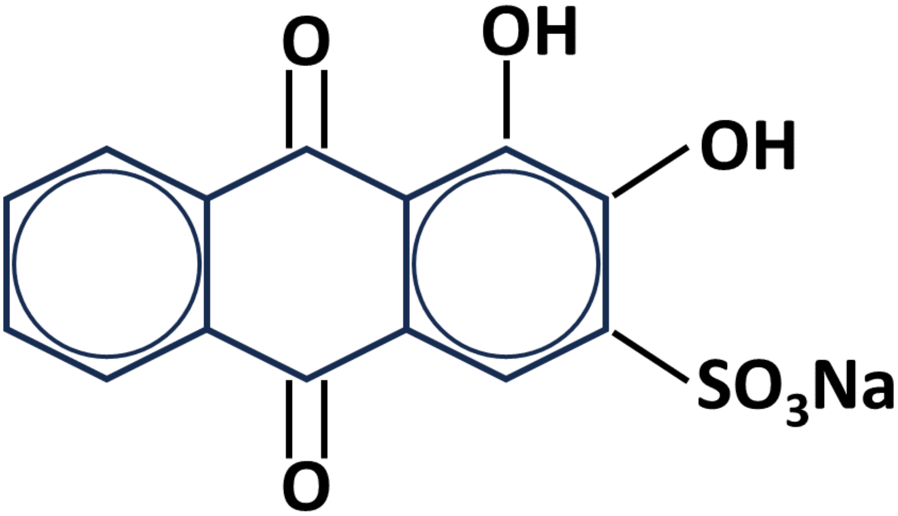

Figure 2.6.1: The molecular structure of Alizarin Red S.

2.7 Bone Matrix

Bone is composed of cells lying in an extracellular, calcified matrix. This calcified matrix, know as the bone matrix, consists of both inorganic and organic constituents. The inorganic portion of bone mainly consists of calcium phosphate minerals, while the organic portion consists of collagen fibers, proteoglycans, and glycoproteins. Multiple cell types are also present. [9]

2.7.1 Organic Component

Constituting approximately 30% of the weight of bone, the organic component (know as osteoid) primarily consists of collagen fibers (80-90%), which are almost exclusively type I collagen. The collagen is formed in large bundles (50 to 70 nm in diameter), with type I collagen being highly cross-linked. The most important functions of collagen in the bone is to provide a surface/scaffold for inorganic crystals to adhere, as well as to give the bones flexibility, so that they can bend without being brittle. [9, 58, 59, 60]

Most of the non-collagenous organic materials in the bone matrix are proteins produced by the bone cells. One group of these proteins are glycosaminoglycans (GAGs), large negatively-charged polysaccharide compounds that links together to form even larger molecules called proteoglycans [61]. These proteoglycans create an amorphous gelatinous material, which is known as the ground substance. They are among other things very good at absorbing water (water makes up around 10% of the weight of bone), making the ECM very good at resisting force. They may also help regulate collagen fibril diameters, as well as play a role in the mineralisation process. [9, 62, 59]

Several glycoproteins are also present in the bone matrix, which all appear to bind to certain parts of the bone. These include osteocalcin, osteopontin and bone sialoprotein. Osteocalcin binds to HAp, and is involved in binding calcium during the mineralisation process. Osteopontin binds to HAp as well as to integrins present on osteoblasts and osteoclasts, and plays a role in bone metabolism, biomineralisation, cell-mediated immunity and bone remodelling, as well as being involved in biological activities such as proliferation, migration, and adhesion of several bone-related cells [63, 64]. Bone sialoprotein has binding sites for matrix components and integrins of osteoblasts and osteocysts, which suggests that they somehow is involved in the adherence of these cells to the bone matrix. [9, 59, 60]

2.7.2 Inorganic Component

The inorganic portion of bone accounts for about 60% of its weight, and roughly 40% of its volume. It is primarily composed of calcium and phosphate in the form of HAp crystals [$Ca_{10}(PO_4)_6(OH)_2$], though calcium phosphate in an amorphous form also is present. It is these crystals that give bones their hardness and strength. The crystals, which are 40 nm in length by 20 nm in width, with a thickness of 1.5-3 nm, are arranged along the type I collagen fibers in an ordered fashion, being deposited in the gap regions and alongside the overlap regions of the fibers. Amorphous ground substance surrounds the free surface of the crystals. Exchange of ions with the extracellular fluid is made possible by a hydration shell around the crystals, which is formed by H_2O molecules attracted by ions on the surface of the crystals. [9, 58, 59, 60]

HAp crystallises in a hexagonal lattice with the space group of $P6_3/m$. The approximate cell parameters for this lattice has $a = b = 9.418$ Å, $c = 6.884$ Å, $\alpha = \beta = 90°$ and $\gamma = 120°$. [65, 66]

While HAp crystals makes up the majority of the inorganic portion of bone, there are actually many other components also present, in the form of impurities/-substitutions in the HAp crystals. These include carbonate, citrate, magnesium, potassium and sodium. Carbonate might be the most common, its weight proportion in bone mineral typically amounting to about 4-8% (depends on age). It can occupy either the PO_4^{3-} (B-type substitution, most common) and/or OH^- (A-type substitution) lattice sites of a HAp crystal. These types of impurities/substitutions seem to decrease the crystallinity of the bone mineral, which affects other mineral properties such as solubility [67]. A fraction of the PO_4^{3-} lattice sites may also be occupied by HPO_4^{2-}. Lastly, ion vacancies in the crystal lattice are also present. [68, 9, 69]

2.8 Bone Cells

A small amount of the bone volume consists of cells, which are crucial to the function of bones. An illustration of the different cell-types can be seen in Figure 2.8.1. [58]

2.8.1 Osteoprogenitor cells

Osteoprogenitor cells, also known as osteogenic cells, are undifferentiated cells derived from embryonic mesenchymal cells. They have high mitotic activity, and are the only bone cells that are capable of mitosis. They can be found (in their immature form) in the deep layers of the periosteum and in the bone marrow. They have the potential to differentiate into osteoblast, though they can also

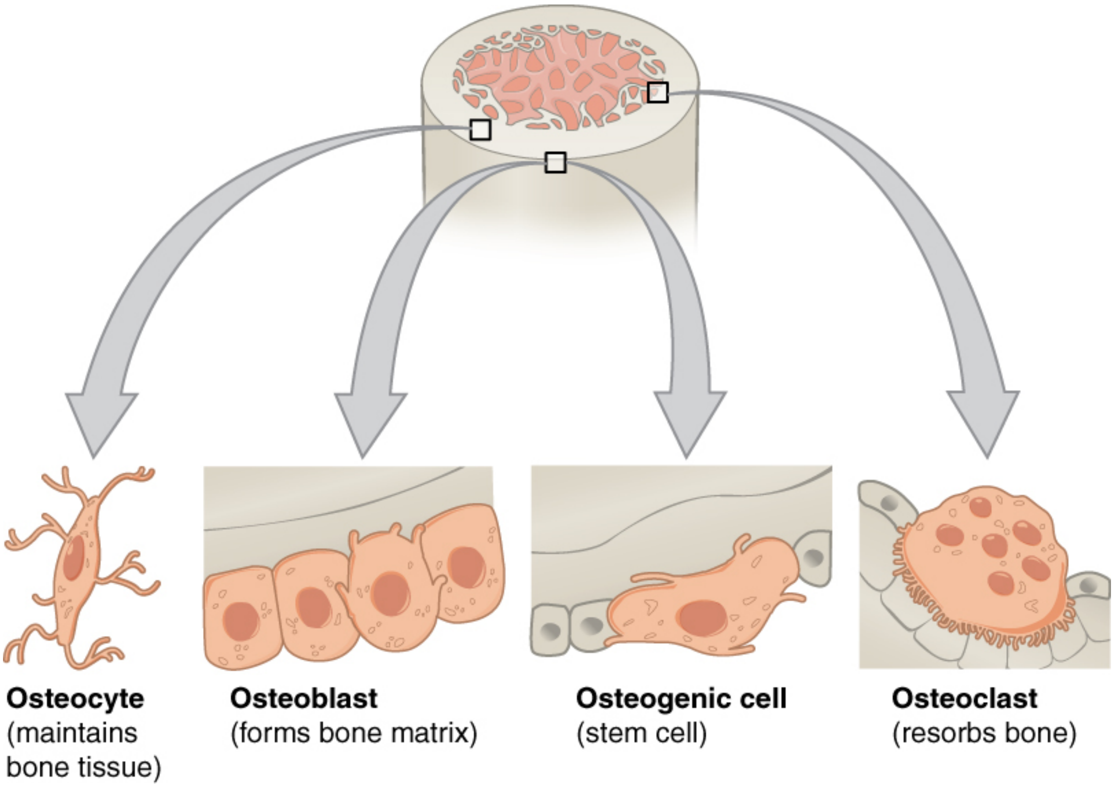

Figure 2.8.1: Four types of cells found and within bone tissue, and their function within the tissue. (CC BY 4.0; Anatomy and Physiology 2e via OpenStax[58])

differentiate into chondrogenic cells (important in the formation of cartilage) under conditions of low oxygen tension. [9, 58]

2.8.2 Osteoblasts

The osteoblasts are the cells responsible for the formation of new bone, and can be found on the growing portion of its surface. Osteoblasts manufacture and release the organic components that constitute the extracellular matrix of bone, which include type I collagen, glycoproteins, proteoglycans and cell attachment proteins. [9, 58, 59]

Osteoblasts also promote the mineralisation of the osteoid through both indirect and direct mechanisms. The indirect mechanism involves the synthesis and secretion of charged noncollagenous proteins associated with the collagen gap regions, where they direct mineral precursors into the collagen fibril. The direct mechanism happens through extracellular matrix vesicles budding of from the outer cell membrane of the osteoblasts. Through attraction and uptake, these vesicles will collect Ca^{2+} and PO_4^{3-} into themselves, where HAp crystals are formed. These crystals will later be released into the extravesicular fluid. [70, 71]

2.8.3 Bone Lining Cells

Ostoblasts that cover the surface of bone, and that cease to form matrix, revert to a more quiescent flattened-shaped state, and are called bone lining cells. By preventing the direct interaction between osteoclasts and bone matrix, they hinder bone resorption in the areas they cover. They can also be reactivated into secreting osteoblasts with the proper stimulus. [9, 59, 72]

2.8.4 Osteocytes

Lying within the bone itself are the osteocytes, mature bone cells differentiated from osteoblasts which became "trapped" when the bone matrix calcified around them. Per mm^3 there can be as many as 20 000 to 30 000 osteocytes. Each osteocyte is located in a cavity within the bone called a lacunae, which have many fine canals called canaliculi radiate out from it in all directions. Cytoplasmic processes of the osteocyte are hosed within these canaliculi, letting the osteoblasts communicate with each other. They also contain extracellular fluids, through which nutrients and metabolites are delivered to the osteocytes. [9, 58, 59]

Osteocytes seems to have two main functions within the bone. The first is to maintain the mineral concentration of the matrix via the secretion of enzymes. The second is to function as the main mechanoreceptors of bone, that is to say the main way the bone detects and respond to mechanical stress. They respond by releasing factors such as insulin-like growth factors, cyclic adenosine monophosphate and osteocalcin, which facilitates the recruitment of osteoprogenitor cells to assist in the remodelling of the skeleton. [9, 58, 59]

2.8.5 Osteoclasts

Originating from the macrophage-monocyte cell lineage, osteoclasts are multinucleated cells responsible for the resorption of bone. They are created when monocytes and/or macrophages migrate from the bone marrow into a specific skeletal site, where they fuse either with each other in order to form new osteoclasts, or with already existing osteoclasts. The cells are found on the surface of the bone, occupying shallow depressions formed by bone resorption called Howship's lacunae. [9]

The formation and function of osteoclasts are dependent on local signals from other cells, like osteoblasts, and growth factors in the bone matrix. Bone resorption can first happen after osteoblasts not only has activated osteoclasts, but also have absorbed the osteoid that separates them from the HAp surface, and then migrated away from that surface. The newly freed bone surface can then be occupied by the activated osteoclasts. The cells will then secrete several organic acids, thus reducing the pH of the microenviroment. This then leads to the dissolvement of the inorganic component, with the released minerals being taken up by the osteoclasts, and delivered to nearby capillaries. The osteoclasts also secrete lysosomal proteolytic enzymes and cysteine proteinases in order to degrade the organic component of the now decalcified bone matrix. The degrade organic component will then be further broken down into amino acids, monosaccharides and disaccharides by the osteoclasts through endocytose, and then released into the nearby capillaries. [9, 58, 59]

The balance between osteoblasts and osteoclasts is responsible for the constant reshaping of bone, as osteoclasts continuously break down old bone while osteoblasts continuously form new bone. [58]

2.9 Compact and Spongy Bone

Bone can be divided into two different types of structures: compact bone, a very dense bone with the function of withstanding compressive forces; and spongy bone (also called cancellous bone), which is filled with open spaces, with the function of supporting shifts in weight distribution. Most bones contains both compact and spongy tissue, but their distribution and concentration vary based on the bone's overall function. [9, 58]

2.9.1 Compact Bone

Compact bone is composed of thin layers of calcified matrix, called lamellae, arranged in layers. The bulk of compact bone is composed of a microscopic structural unit called an osteon, or Haversian canal system. Each osteon is composed of concentric rings of lamellae, aranged around a vascular space known as the Haversian canal. Running through these canals are blood vessels, nerves, and lymphatic vessels. Haversian canals are connected to each other by Volkmann canals, vascular spaces that are oriented perpendicular to or oblique to Haversian canals. The outer layer of dense bone is called the outer circumferential layer, and is connected to the periosteum (two layer membrane consisting of a dense fibrous connective tissue layer and a cellular layer containing osteprogenitor cells). An inner circumferential lamellae also exists, completely encircling the marrow cavity. Within a lamellae, collagen fiber bundles are parallel to each other, though they are oriented almost perpendicular to those of adjacent lamellae. The lacunae containing the osteocytes are found at the borders of adjacent lamellae. [9, 58] Figure 2.9.1 shows a cross-sectional view of compact bone, along with its structures.

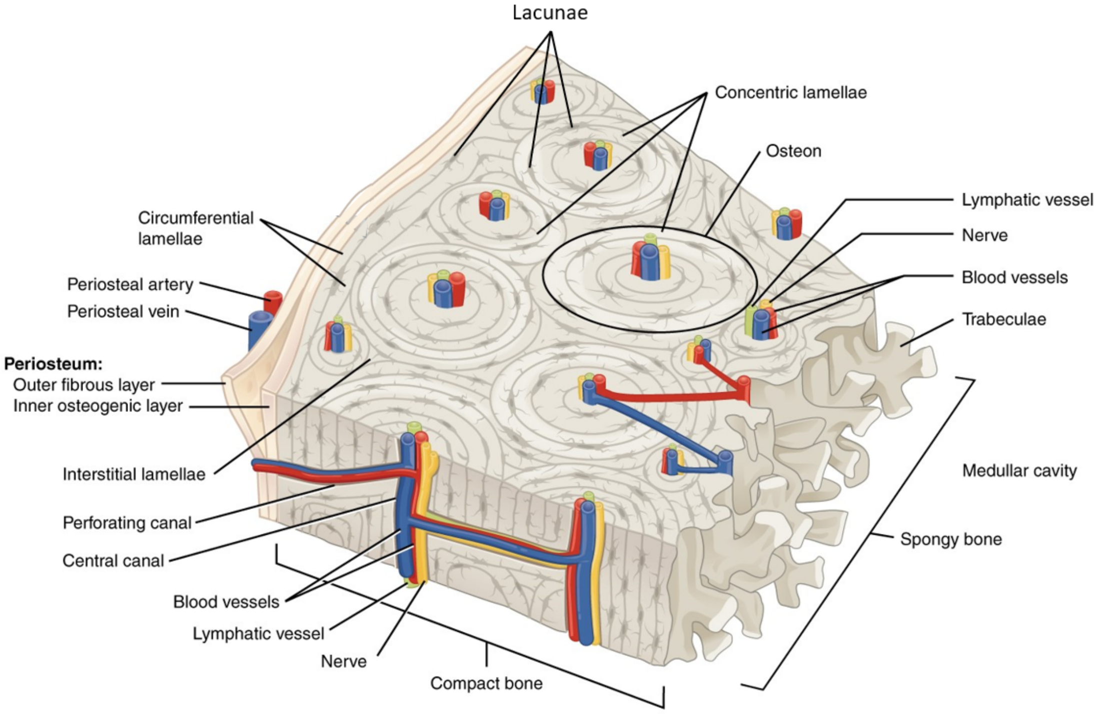

Figure 2.9.1: A cross-sectional view of compact bone and its structures. (CC BY 4.0; Anatomy and Physiology 2e via OpenStax[58])

2.9.2 Spongy Bone

Unlike the compact bone, spongy bone contains no Haversian system. Instead, the lamellae of spongy bone are arranged in a lattice-like network of matrix spikes called trabeculae. They are lined with a thin specialised connective tissue composed of a monolayer of osteoprogenitor cells and osteoblasts, called endosteum. While it might seem like the trabeculae are arranged in an irregular fashion, in reality each trabecula forms along lines of stress in order to provide strength to the bone. The lamellae of spongy bone also contains lacunae housing osteocytes, which gains nourishment through diffusion from the marrow cavity surrounding the trabeculae. These cavities are filled with red bone marrow, which contains blood stem cells (can differentiate into red blood cells, white blood cells, or platelets), and where the formation of blood cells (hematopoiesis) occurs. [9, 58] There also exists yellow bone marrow in the bone (though located in the medullary cavity rather than in the spongy bone), which is composed mostly of fat. It also contains stem cells that can become cartilage, fat, or bone cells. [9, 73] See Figure 2.9.2 for a schematic of spongy bone.

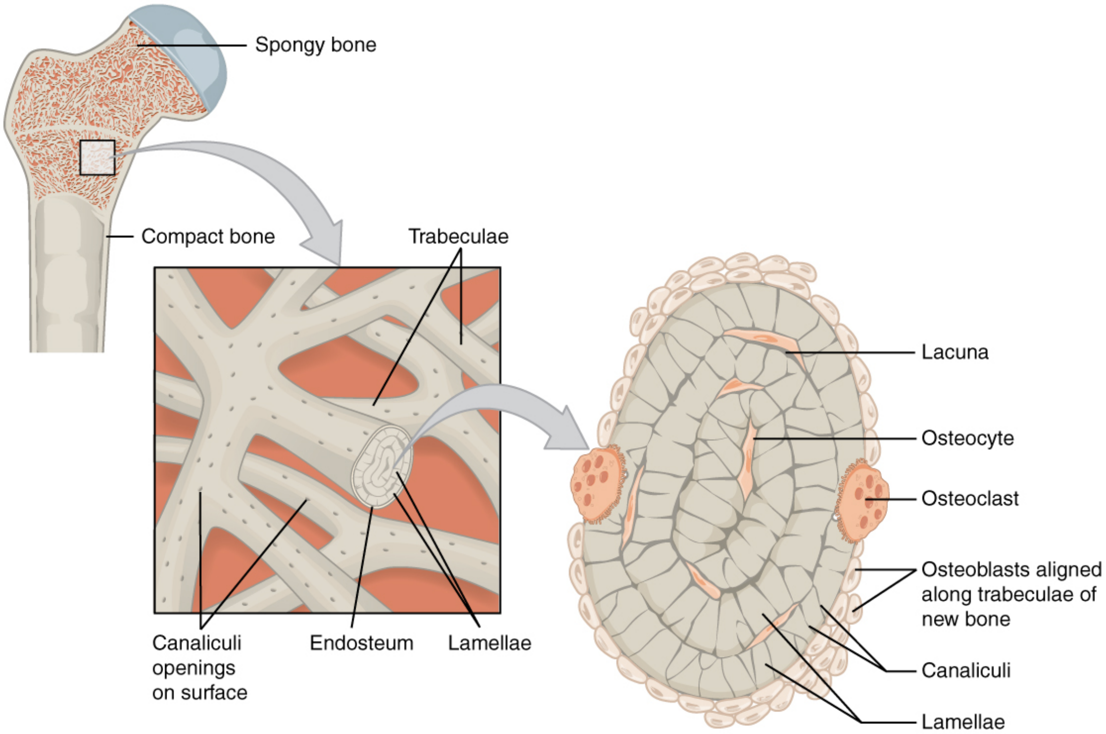

Figure 2.9.2: Spongy bone and its structures, the trabeculae. (CC BY 4.0; Anatomy and Physiology 2e via OpenStax[58])

2.10 Raman Signal for Bone

The phosphate group associated with the mineral component of bone has four vibrational modes. The ν_1 PO_4^{3-} stretching mode gives the strongest Raman signal (highest peak) for bone, and is therefore the strongest marker for the tissues mineral component. This peak can usually be found around 960-970 cm^{-1}, though certain tests has shown that it can sometimes also appear at upwards of

990 cm^{-1} [32, 33, 34]. The other vibrational modes for phosphate are the ν_2 and ν_4 bending modes at around 430-450 and 587-604 cm^{-1}, and the ν_3 asymmetric stretching mode at 1035-1048 and 1070-1075 cm^{-1}. [74, 75] Different parts of the organic component (collagen and non-collagen moieties) of bone also gives a Raman peak. These are amide III in the region 1200-1340 cm^{-1}, amide I in the region 1600-1700 cm^{-1}, CH bending at 1400-1470 cm^{-1}, and CH stretching at 2800-3100 cm^{-1}. Some important amino acids in collagen that might give of a Raman signal is proline at around 850 and 920 cm^{-1}, and hydroxyproline at around 870-880 cm^{-1}. [76, 77, 78] For the carbonate group (CO_3^{2-}), the internal modes are detected at 1073 cm^{-1} (ν_1 mode of B-type carbonate) and at 1103 cm^{-1} (mode of A-type carbonate). [74, 75, 79, 80] A typical Raman spectrum for bone tissue can be seen in Figure 2.10.1

One should of course also remember that the nerves, veins and blood vessels found in the bone tissue give their own Raman spectra when studied. Peaks relating to CH bending (1400-1470 cm^{-1}), amid I (1600-1700 cm^{-1}) and CH stretching (2800-3100 cm^{-1}) also appear in these spectra. Many other peaks also appear, including peaks related to cellular components such as phenylalanine (1000 cm^{-1}), CH_2 bending mode (1450 cm^{-1}). [81]

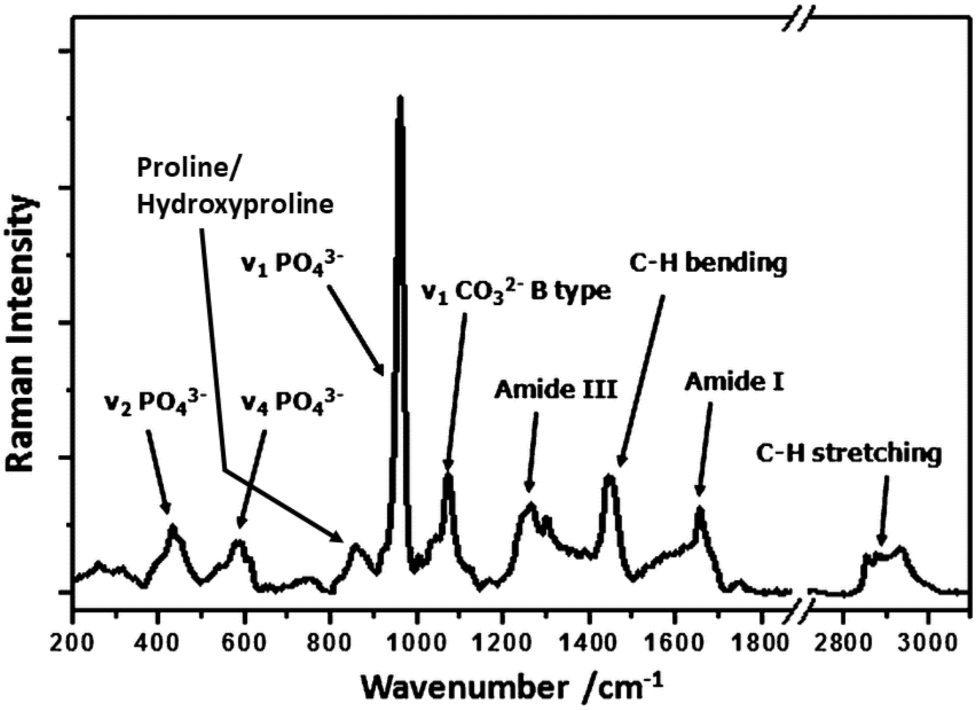

Figure 2.10.1: A typical Raman spectrum of bone tissue showing the major bands and the corresponding compounds. The background signal has been removed. The bands for A-type carbonate and ν_3 PO_4^{3-} are not shown, as these are usually hidden by the band from ν_1 mode of B-type carbonate. Used with permission of SPIE, from *Identifying compositional and structural changes in spongy and subchondral bone from the hip joints of patients with osteoarthritis using Raman spectroscopy*, Tomasz Buchwald et al., Journal of Biomedical Optics Vol. 17, Issue 1, 2012; permission conveyed through Copyright Clearance Center, Inc.

2.11 Teeth

While not considered bones, teeth are considered as part of the skeletal system. While some morphological features, such as the number of roots, differs between various teeth, the general structure remains the same. A collagenous connective tissue, know as the peridontal ligament (PDL), suspends each tooth in a bony socket, know as the alveolus. The region of the bone within the alveolus is know as the root, while the one outside of it (visible in the oral cavity) is know as the crown. The portion between these two sections is known as the cervix. A tooth can be divided into two parts, a mineralised component consisting of three different calcified substances, which in turn encapsulates a soft, highly vascularized and innervated gelatinous connective tissue known as the pulp. [9]

Its the mineralised component that has the structure closest to bone, consisting primarily of HAp and collagen. Unlike bone however, teeth consists of multiple different mineralised substances. These are enamel, dentin, and cementum. Dentin surrounds the pulp, and composes the bulk of a tooth's mineralised substance. It is covered by enamel on the crown, and by cementum on the root. [9]

Enamel is the hardest substance in the body, and consists of 96% HAp, and 4% organic material and water. The HAp crystals are large, and each is coated in a thin layer of organic matrix. This matrix consists of glycoproteins, as well as proteins such as enamelins, amelogenins and ameloblastins. The body cannot repair enamel, as the cells that create the tissue, the ameloblasts, die after the maturation of the tooth, which happens before the tooth erupts into the oral cavity. [9, 82]

The second hardest substance in the body is dentin. It is composed of 65-70% HAp, 20-25% organic material, and around 10% bound water. The organic substance is almost exclusively composed of type I collagen, with the remainder consisting of proteoglycans and glycoproteins. Another similarity dentin have with bones is that the cells that produces it, odontoblasts, remain functional after the tooth has been made. This gives dentin the ability to self-repair. Odontoblasts can be found at the periphery of the pulp, with cytoplasmic processes extending into the dentin through tunnel-like spaces. [9, 82]

The last mineralised substance in teeth is cementum, which is composed of 45-50% HAp and 50-55% organic material. The organic material primarily consists of collagen of type I, III and XIII, as well as their associated proteoglycans and glycoproteins. One part of cementum, known as cellular cementum, is similar to bone in that the tissue houses cells, cementocytes, withing lacuane, with processes from these cells extending towards the vascular PDL through canaliculi. The part of cementum without these cells are called acellular cementum. Both types of cementum are covered in cementoblasts (at the interface with the connective tissue), cells that produces cementum throughout the life of the tooth. Cementum can also be resorbed by odontoclasts, osteoclasts-like cells. Along with alveolar bone and periodontal ligament, cementum forms the attachment apparatus of the tooth. [9, 82]

2.12 CARS setup

As the CARS microscope used during the duration of this masters wasn't a commercial microscope, but instead a homemade setup, this setup will be described below. See Figure 2.12.1 for a simplified schematic. The microscope consisted of many different components. It had two lasers, a pump laser a Stokes laser. An electro-optic modulator (not shown in the schematic) had the function of controlling the power, phase, and polarization of the lasers. Both lasers were also connected to a cooling system (not depicted in the schematic) which kept them at a certain degree so they did not overheat.

The different scanning mirrors had the function of aligning the two lasers on the sample, as well as to control any delay between them. These were controlled by a beam diameter galvo system.

The CARS system had two detectors, one below the sample, which detected the signal in the trans direction, and one above the sample, which detected the signal in the epi direction. Both CARS detectors were connected to each their PMT controller and power supply, which had the function of amplifying the signal detected from their respective detector, and then send it on to a computer where the signal could be processed.

The main dichroic cubes and CARS filter cubes above and below the sample were used to filter out all unwanted background signal from hitting the two detectors. The dichroic cubes reflected all signal underneath a certain wavelength towards the detectors, while the filter cubes would function as absorption filters, only letting a narrow band of wavelengths through to the detectors.

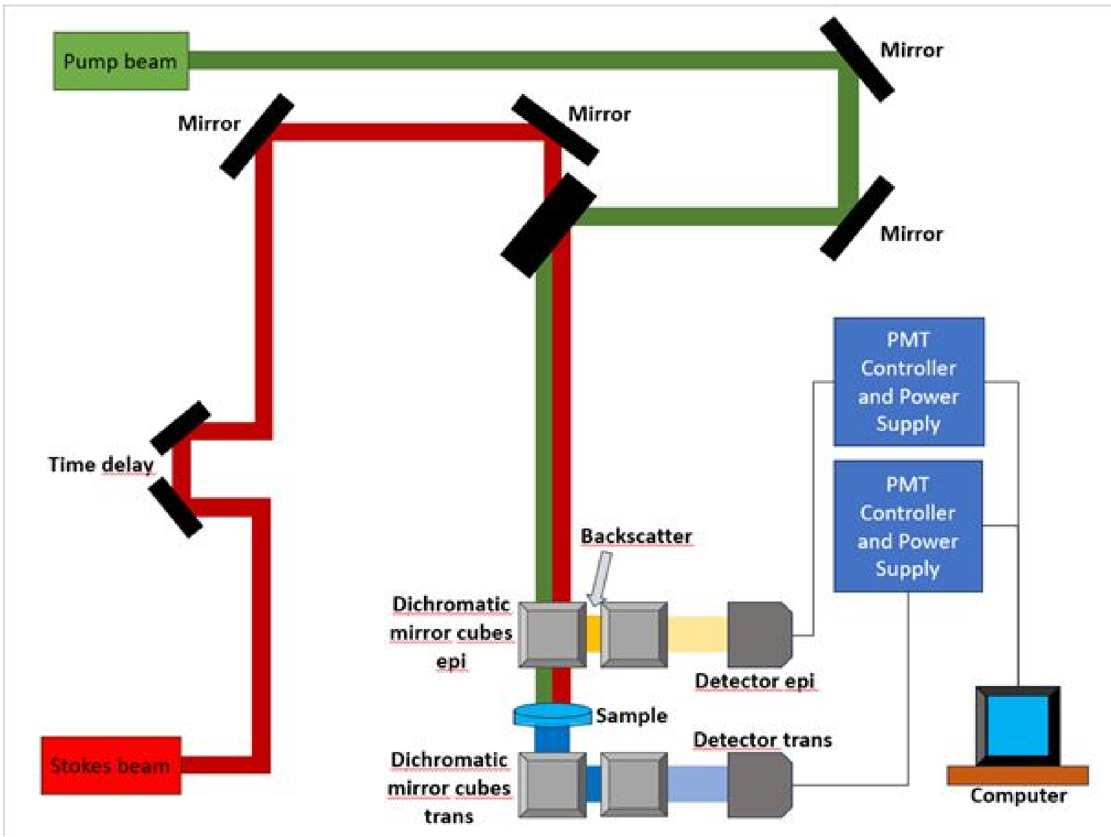

Figure 2.12.1: Setup for the CARS microscope.

CHAPTER

THREE

MATERIAL AND METHODS

3.1 Sample Preperation

Some results obtained during the author's specialisation project (TFY4520) were used in this thesis. These were collected from a sample consisting of 10 mg Dicalcium Phosphate Dihydrate (DCPD) in 1 ml NaCl-solution made by constructing a simple flow cell, see Figure 3.1.1. 5 μl of the sample was placed on a microscope slide, and a coverslip was then mounted on-top of the sample, held in place by double-sided tape. A 1M $CaCl_2$-solution, made by mixing 29.4 g CaCl (CAS 10035-04-8) in 200 mL deionized water, was then added underneath the coverslip. The edges of the coverslip was then sealed using nail polish.

The bone samples studied were prepared by Catherine A. Heyward and Hanna Tiainen from the University of Oslo's Faculty of Dentistry. Some of these samples included two separate dog jaw sections, one rabbit leg section, two different bone marrow biopsies, and one bone nodule, all embedded in methyl methacrylate (MMA). After extraction, the samples were first dehydrated in an ascending series of alcohol and xylene baths, before being embedded in MMA and polymerised at -20°C. Polymerising means the process in which monomer molecules react together to form a polymer, here with the MMA molecules coming together to form Polymethyl Methacrylate (PMMA). The samples were then sectioned into thinner sections using a motorised rotary microtome. [83] The exact thickness varied between the samples, and weren't always known. It should also be noted that all traces of fat and fat cells in the samples should have been removed during this process (according to those who prepared the samples).

Catherine A. Heyward and Hanna Tiainen from the University of Oslo's Faculty of Dentistry also prepared a decalcified rat jaw section. Decalcification means that calcified minerals were removed from the sample, here HAp. After euthanasia of the specimen the sample originally belonged to, the upper jaw (maxilla) was dissected and immediately placed in fresh formaldehyde for 48 hours. After fixation, the samples taken from the tissue were washed in water and immersed in 10 % EDTA at pH 7.4 (the decalcification process). After decalcification, the samples were further sectioned to separate the right and left side of the maxilla, and the specimens were then serially dehydrated in ethanol and embedded in paraffin. Tissue sections of 5-µm thickness were prepared as cross-sections cut parallel to the long axis of the first molar. [84]

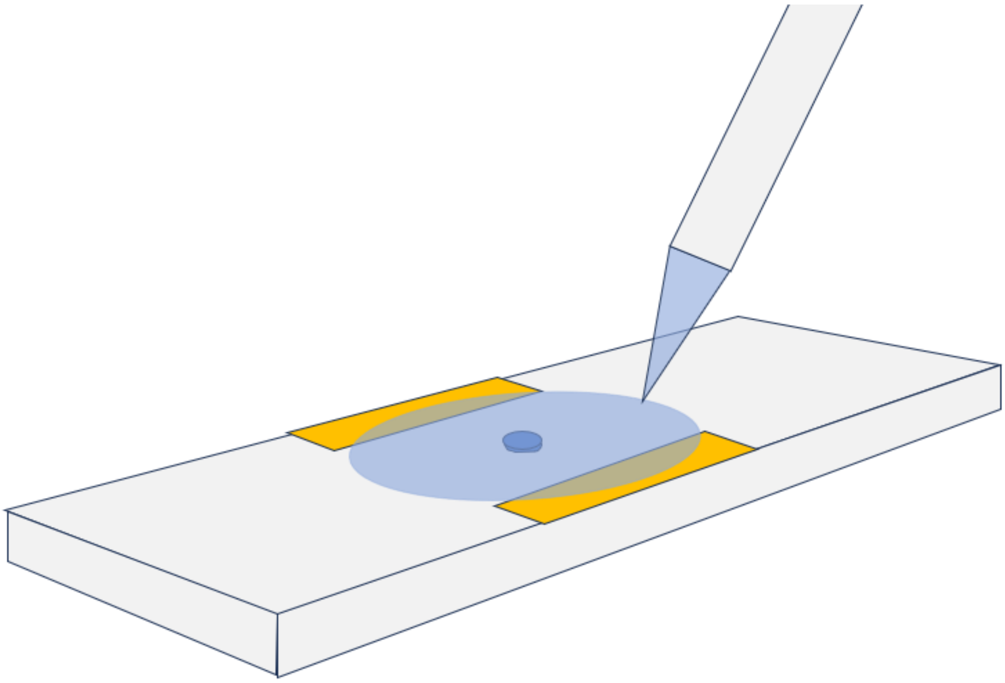

Figure 3.1.1: Illustration of a simple flow cell.

Two other samples which were studied, prepared by Marie Eline Ullevålseter from NTNU's Faculty of Natural Sciences, consisted of a layer of MC3T3-E1 preosteoblasts which had been cultured for either 21 and 31 days. The sample which had been cultured for 21 days was stained using ARS, while the one cultured for 31 days was not. The cells were cultured in TC75 flasks (Thermo Fisher Scientific) with Minimum Essential Medium Alpha Medium (Gibco 22571 for the stained sample, Gibco A10490-01 for the non-stained sample) and fetal bovine serum (Thermo Fisher Scientific). 50 mL of fetal bovine serum was added to 500 mL of media. The cells were cultured at 37°C with 5 % CO_2 and at least 95 % humidity. The differentiation media was supplemented with 2 mM β-glycerol-2-phosphate (Sigma-Aldrich) and 50 µg/mL L-ascorbic acid-2-phosphate (Sigma-Aldrich). The cell cultures were seeded on round cover glasses with 20 mm diameter in well plates. The cover glasses and tweezers were sterilised with 70 % ethanol. 35000 cells were seeded in each well. The media was exchanged every second to third day. The sample that was to be stained, was transferred to a 35 mm Petri dishes with its media before staining. After the glass slip was moved the media was aspirated, and the cells were then washed with phosphate buffered saline. 1 ml 4 % paraformaldehyde (Sigma-Aldrich) was then used to fix the cells for 15 minutes. The sample was washed twice with water before adding 1 ml of an ARS solution. The sample was left in the solution for 20 minutes before removing the excess, and was then washed by gently lowering the bottom of the Petri dishe in a water bath and gently rinsing until no more stains were coming from the sample. The sample was stored in water at 4 °C . The ARS solution was made by dissolving 0.50 g ARS powder (Sigma-Aldrich) in 25 ml of water to make a 2%(w/v) solution. It was mixed for 10 min on a rolling board. The pH was then measured to be 5.0 with a pH-meter. The solution was then filtered through Acrodisc syringe filters with a 0.2 µm membrane (Pall).

3.2 Starting the system

When starting the CARS microscope, there was a certain order things had to be done:

1. The pump and Stokes beams/lasers were both turned on from standby mode, and allowed to warm up for 15 min. The cooling system for the lasers also had to be checked, in order to make sure that both lasers kept a temperature of 30°C.

2. The power strip that powered all of the following parts was turned on.

3. The electronic unit from NI was turned on, along with the computer.

4. The small beam diameter galvo system was turned on, which in turn turned on the scanning mirrors.

5. The electro-optic modulator was turned on.

6. The PMT power supplies (Hamamatsu C10709) for both the epi and trans laser was turned on, though first one had to make sure that the voltage control buttons were off.

7. The shutter power supply (control unit KSC101, ThorLabs) was turned on. If set to manual mode, its wheel was set to its upper position while scanning.

8. The control unit (KDC101, ThorLabs) for the sub-stage condenser motor was turned on.

9. If not already on (from turning on power strip), the control for the z-motor was turned on.

3.3 Bright field

The bright field microscope had two primary functions; to give and overview of the sample that was going to be analysed, and to focus and centre the aperture in the sample plane. First, the main dichroic mirror cube for the epi signal had to be removed, and the camera cube had to be inserted (see Figure 3.4.2) The sample that was going to be analysed was place in the sample holder, and a water droplet was added to the cover glass. The objective of the microscope was then lowered into to water droplet. The sample was then focused on with the camera, using a green LED light and ThorCam. Exposure time, light intensity and contrast was then adjusted as necessary. Then, the Kohler was adjusted by closing the field aperture until the edge of the light was clearly visible, for then to centre the aperture in the middle of the image using the micrometer screws shown in Figure 3.4.4. If the edges of light were blurry/not visible when closing the field aperture, the sub-stage condeser motor was used in order to focus the aperture in z-direction. The lens used to focus on the sample had an magnification of 25X.

3.4 CARS microscope

After the aperture had been centred and focused using the bright field microscope, the green LED light was turned off, and the camera cube for the bright field microscope was removed. The appropriate dichroic mirror cubes and filter cubes was then placed in both Trans and Epi locations (see Figure 3.4.3 and Figure 3.4.2 for setup). The light was then turned of, and the lasers were calibrated using ScanImage. The pump signal was then set to its appropriate wavelength. ScanImage was then used to capture the CARS-image received when the lasers were focused on the sample. Unidirectional scan was used at all image acquisitions.

In order to detect CARS signal from calcium phosphate in HAp, literature values, as well as values found by scanning calcium phosphate crystals using the CARS during the author's specialisation project (TFY4520), set the strongest Raman shift at around 988 cm^{-1}. Using Equation 2.15, the value for λ_{pump} was then found to be at 935.7 nm. λ_{CARS} was then calculated using Equation 2.15 to be 856.5 nm. The main dichroic cubes were therefore set to reflect all wavelengths beneath 875 nm, and the reflected light was then filtered using 857 ± 15 nm filters. There was however not enough filter cubes (with the correct filters) available to have both a trans and epi filter at 857 nm. A 857 nm filter was therefore placed on the left side of the main dichroic epi cube so that it in theory should be able to work as both a dichroic cube and a filter cube. This however meant that the epi detector had to change place to the left side of the dichroic epi cube when scanning a calcium phosphate sample. However, late into the master it was discovered that the filters in the dichroic epi cube had been mounted incorrectly, reflecting most epi signal that would have reached the cube in the wrong direction, away from the detector.

Using the work done in author's specialisation project (TFY4520), the optimal delay between Stokes and Probe laser pulses for calcium phosphate crystals was found to be around 2500 fs. This value was therefore first used when imaging the bone samples. Later, the optimal delay for scanning HAp in bone was found during testing.

For CH-bindings, literature values set the Raman shift for CH stretching at somewhere between 2800-3000 cm^{-1}. λ_{pump} was therefor set to different values between 787.4-800.0 nm. The optimal value was found during testing, which was then used for imaging of the samples using CARs signal coming from CH stretching. The main dichroic cubes were therefore set to reflect all wavelengths beneath 695 nm, and the reflected light was then filtered using 643 ± 15 nm filters (see Equation 2.17 for how to find λ_{CARS}). Here, enough filter cubes with the correct filters were available, so the setup for capturing signal in both trans and epi direction was the same (one dichroic cube and one filter cube), with the epi detector placed on the right side.

The datasets collected using CARS consisted of numbers representing the signal strength at each pixel of the area scanned. These values are then converted into an image using a colourmap. Here, greyscale was used when imaging the datasets, meaning black in the CARS images represents the lack of signal, while different shades of grey/white represents signal at different strengths. The brighter the grey, the stronger the signal.

Multiple spectra showing the intensity of CARS signal acquired at different wavelengths for the pump laser were made. This was done by scanning the sample while the pump laser was set to many different wavelengths within the limit values of the filter. The intensity of each signal were then analysed, both for the whole image acquired, as well as for smaller areas. This was only done for the trans signal, as non of the samples scanned gave much of an epi signal. This type of spectra were also acquired at different values of delay between when the Stokes and Probe laser pulses hit the sample. λ_{pump} was here constant. The value for the signal strength was acquired by adding together all numerical values in the CARS dataset. Both types of spectra were made when studying both HAp and CH-bonds.

At certain points, spectra which studied the signal strength for HAp when λ_{pump} was below 927 nm (v_{vib} below 1088 cm^{-1}) were made. For this, a filter cube with a 832 ± 18 nm filter was used alongside the 857 ± 15 nm filter in trans direction. This made it possible to use λ_{pump} down to 909.8 nm, and therefore study wavenumber signals up to 1292.1 cm^{-1}.

Background signal was collected by finding an area where no HAp was present in one of the samples, for then to collect multiple datasets at different values of λ_{pump}. Here, this was done in an interval of 909.0-944.8 nm. A background signal spectrum was then made. By subtracting this spectrum from a spectrum made within the same interval from one of the bone samples, a new spectrum which in theory should be showing the CARS signal from the sample without any background signal was acquired. The area in which both signals were collected were of the same size.

At one point during the master's, the lasers were re-aligned (if the two beams didn't hit the sample with perfect overlap, then the CARS signal would become weaker). As this could have led to changes in the CARS signal received, it will be noted when results has been gained after this re-calibration.

The CARS signal coming from HAp and CH-bonds from the same areas were at certain points compared by overlaying the signals coming from both sources ontop of each other, using different colourmaps for each signal type (blue for HAp, red for CH-bonds. In order to normalise the brightness/contrast of the colours for both signals, the background signal from areas where barely any signal was detected was removed, and any signal coming from pixels with abnormally large signal values (usually caused by saturation of the detector), were changed to a more reasonable value. This was all done using python (see Figure 3.4.1 for code).

3.4.1 Setup

The CARS microscope used during the duration of this masters was not a commercial microscope, but was instead a homemade setup. It had two lasers, one designated OPO (pump laser) and one designated IR (Stokes laser). Both lasers were made by APE. An electro-optic modulator had the function of controlling the power, phase, and polarization of the lasers. Both lasers were connected to a panel PC separate from the rest of the CARS system, which used the picoEmerald (ver. 4.10.0.65) software from APE to control the individual power output (in mW) of the lasers, the wavelength of the pump laser, any delay between the lasers' pulses, and if the laser shutter was open or closed. The Stokes laser always had a wavelength of 1031 nm. Both lasers were connected to a cooling system which

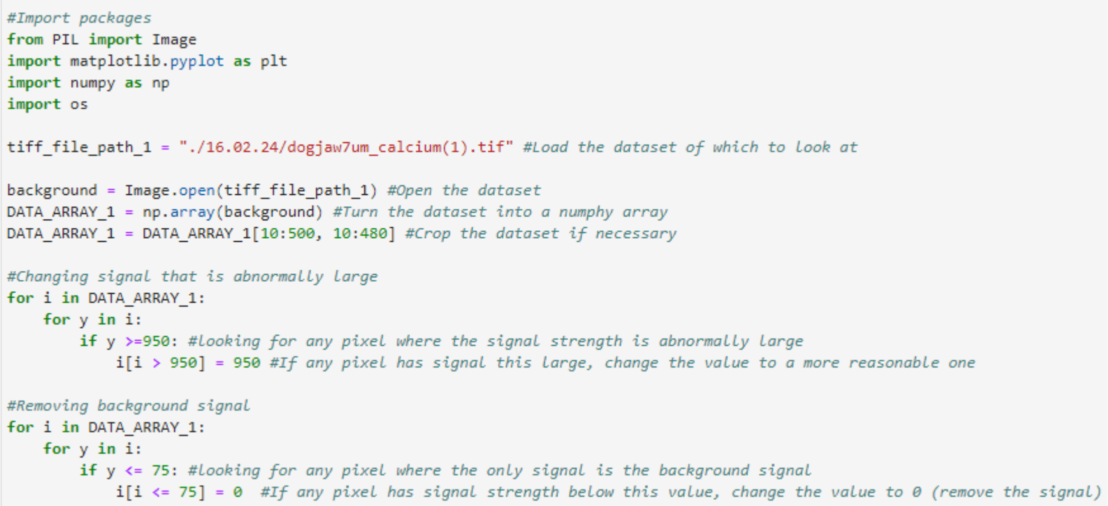

```
#Import packages
from PIL import Image
import matplotlib.pyplot as plt
import numpy as np
import os

tiff_file_path_1 = "./16.02.24/dogjaw7um_calcium(1).tif" #Load the dataset of which to look at

background = Image.open(tiff_file_path_1) #Open the dataset
DATA_ARRAY_1 = np.array(background) #Turn the dataset into a numphy array
DATA_ARRAY_1 = DATA_ARRAY_1[10:500, 10:480] #Crop the dataset if necessary

#Changing signal that is abnormally large
for i in DATA_ARRAY_1:
    for y in i:
        if y >=950: #Looking for any pixel where the signal strength is abnormally large
            i[i > 950] = 950 #If any pixel has signal this large, change the value to a more reasonable one

#Removing background signal
for i in DATA_ARRAY_1:
    for y in i:
        if y <= 75: #Looking for any pixel where the only signal is the background signal
            i[i <= 75] = 0  #If any pixel has signal strength below this value, change the value to 0 (remove the signal)
```

Figure 3.4.1: An example of python code which can be used to remove background signal, as well as change abnormally large signal in a dataset acquired using a CARS microscope.

kept them at 30°C.

An electronic unit from NI was used to powered the computer that control the CARS system and the brightfield camera. The computer used the ScanImage-software for controlling the CARS, and ThorCam-software for controlling the brightfield camera.

The different scanning mirrors used to aligning the two lasers on the sample, as well as to control any delay between them, were all connected to a small beam diameter galvo system from ThorLabs, which controlled them all.

The setup for filters, detectors, objective and other microscope related components is a little more complicated. See Figure 3.4.2, 3.4.3 and 3.4.4 for images of this setup. All of Figure 3.4.3 and 3.4.4 are set up below the sample. The CAM unit is the brightfield camera, the Epi PMT is the signal detector for the CARS epi-signal, and the Trans PMT is the signal detector for the CARS trans-signal. The CAM cube was used to reflect light into the brightfield camera. The light used for the brightfield came from the LED in Figure 3.4.3. The main dichroic cubes and CARS filter cubes were used to filter out all unwanted background signal from hitting the two detectors. Both CARS detectors were connected to each their preamplifier (pre-amp in images), which in turn passed the signal from the detectors to a PMT power supply (Hamamatsu C10709, one for trans and one for epi). In Figure 3.4.4, the condenser screws and control unit (KDC101, ThorLabs) for the substage condenser motor are shown.

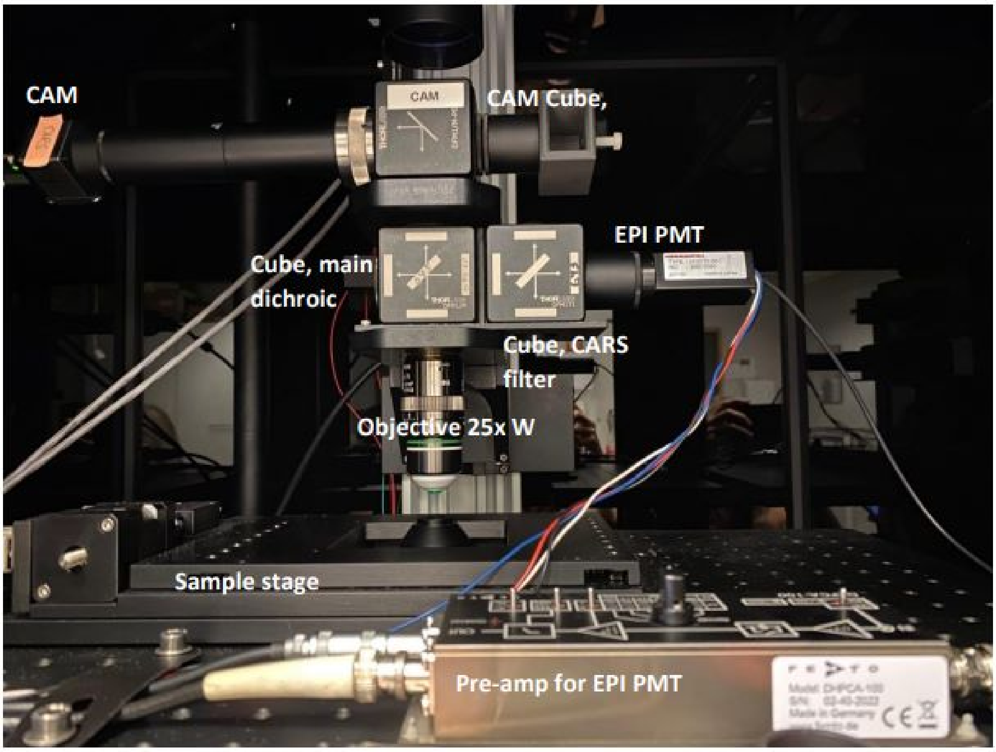

Figure 3.4.2: Setup for the brightfield camera, brightfield camera cube, preamplifier for epi PMT, epi main dichroic mirror cube and filter cube, and epi detector (EPI PMT).

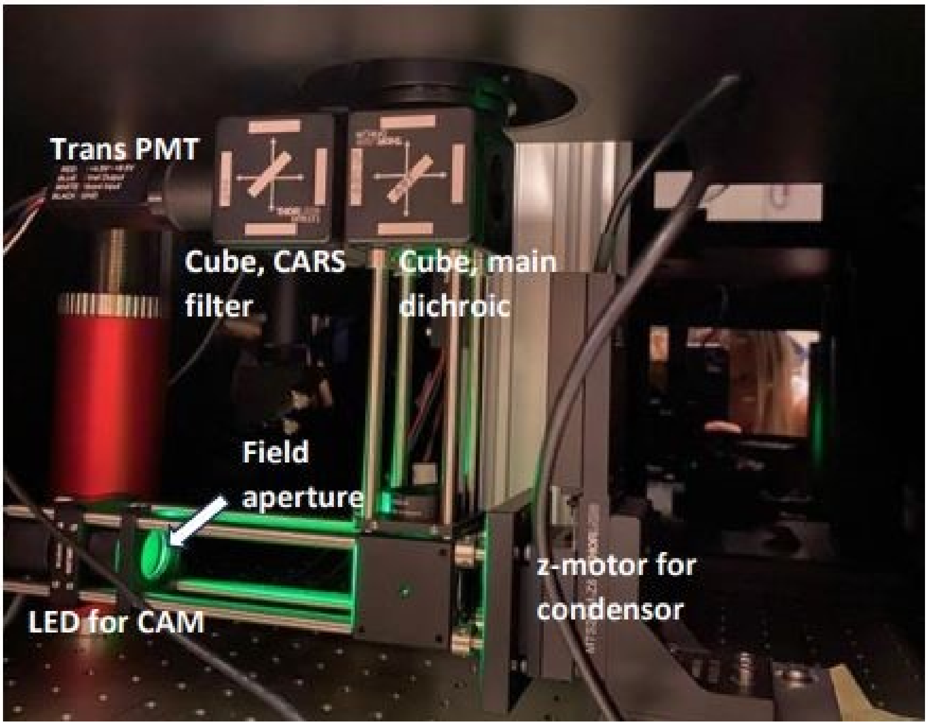

Figure 3.4.3: Setup for the LED light, field aperture, z-motor for condenser, trans main dichroic mirror cube and filter cube, and trans detector (EPI PMT). This is all placed underneath the sample.

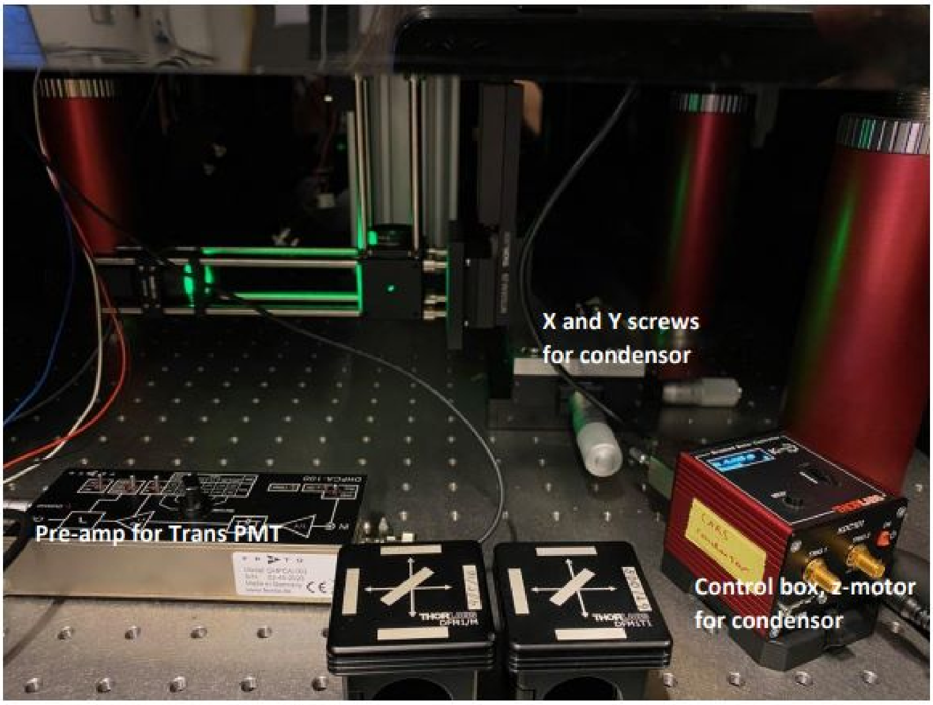

Figure 3.4.4: Setup for preamplifer for trans PMT, the screws used to control the direction of light beam from condenser (x- and y-direction), and the z-motor control box used to control the z-position of the condenser. This is all placed underneath the sample.

A shutter power supply (control unit KSC101, ThorLabs) was also connected to the system. When its wheel was in the upper position, a shutter stopping the lasers from hitting the sample would be open.

There was a control unit for the sample stage that controlled its the position of the sample in z-direction. The control for x- and y-position did not function.

3.4.2 Settings

The CARS microscope had many different settings that could be changed. Below is a list of some of these setting:

1. The individual output power of the pump and Stokes laser in mW. Set to 350 mW for both lasers.
2. The time the focused laser beams rested on a single pixel and illuminated it, known as pixel dwell time. Set to 3200 ns.
3. Zoom, which increased the magnification of the area scanned. Normally set to 1.
4. The fill fraction, another type of zoom function, which increased or decreased the magnification to a much smaller degree than the zoom function. Set to 0.400.
5. The number of pixels per line scanned. Set to 512 pixels/line.

6. The overall power of the lasers that the sample was illuminated with, in %. Set to around 60 %.
7. The delay between when the second and third laser pulse from the lasers hits the sample. At 0 delay, they hit at the same time, at $delay > 0$ the pulse from the Stokes laser hits first, and at $delay < 0$, the second pulse from the pump laser hits first. Delay times between 0 and 10000 fs were tested. The optimal value was found during testing.
8. Number of accumulations used for the averaging of an area scan. Set to 32 accumulations.
9. The use of either bidirectional or unidirectional scan (explained in subsection 3.4.3).

3.4.3 Bidirectional and Unidirectional Scan

Bidirectional scan and unidirectional scan are two different way for image acquisition for CARS and other laser microscopes. The difference between them is based of how they scan each "line" of a sample. Unidirectional scan starts the scan of each line on the same side (the left side for the CARS microscope used here). This means that the laser has to "jump" back to the other side of the scan area each time it is going to start a new line. While this means that the distance the laser travels, and thus the acquisition time, is longer, this helps preserve spatial information during imaging. Bidirectional scan on the other hand has the beginning of a new line be at the same side as the last line ended. While this increase the scanning speed, it also deteriorates the spatial information. Because of this, unidirectional scan was the preferred method of scanning used. Both scan methods are depicted in Figure 3.4.5. [85]

3.5 Micro-Raman

Using the principles of micro-Raman, a Raman microscope was used to find the Raman spectra for the different bone and tooth samples. Witec AS was the manufacturer of the Raman microscope used (model Witec Alpha 300r). A 532 nm laser (100mW) with a 600 grooves/mm grating was used to analyse the samples. The Witec Control Five 5.2 software was used to control the RS and analyse the results gained from it. Using this software, the number of accumulations that would be used when creating the Raman spectrum was set to 6, the integration time was set to 10 seconds per accumulation, and the laser power was set to 10 mW. The interval of wavenumbers that were tested was between 0-3800 cm^{-1}. For a normal scan, the sample was first put under a brightfield microscope at either 10X or 50X magnification. If possible, the brightfield was used to focus on the sample. If this wasn't possible, due to for example the sample's surface structures not being visible in the brightfield at such a high magnification, the focus was instead found by letting the Raman microscope continuously scan the sample while changing the focus, in order to find the height that gave the best signal in the form of a Raman spectrum. A larger area map was then made by combining multiple pictures taken at the chosen magnification. One could then

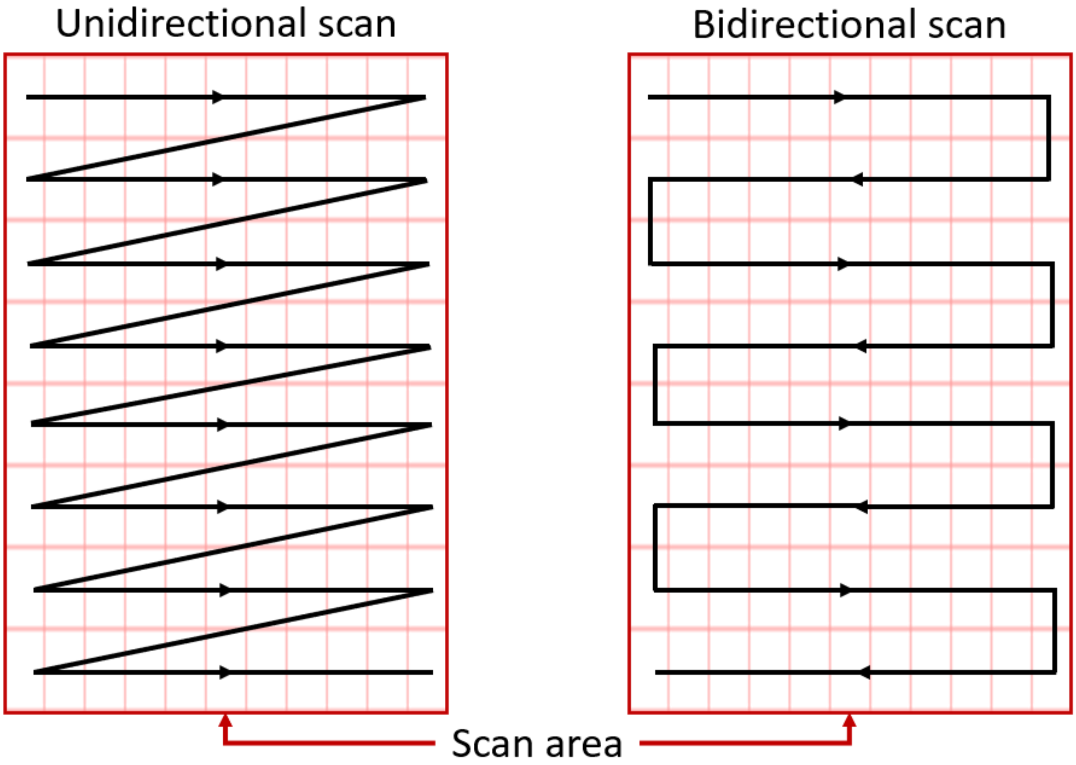

Figure 3.4.5: Unidirectional and bidirectional scanning.

chose the points one wanted to scan on the sample by picking them from the area map.

CHAPTER

FOUR

RESULTS

4.1 DCPD

As part of the author's specialisation project (TFY4520), a Dicalcium Phosphate Dihydrate (DCPD) sample was imaged using the CARS microscope. The sample was scanned at different values of delay between 0 and 5000 fs, as well as at different λ_{pump} values between 933.5-943 nm, in order to find which delay and wavenumber gave the strongest signal (by transforming the wavelength values found here to wavenumber using Equation 2.15 the corresponding wavenumbers were found). Delay here means the time between when the second laser pulse from the pulse laser (also known as the probe pulse) hits the sample after the Stokes laser. The delay becomes important when the CARS signal generated by the sample is weak enough that a so called non-resonant background signal can become stronger than it (see section 2.5 for an explanation into how this background signal is created). As explained in section 2.5, one can decrease the amount of non-resonant signal generated by the sample by increasing the delay. However, increasing the delay to much may also decrease the amount of CARS signal generated. Therefore, it was important to find the delay that gave the strongest CARS signal. An image of a sample containing the DCPD crystal is shown in Figure 4.1.1. It was found that calcium phosphate crystals gave the strongest CARS-signal at 2500 fs delay, and that they gave the strongest CARS signal at around 988 cm^{-1} (λ_{pump} = 935.7 nm). This signal corresponds to the ν_1 vibrational stretching mode for PO_4^{3-} normally detected with Raman spectroscopy [32, 33, 34]. It should be noted that the range of vibrations explored was narrow (between 905.1-1013 cm^{-1}), being close to the vibrational peak for calcium phosphate found in literature. As a CARS signal was acquired from the DCPD crystals, and it was strong enough to give detailed imaging of the crystals, the work of the master thesis focuses on testing different bone, teeth and bone cell samples with the CARS microscope.

4.2 Samples

As the CARS technique had proven itself to work for imaging of calcium phosphate, one would like to see if the technique worked for bone and bone related samples, as well as to figure out what kind of information one could gain using CARS.

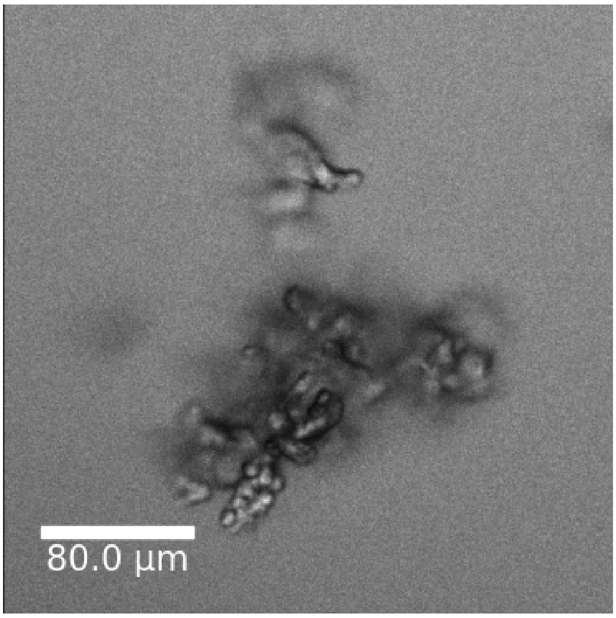

Figure 4.1.1: An image of a calcium phosphate crystal made using CARS. Taken during the author's specialisation project (TFY4520). The image was captured at 988 cm^{-1}. $\lambda_{pump} = 935.7$ nm, $\lambda_{Stokes} = 1031$ nm, delay = 2500 fs.

Because of this, many different samples were studied using the technique. The different samples were:

1. Two dog jaw sections embedded in Methyl Methacrylate (MMA). One was a 7 µm section cut by microtome. The other one of unknown thickness (though much thicker than 7 µm) with surrounding soft tissue. The thicker sample was embedded in a much thicker layer of MMA than the 7 µm section.
2. A 5 µm decalcified upper rat jaw bone section with surrounding tissue, embedded in paraffin.
3. A rabbit leg bone sample embedded in MMA. The exact thickness was not known, though it was around the same thickness as the thicker dog jaw section.
4. Two bone marrow biopsies of differing thickness, embedded in MMA. One had a thickness of 10 µm, while the other's thickness was somewhere between 7-20 µm.
5. One bone nodule (level 1 arthritis), embedded in MMA.
6. Two samples consisting of MC3T3-E1 preosteoblasts which had been cultured for either 21 or 31 days, so that the cells had created HAp mineralized extracellular matrix. One of the samples was stained using ARS (cultured for 21 days), while the other wasn't (cultured for 31 days).
7. Multiple human tooth sections. Eye measurements put them at a thickness around 0.5 mm. They were not embedded in anything.

4.3 Micro-Raman

Before testing the different bone and tooth samples with the CARS microscope, Raman spectra were collected for all samples using a Witec Alpha 300r Raman microscope. As explained in the theory section, a Raman microscope can be used for the identification and analysis of physical and chemical properties of a sample by the acquisition of a spatially resolved Raman spectra. This was done in order to confirm the wavenumbers which gave Raman active vibration from the samples, and to compare these results with the results from CARS microscopy. With the brightfield, the samples were focused on using first 10X and then 50x magnification. Where possible, the brightfield camera was used to focus on the samples. If this wasn't possible, the focus was instead found by letting the Raman microscope continuously scan the sample while changing the focus, in order to find the height that gave the best signal in the form of a Raman spectrum. Which method that was used depended on the sample. The spectra were made for the wavenumber interval between 200-3200 cm^{-1}.

Each of the Raman spectra collected was taken from the average over a selected region of around 1-10^2 μm^2. While multiple spectra were made for each sample from different regions, they all showed very similar results for each sample. Because of this, only one spectra collected from each sample is shown unless otherwise specified.

The Raman spectra made from the dog jaw 7 µm section can be seen in Figure 4.3.1. While some of the spectra had a little more background signal than the others, all of them had the same peaks. Most of these peaks fit well with the literary values for the Raman active vibrations found in bone tissue. These were the peak at 600cm^{-1} (ν_4 mode, PO_4^{3-}), the peak around 967 cm^{-1} (ν_1 mode, PO_4^{3-}), the many smaller peaks between 1200-1300 cm^{-1} (amid III), and the peak at 1450 cm^{-1} (CH bending). Some of the other peaks didn't fit quite a well, but might still have corresponded to known Raman peaks in bone. The peak at 1120 cm^{-1} might correspond to either A-type carbonate or ν_3 mode for PO_4^{3-}, while the peak at 1730 cm^{-1} might correspond to amid I. The one peak that did not fit the know Raman spectrum for bone was the one found at 810 cm^{-1}. While this might have correspond to proline and/or hydroxyproline, the signal strength was much higher than expected. A reason for this might be the embedding MMA, as MMA has a Raman peak at around 850 cm^{-1}. One can also see a peak at around 3000 cm^{-1} (much larger than any of the other peaks, see Figure 4.3.1b), which may have come from CH stretching. Why the ratio between the peaks is so different than that seen in Figure 2.10.1 was unknown, but may have been due to Raman signal created by background signal from the embedding MMA, as MMA has its strongest Raman active vibrations around this wavenumber. This background signal will be discussed in a bit.

The Raman spectrum for the thicker dog jaw section can be seen in Figure 4.3.2. The peaks found here are at 600 cm^{-1} (ν_4 mode, PO_4^{3-}), 820 cm^{-1} (might correspond to proline or hydroxyproline), 960-970 cm^{-1} (ν_1 mode, PO_4^{3-}), 1455 cm^{-1} (CH bending), 1727 cm^{-1} (amid I), and 2950 cm^{-1} (CH stretching). If the 820 cm^{-1} were from proline or hydroxyproline, the signal strength was much higher than expected. There was also more background signal coming from the sample. This can be seen by how the strength of the base line (the intervals between

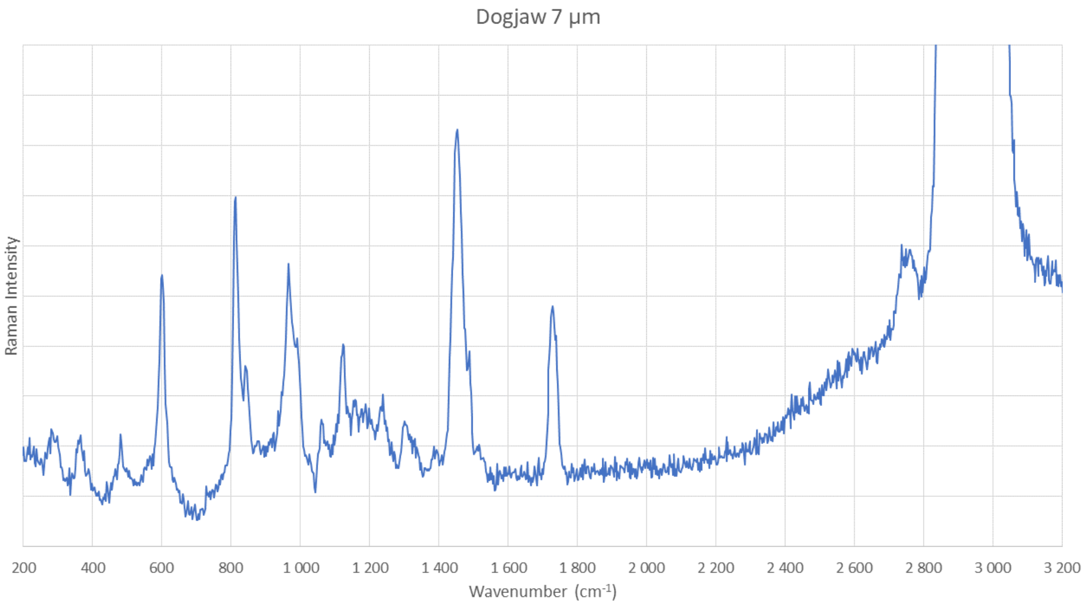

(a)

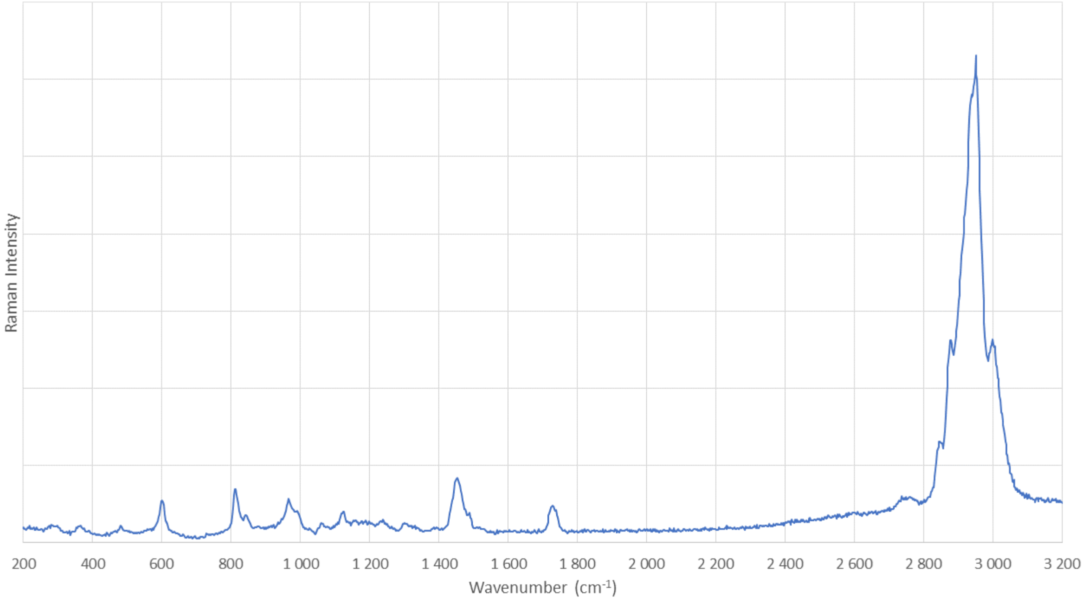

(b)

Figure 4.3.1: Raman spectrum of a 7 µm dog jaw bone sections cut by microtome, and embedded in MMA. The scale for Raman intensity is based on the second highest peak in (a), and the highest peak in (b). Captured using a Raman microscope (Witec Alpha 300r) from a single point of trabecular bone, 532 nm laser, 600 grooves/mm grating, 10 mW laser power, 6 accumulations, 10 s acquisition time.

the peaks) of the Raman signal seems to be increasing as the wavenumber increases, even though the signal strength in these intervals in theory should have very similar values. This background signal may come from two different sources, fluorescence and/or non-resonant background signal. The reason the thicker dog jaw section creates more of these two types of background signal may have to do either with the thickness of the sample, and/or the thickness of the embedding layer of MMA.

In order to see if the MMA contributed any significant Raman signal that may affect the results recorder from the MMA embedded sections, the collection of the embedding MMA spectra was attempted. This however turned out to be more difficult than expected. For all MMA embedded samples, at least a thin layer of bone cells could be found almost everywhere in the sample, making it very difficult to gain a spectrum which didn't receive signal from either the bone tissue or the the glass slide. While some of these spectra showed small differences from the MMA embedded spectra (like a small peak at around 1000 cm^{-1}), it was difficult to say if this actually was because of the MMA or not. However, while investigating the two dog jaw sections, small areas without any bone tissue were found, and both of these areas gave very similar spectra, with the only difference being the size of the peaks when compared to the rest of the spectrum. One of these spectra can be seen in Figure 4.3.3. While this spectrum does contain some peaks that might fit with a typical PMMA Raman spectrum, such as peaks around 1000 cm^{-1}, 1170 cm^{-1}, 1320 cm^{-1} and 1415 cm^{-1}, it also lacks certain peaks typical for MMA, such as peaks at 600 cm^{-1}, 850 cm^{-1} and 1730 cm^{-1}, as well as clear peaks around 2700-3000 cm^{-1}. The spectrum also contain peaks not typical to the MMA Raman spectrum, such as a peak at 1570 cm^{-1}. As such, this spectrum does likely not belong to MMA. What molecule it might belong to, if any, was therefore unknown.

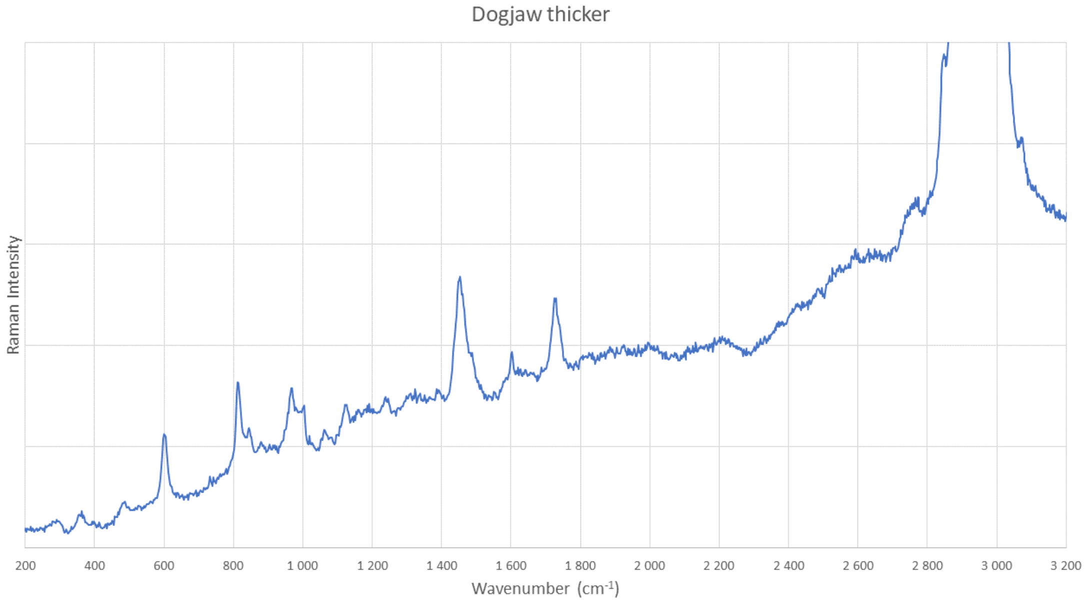

(a)

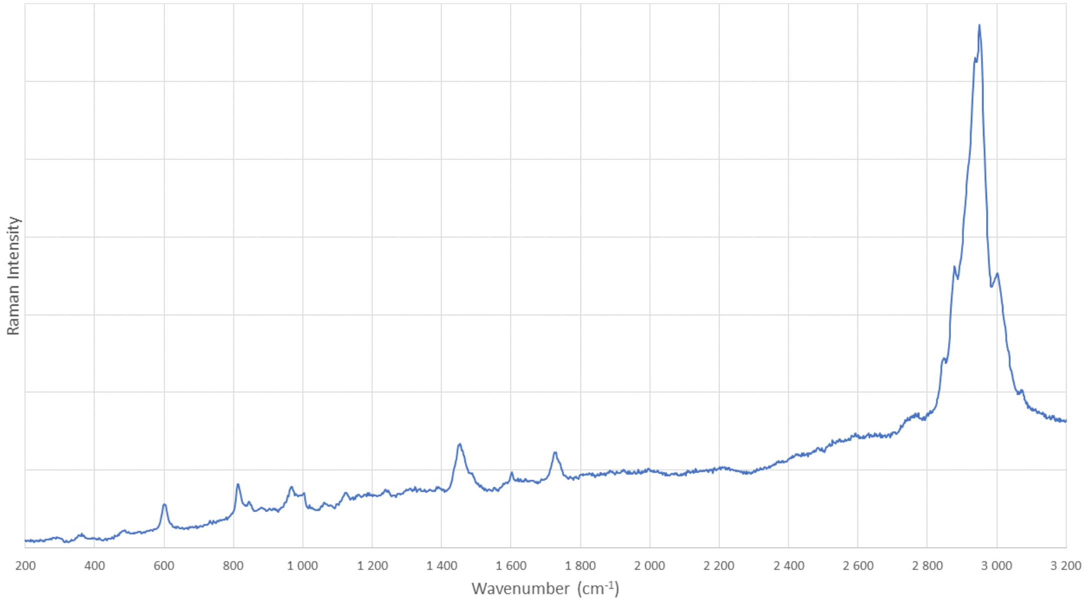

(b)

Figure 4.3.2: Raman spectrum of a dog jaw bone sample embedded in MMA. The scale for Raman intensity is based on the second highest peak in (a), and the highest peak in (b). Captured using a Raman microscope (Witec Alpha 300r) from a single point, 532 nm laser, 600 grooves/mm grating, 10 mW laser power, 6 accumulations, 10 s acquisition time.

The Raman spectra made from the decalcified rat jaw sample can be seen in Figure 4.3.4. This spectrum was collected from an arteriole, though a spectrum collected from a nerve bundle showed all the same peaks. Here, peaks were found at 890 cm^{-1} (might correspond to proline/hydroxyproline), 1060 cm^{-1} (ν_1 mode of B-type carbonate), 1140 cm^{-1} (might correspond to either A-type carbonate or ν_3 mode for $PO_4{}^{3-}$), 1290 cm^{-1} (amid III), 1440 cm^{-1} (CH bending), and 2880 $^{-1}$ (CH

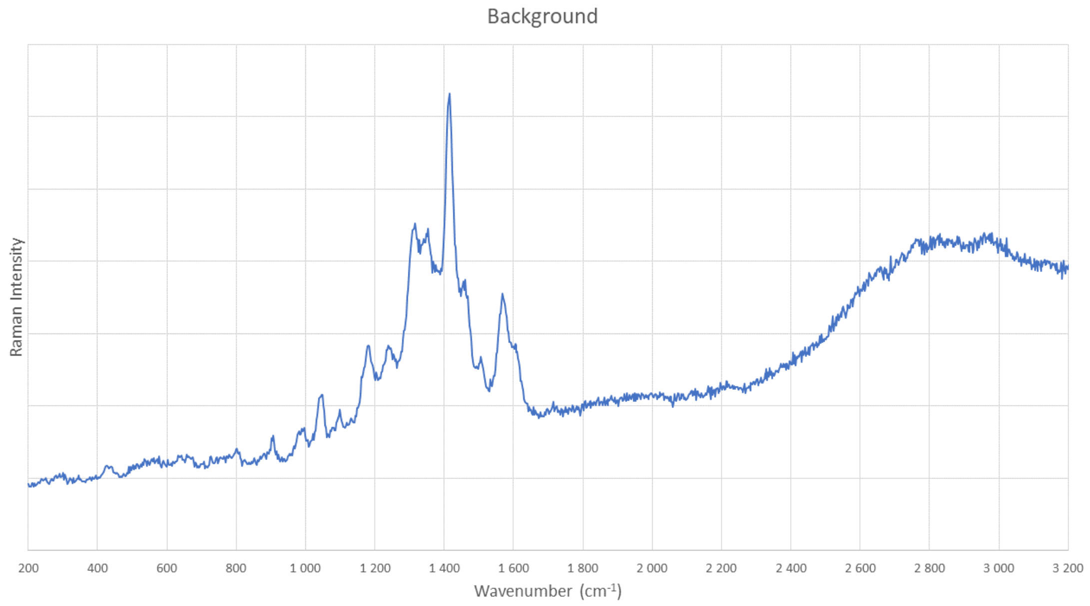

Figure 4.3.3: Raman spectrum of the background signal found in a dog jaw section embedded in MMA. Captured using a Raman microscope (Witec Alpha 300r) from a single point, 532 nm laser, 600 grooves/mm grating, 10 mW laser power, 6 accumulations, 10 s acquisition time.

stretching). Here, the relation between the 890 cm^{-1}, if it indeed corresponded to proline or hydroxyproline, and the other peaks were much more in line with what one would expect. While these spectra share some of the same peaks as the dog jaw sections, it lacked all peaks related to PO_4^{3-}. As this spectrum was collected from tissue where there normally should be little HAp, combined with the decalcification which further decreased the amount of HAp in the sample, the lack of peaks related to PO_4^{3-} was not surprising.

A spectrum collected from the tissue around the arteriole and nerve bundle was also collected, and can be seen in Figure 4.3.5. While all the peaks in Figure 4.3.4 can be seen here (with the exception of the 890 cm^{-1} peak, where it isn't as clear if what is shown is a peak or just background signal), multiple other peaks are visible as well. This includes what looks like small peaks at 560 cm^{-1} (ν_4 PO_4^{3-} bending modes) and 940 cm^{-1} (may correspond to the ν_1 PO_4^{3-} stretching mode), as well as a larger peak at 1660 cm^{-1} (amid I). As this tissue normally consists of primarily HAp, it makes sense that small peaks related to PO_4^{3-} are collected from this tissue. The amid I peak also makes sense, as the HAp in bone is arranged along type I collagen fibers, where amid groups can be found.

The Raman spectrum made from the rabbit leg sample can be seen in Figure 4.3.6. Just as with the thicker dog jaw section, there seemed to be more background signal coming from this sample as well. Still, it was possible to discern the peaks, which were found at 600 cm^{-1} (ν_4 mode, PO_4^{3-}), 820 cm^{-1} (might correspond to proline), 960-970 cm^{-1} (ν_1 mode, PO_4^{3-}), 1455 cm^{-1} (CH bending), 1727 cm^{-1} (amid I), and 2950 cm^{-1} (CH stretching). The peak that that might represent proline or hydroxyproline was again much higher than expected. The base-line for signal strength also seem to be climbing here as well, although less than the thicker dog jaw section. The reasons for the climbing base-line is proba-

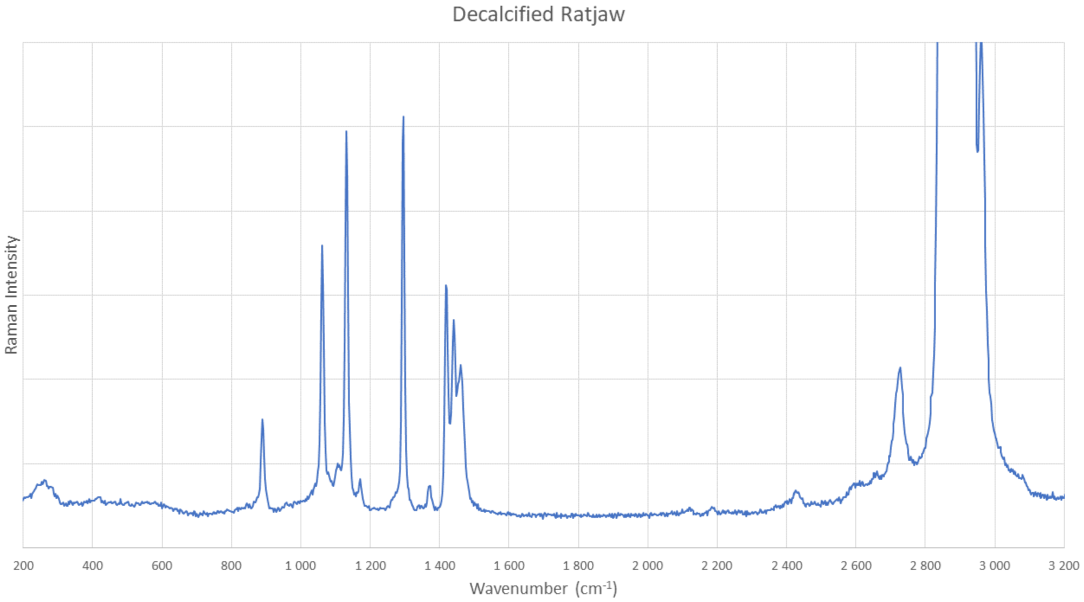

(a)

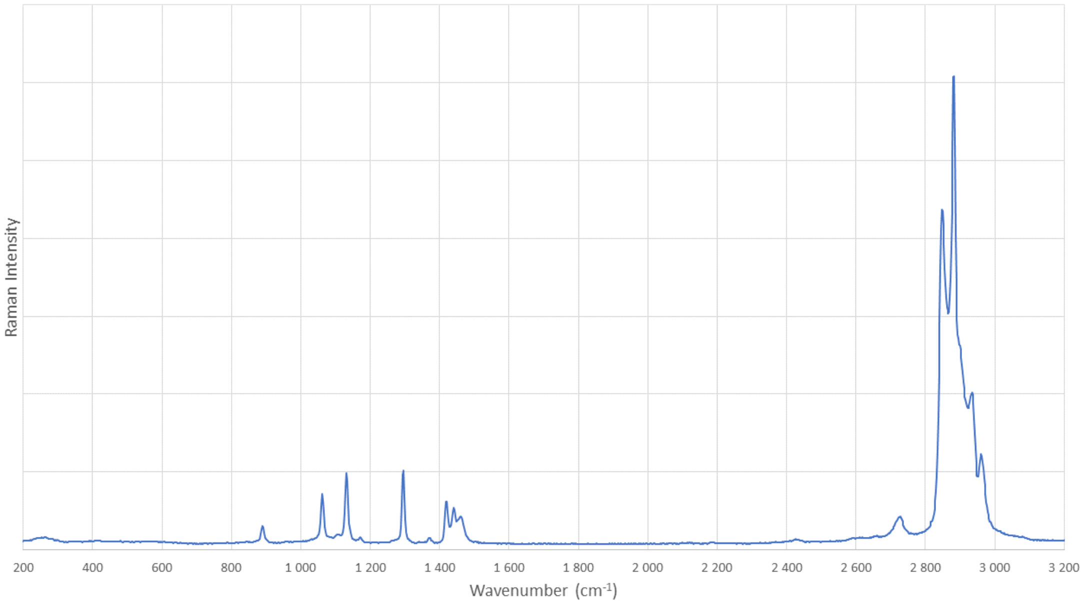

(b)

Figure 4.3.4: Raman spectrum of a decalcified rat jaw sections in paraffin. The scale for Raman intensity is based on the second highest peak in (a), and the highest peak in (b). Captured using a Raman microscope (Witec Alpha 300r) from an arteriole, 532 nm laser, 600 grooves/mm grating, 10 mW laser power, 6 accumulations, 10 s acquisition time.

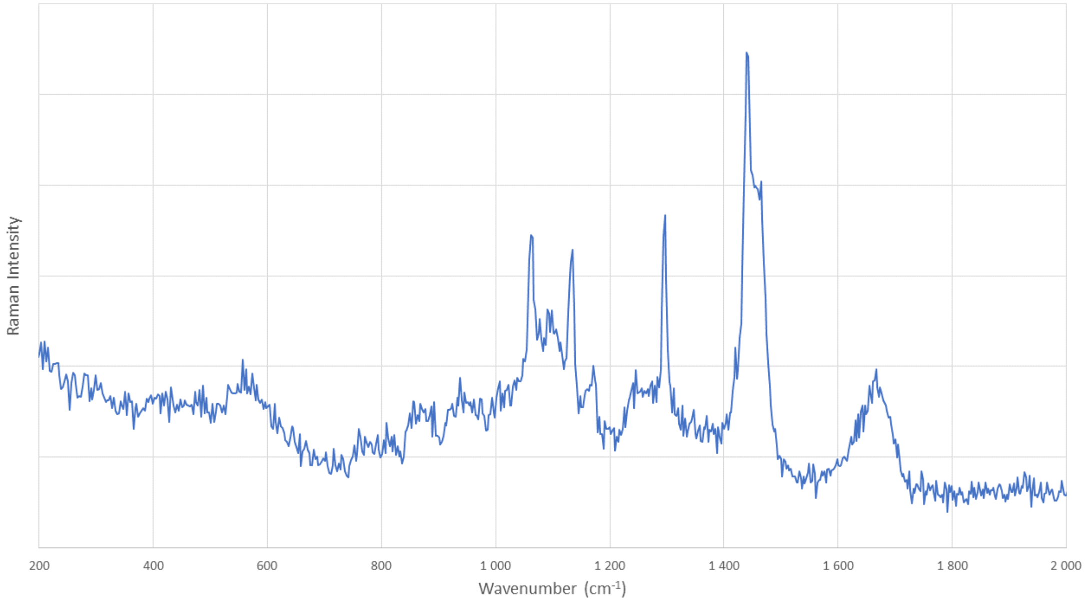

Figure 4.3.5: Raman spectrum from a decalcified rat jaw sections in paraffin. Captured using a Raman microscope (Witec Alpha 300r) from the tissue surrounding an arteriole, 532 nm laser, 600 grooves/mm grating, 10 mW laser power, 6 accumulations, 10 s acquisition time.]

bly the same as for the thicker dog jaw section, that is to say an increase in either non-resonant background signal or fluorescence because of the increased thickness of the sample and/or MMA layer the sample is embedded in. The fact that the increased base-line is less noticeable for the rabbit leg section might indicate that the sample is thinner than the thicker dog jaw section. A thinner sample would require thinner layer of embedding MMA, so this explanation work even if only the MMA layer is at fault for the increase in non-resonant background signal.

Raman spectra from two bone marrow biopsies of different thickness (one 10 µm, one somewhere between 7-20 µm), as well from a bone nodule, were collected. For the most part, these three samples gave very similar Raman spectra when looking at areas in the samples with lower bone density. Because of this, only the spectrum from the bone nodule is shown for these areas here, see Figure 4.3.7. Here, peaks can be found at 600 cm^{-1} (PO_4^{3-} ν_4 bending mode), 810 cm^{-1} (proline/hydroxyproline), 970 cm^{-1} (ν_1 mode, PO_4^{3-}), 1130 cm^{-1} (might correspond to either A-type carbonate or ν_3 mode for PO_4^{3-}), 1450 cm^{-1} (CH bending), 1730 cm^{-1} (amid I) and 2950 cm^{-1} (CH stretching).

The two bone biopsies however both gave some interesting results when looking at other areas in the sample. For the 10 µm biopsy, an overview image can be seen in Figure 4.3.8.

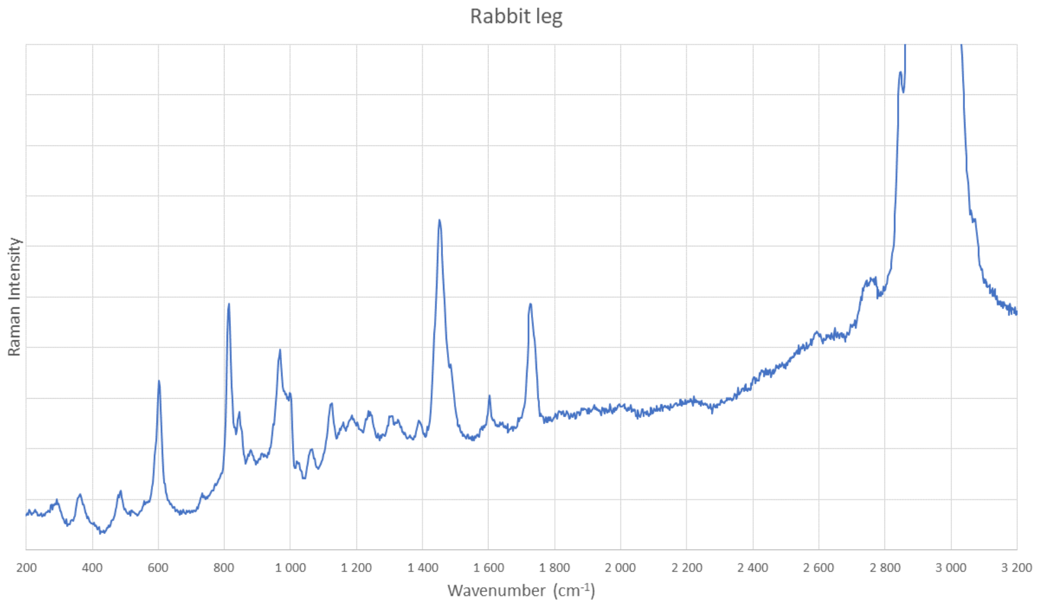

(a)

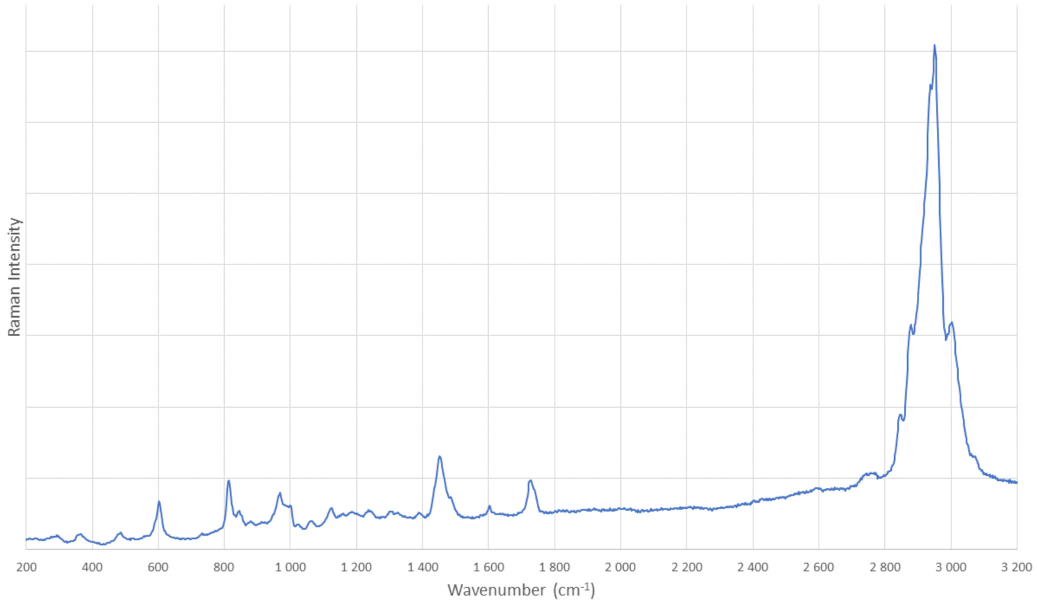

(b)

Figure 4.3.6: Raman spectrum of a rabbit leg bone sample embedded in MMA. The scale for Raman intensity is based on the second highest peak in (a), and the highest peak in (b). Captured using a Raman microscope (Witec Alpha 300r) from a single point, 532 nm laser, 600 grooves/mm grating, 10 mW laser power, 6 accumulations, 10 s acquisition time.

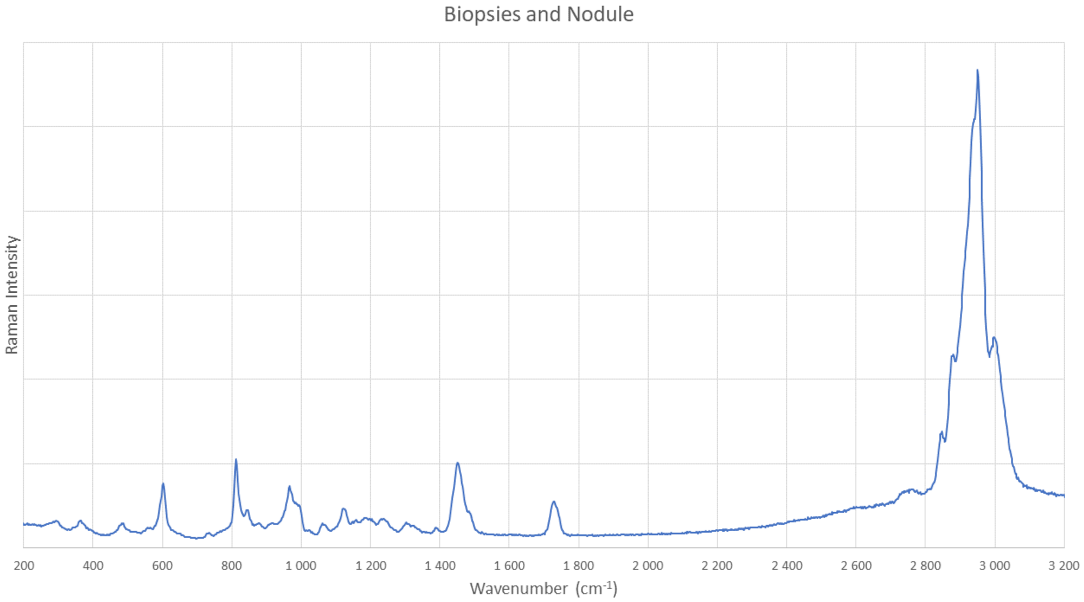

Figure 4.3.7: Raman spectrum from a bone nodule (arthritis 1). Captured using a Raman microscope (Witec Alpha 300r) from a single point, 532 nm laser, 600 grooves/mm grating, 10 mW laser power, 6 accumulations, 10 s acquisition time.

Figure 4.3.8: An overview image of the parts of a 10 µm bone marrow biopsy taken using an optical brightfield microscope. The image was made by merging multiple brightfield images.

Here the spectrum seen in Figure 4.3.7 fit the more white and red areas seen in Figure 4.3.8, which was the less dense bone tissue in the sample. The darker areas on the other hand, which had structure similar to compact bone, gave the Raman spectrum seen in Figure 4.3.9. While all the peaks are at the same wavenumbers, this spectrum has a much higher peak at around 960 cm^{-1} (the ν_1 mode for $PO_4{}^{3\text{-}}$). This then meant that this spectrum was closer to the typical Raman spectrum for bone (see Figure 2.10.1), where the Raman signal around 960 cm^{-1} is the highest. As the denser tissue contained more HAp, it made sense for the ν_1 mode for $PO_4{}^{3\text{-}}$ to give off a stronger signal. This also show that even though two different tissues might have a similar molecular composition, the structure of the tissues also affect the Raman signal the tissue can create.

For the 7-20 µm biopsy, an overview image of the sample can be seen in Figure 4.3.10. Here, the white areas fit the spectrum seen in Figure 4.3.7. The darker areas also fit the spectrum seen in Figure 4.3.9. The brown areas on the other hand were not suppose to be from bone, and was therefore also tested in order to confirm if this was true. It should be noted that these areas couldn't be scanned using a laser power of 10 mW, as this would burn through the sample. Instead, the laser was turned down to 0.1 mW power. A spectrum from these areas can be seen in Figure 4.3.11. While the spectrum doesn't give a lot of information as the molecular structure of this material, it is clearly different from the Raman spectrum of bone, or any of the earlier spectrum found from HAp. This confirms that this material is something else other then bone tissue.

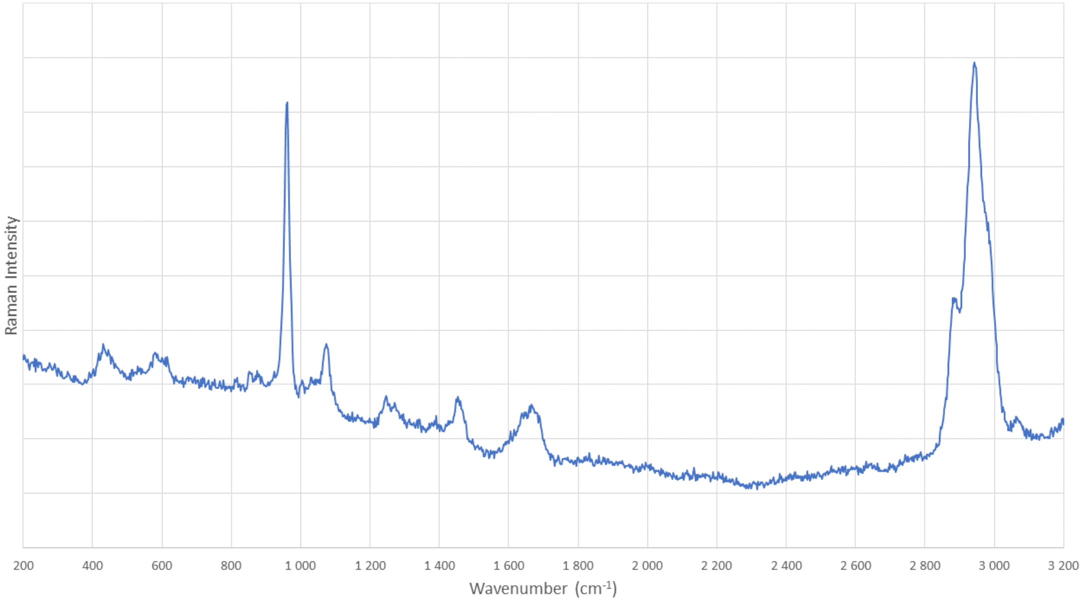

Figure 4.3.9: Raman spectrum from a 10 µm bone marrow biopsy. Captured using a Raman microscope (Witec Alpha 300r) from a single point, 532 nm laser, 600 grooves/mm grating, 10 mW laser power, 6 accumulations, 10 s acquisition time.

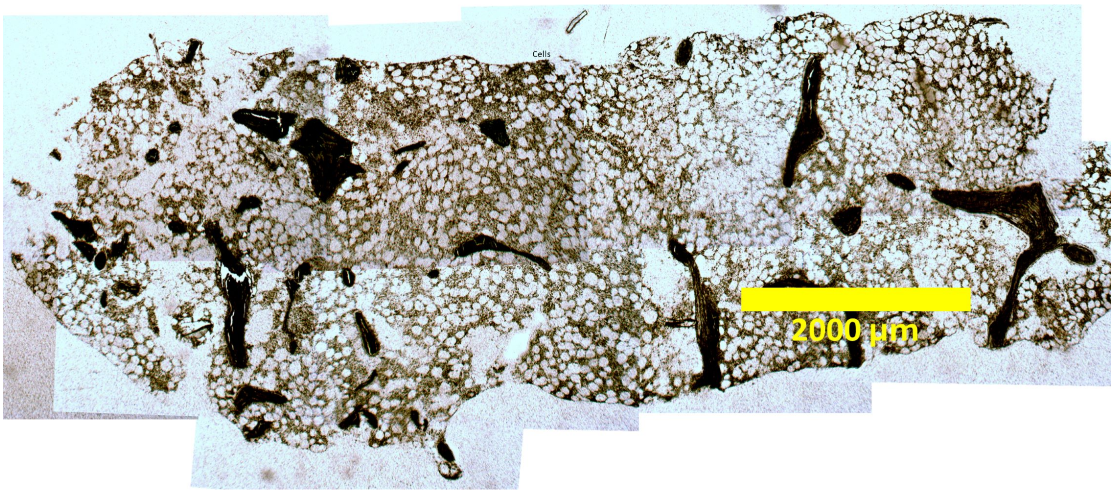

Figure 4.3.10: An overview image of a 7-20 µm bone marrow biopsy taken using an optical brightfield microscope. The image was made by merging multiple brightfield images.

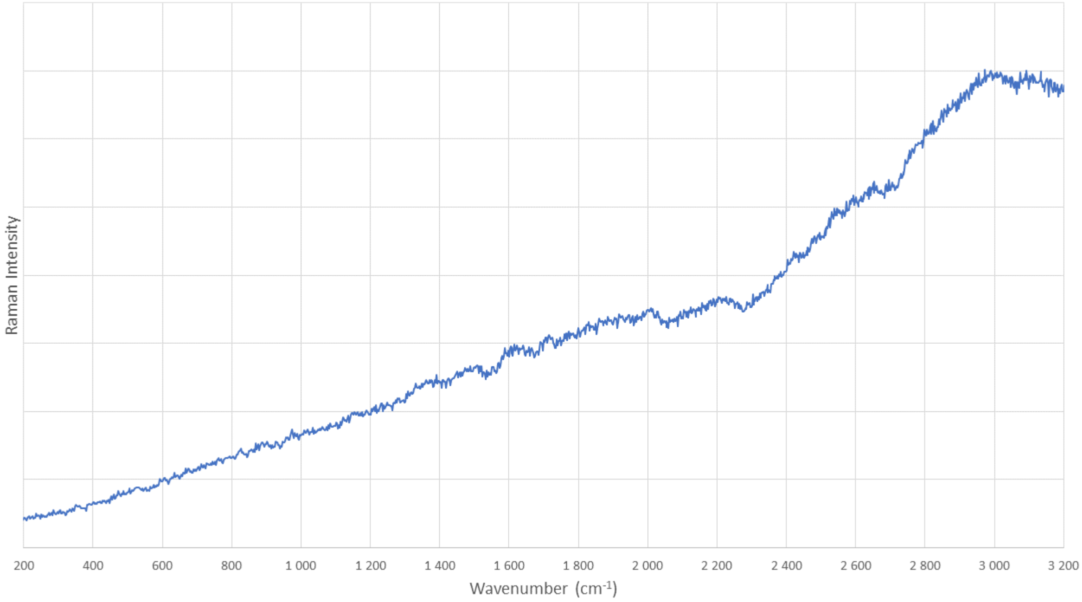

Figure 4.3.11: Raman spectrum from a 10 µm bone marrow biopsy. The spectrum is made from the brown tissue seen in Figure 4.3.10. Captured using a Raman microscope (Witec Alpha 300r) from a single point, 532 nm laser, 600 grooves/mm grating, 0.1 mW laser power, 6 accumulations, 10 s acquisition time.

Acquiring spectra from the MC3T3-E1 preosteoblasts samples (which had been cultured for 21/31 days) was interesting primarily because these samples weren't embedded in neither MMA nor paraffin, meaning the Raman spectra obtained would only come from the HAp mineralized extracellular matrix in the sample, and not from the embedding material. As the mineralized matrix also had a different structure from that of normal bone tissue, it would also be interesting to see if this affected the Raman spectra collected from the samples in any way. Lastly, one was also interested in seeing if the ARS staining would affect the Raman spectrum collected.

The spectrum from the preosteoblasts sample which had not been stained can be seen in Figure 4.3.12. Here, one see less background signal and more discernible peaks when the spectra were made from areas with a thicker layer of HAp. The peaks were found at 956 cm^{-1} (ν_1 mode, $PO_4{}^{3-}$), 1250 cm^{-1} (amid III), 1450 cm^{-1} (CH bending), 1670 cm^{-1} (amid I), and 2940 cm^{-1} (CH stretching). No peak was found between 820-890 cm^{-1}.

When trying to study the preosteoblasts sample which had been stained using ARS however, the laser ended up burning through the sample. Therefore, no Raman spectrum has been captured for this sample. This meant that, since the settings were the same when scanning both preosteoblasts samples, that the stained sample somehow was more sensitive to the laser. When looking at the absorption spectra for ARS, it seems like the molecule does absorb wavelengths at 532 nm. As the salt created between ARS and calcium takes on a similar reddish colour as the ARS, this salt would have the ability to absorb similar wavelengths to the ARS, unlike the HAp mineralized matrix alone, which because of its white colour would reflect more of the wavelengths. This would mean that the stained preosteoblast sample would absorb more energy from the laser than the non-stained sample, which might explain why the laser ended up only burning through the stained sample.

Last, one Raman spectrum was made from one of the tooth sections (Figure 4.3.13). This showed peaks primarily at 960 cm^{-1} (ν_1 mode, $PO_4{}^{3-}$) and 2945 cm^{-1} (CH stretching), though small peaks at around 430 (ν_2 mode, $PO_4{}^{3-}$), 590 (ν_4 mode, $PO_4{}^{3-}$) and 1080 cm^{-1} (A-type carbonate and/or ν_3 mode for $PO_4{}^{3-}$) could be observed as well. No peak was observed between 820-890 cm^{-1}. It should be noted that this was the only sample who's Raman spectrum had a 960 cm^{-1} peak higher than the 2945 cm^{-1} peak. This isn't to surprising, as the tooth section were much thicker than the other samples, which would increase the amount of calcium phosphate mineral that gave a Raman signal. The fact that the tooth section wasn't embedded in either MMA or paraffin might also have played a factor here.

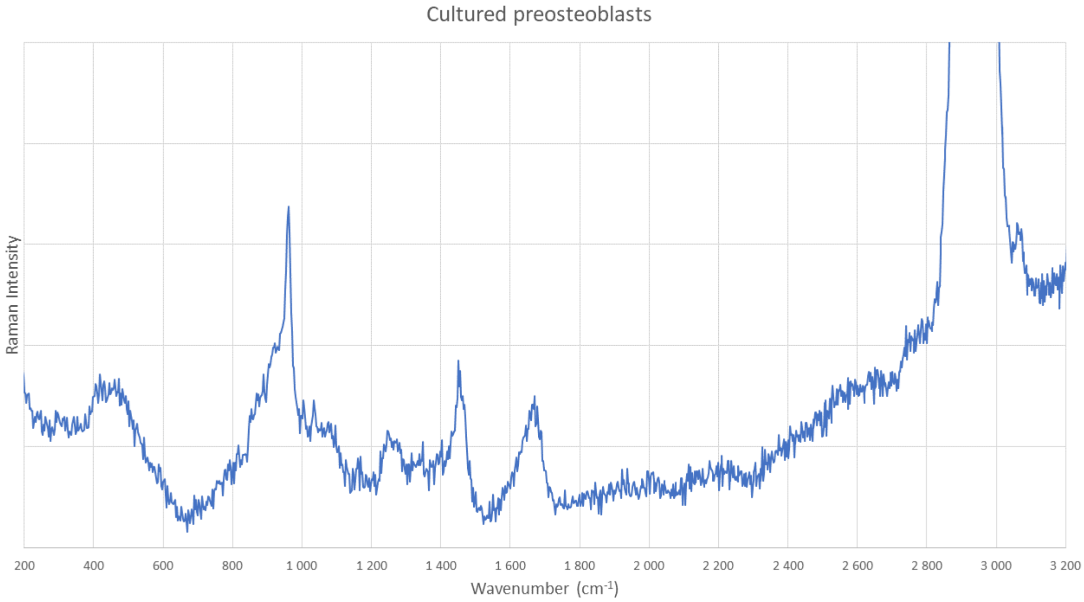

(a)

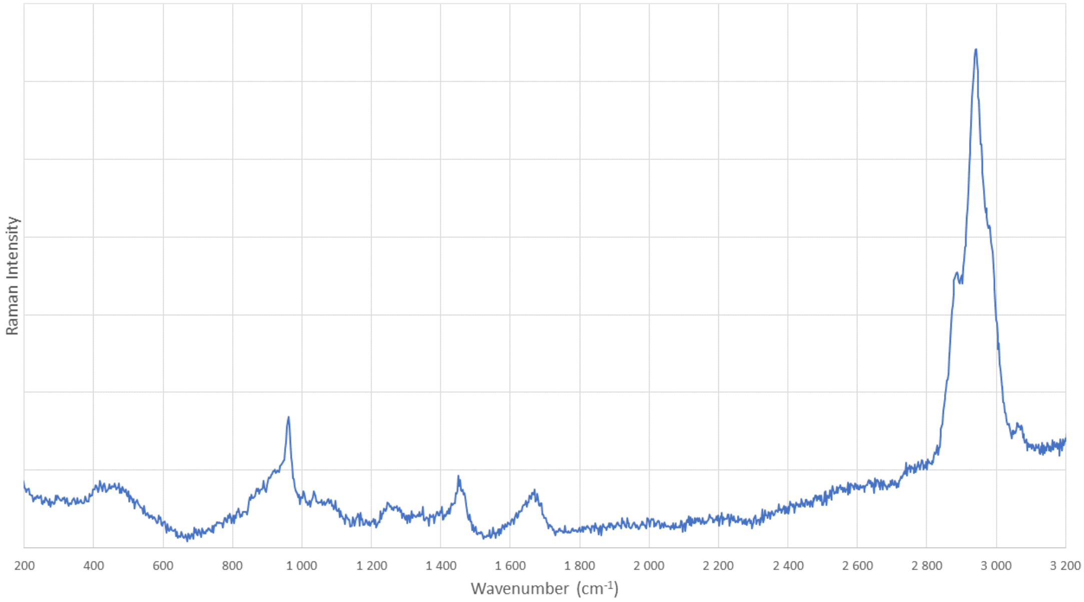

(b)

Figure 4.3.12: Raman spectrum of a MC3T3-E1 preosteoblasts sample which had been cultured for 31 days. The scale for Raman intensity is based on the second highest peak in (a), and the highest peak in (b). Captured using a Raman microscope (Witec Alpha 300r) from a single point, 532 nm laser, 600 grooves/mm grating, 10 mW laser power, 6 accumulations, 10 s acquisition time.

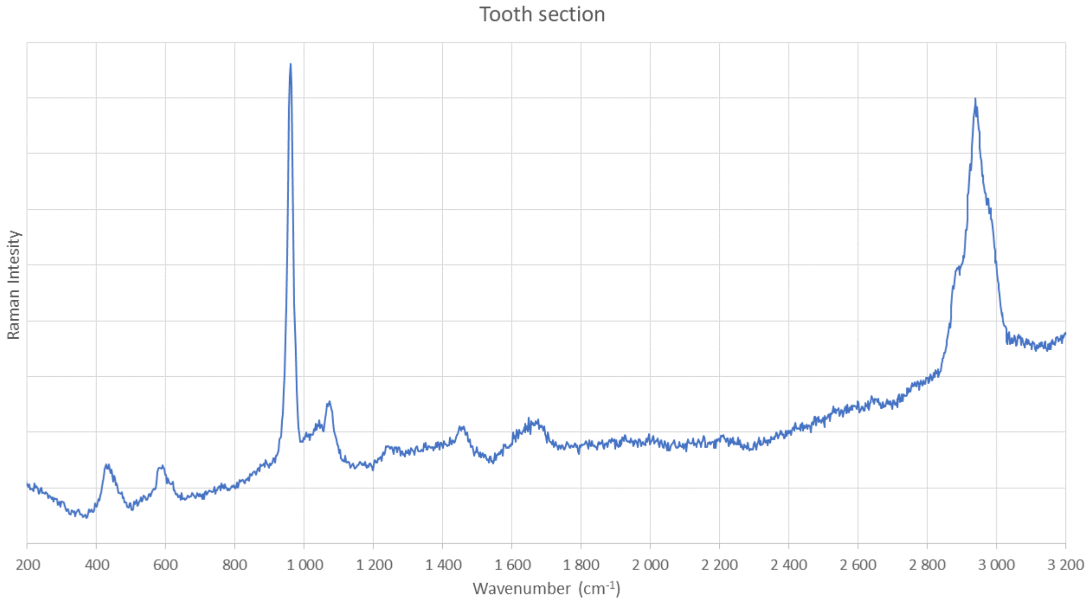

Figure 4.3.13: Raman spectrum of a tooth section. Captured using a Raman microscope (Witec Alpha 300r) from a single point, 532 nm laser, 600 grooves/mm grating, 10 mW laser power, 6 accumulations, 10 s acquisition time.

4.4 CARS

4.4.1 Trans and epi signal

The CARS microscope was set up in such a way that the collection of signal from both trans and epi direction should be possible (see Figure 2.12.1 for a simplified schematic, and section 2.12 for a more in depth description). At wavenumbers where the sample scanned has Raman active vibrations, the trans signal will usually be strong enough to be used for imaging, though this is only applicable to thin samples. On the other hand, if the signal in trans direction is to weak (gets overshadowed by non-resonant background signal), or the sample is to thick, then it might be more fruitful to instead look at the signal that is instead backscattered, that is to say the CARS signal in the epi direction. An epi signal can be created even if there is a strong trans signal (and vise versa), and the CARS microscope was setup in such a way that both could be detected at the same time. During most of the master's however, no epi signal was detected during any of the experiments. If this was because the samples didn't produce any epi signal, or if it was because of the faulty installation of the dichroic epi cube filters (see section 3.4 for further explanation), is unknown. Because of this, unless otherwise specified, all signal received during the following experiments was trans signal.

4.4.2 Dog jaw sections embedded in MMA

The two dog jaw sections of different thickness were the first to be studied using the CARS technique. The goal of studying these samples was to see if it was possible to images bone tissue using CARS, and, if this was possible, see how

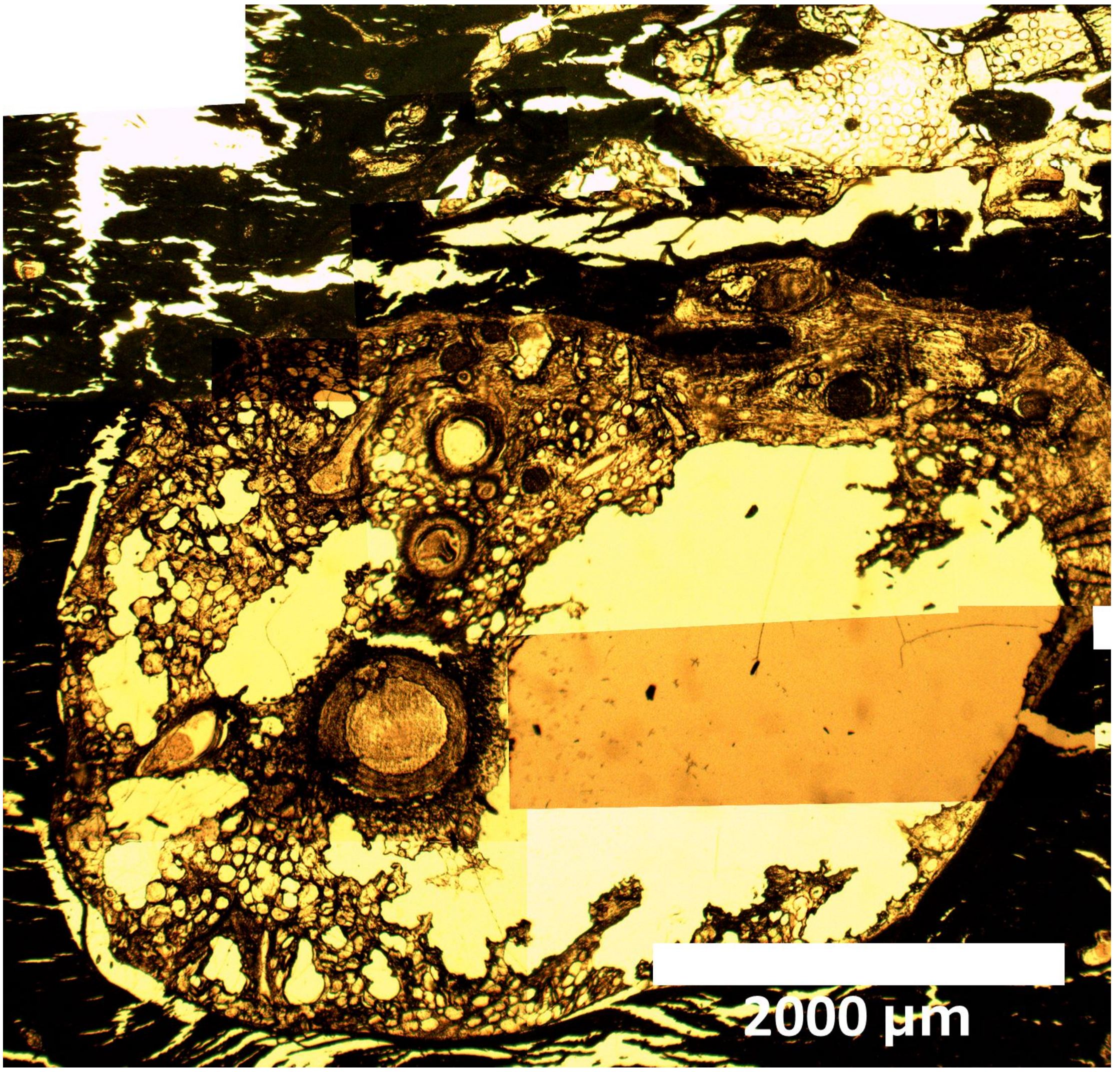

Figure 4.4.1: An overview image of the parts of a dog jaw 7 µm section taken using an optical brightfield microscope. The image was made by merging multiple brightfield images.

a thicker sample and/or a thicker layer of embedding material might affect the CARS process.

To be able to identify morphological features on the CARS images, a brightfield overview image was collected of the 7 µm section with an optical microscope (see Figure 4.4.1). Some of the most important structures seen in this image are described further in Figure 4.4.2. These include arterioles, venules, nerve bundles, blood vessels, the different types of bone tissue (spongy, trabecular and cortical), and bone structures that are produced inside bone marrow (known as bone inside bone marrow). One would expect to find calcium phosphate in the spongy, trabecular or cortical bone tissue, as these tissues consists of HAp, and not from the arterioles, venules, nerve bundles or blood vessels.

Images were also acquired using the brightfield camera on the CARS microscope. These images were from different areas seen in Figure 4.4.1. The same areas were then scanned using the CARS at wavenumber 988 cm^{-1} (λ_{pump} = 935.7 nm) and 2500 fs delay. Some of the images acquired can be seen in Figure 4.4.3. This

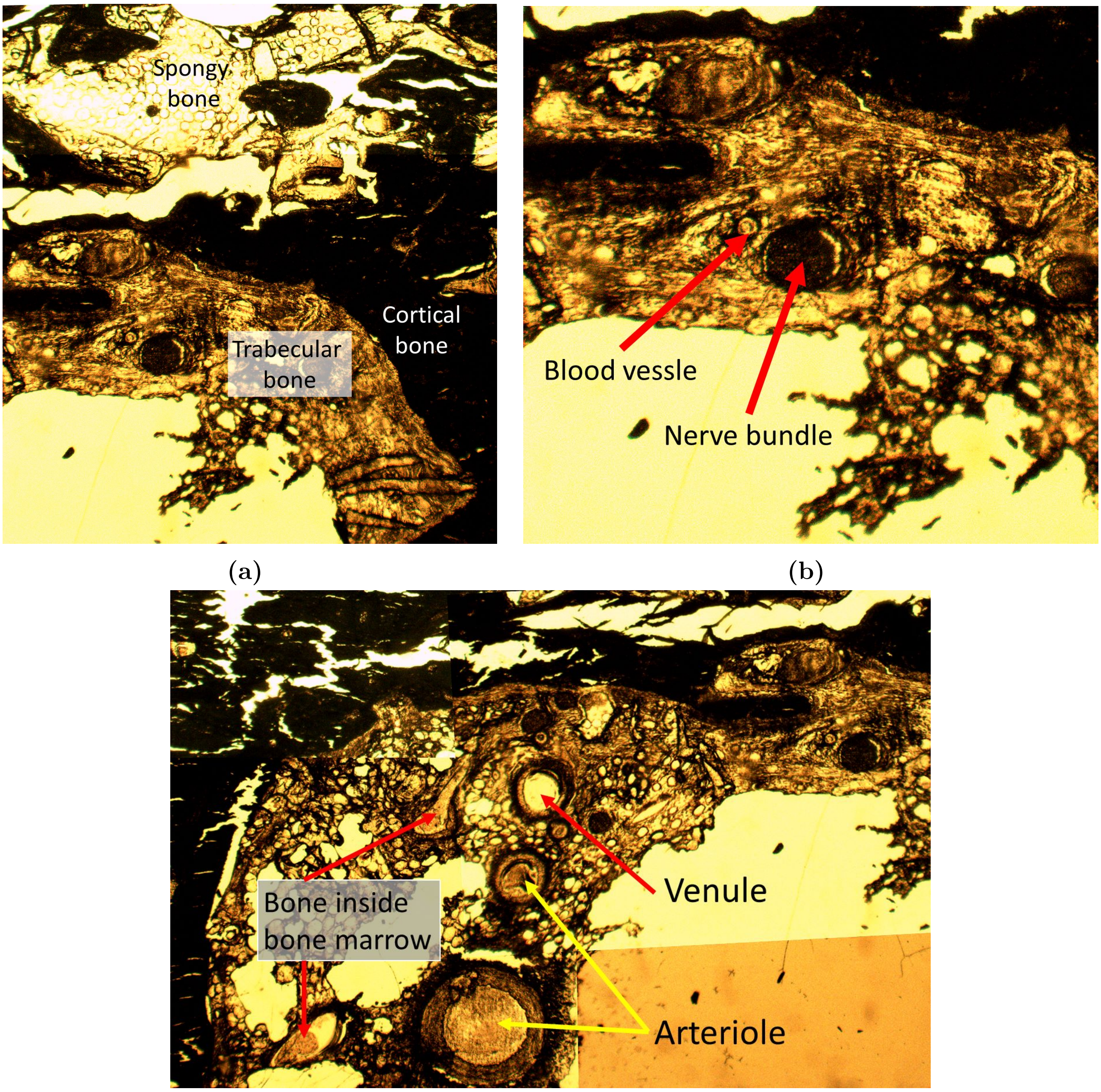

(a) **(b)**

(c)

Figure 4.4.2: Brightfield image of a bone sample showing the difference between spongy bone, cortical bone (a type of compact bone) and trabecular bone (a type of spongy bone) **(a)**; brightfield image of a bone sample showing a nerve bundle and a blood vessel **(b)**; brightfield image of a bone sample showing arterioles, a venule, and bone that develops inside bone marrow **(c).**

shows that the CARS signal acquired can be used for imaging of the bone, creating images with contrast resembling those captured using a brightfiled camera. The CARS signal acquired at this wavenumber should in theory come from ν_1 PO_4^{3-} stretching.

Tests were then done in order to confirm the wavenumber and delay where the HAp gave the strongest CARS signal. For delay, multiple images were acquired at different values of delay between 0 and 5500 fs, with a step of 250 fs (wavenumber

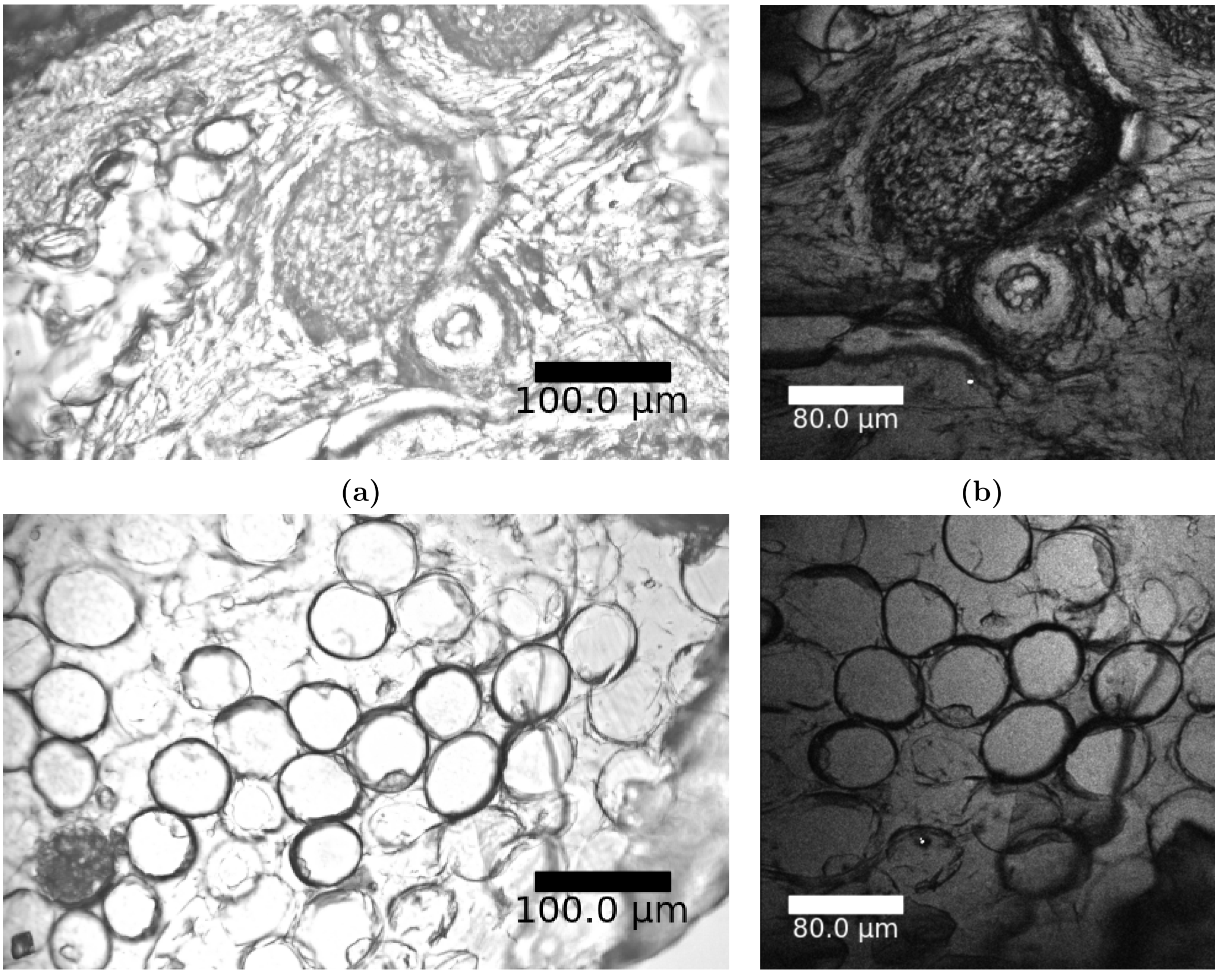

(a) **(b)**

(c) **(d)**

Figure 4.4.3: Brightfield images **(a, c)** and corresponding CARS images **(b, d)** of different areas of a 7 µm dog jaw section. (a) and (b) depicts a nerve bundle and a blood vessel, while (c) and (d) depicts spongy bone. The CARS images were captured at 988 cm^{-1}. λ_{pump} = 935.7 nm, λ_{Stokes} = 1031 nm, delay = 2750 fs. In CARS imaging, black represents the lack of signal, while grey/white represents signal at different strengths (the brighter the stronger).

988 cm^{-1}). Then, the strength of the signal from each image were plotted, which can be seen in Figure 4.4.4. Based on these results, the bone samples gave the strongest HAp signal at 2750 fs delay.

For the wavenumber, multiple images were acquired at different values of λ_{pump} from 927.4 nm to 944.8 nm. The corresponding wavenumber (see Equation 2.15) was then plotted against the signal strength of each image. The results of this can be seen in Figure 4.4.5. Here, one can see a peak at around 988 cm^{-1}, which was as expected based on the results acquired from the DCPD crystals. This is also the reason 988 cm^{-1} was used as a the primary wavenumber for study of all samples when looking at the ν_1 PO_4^{3-} mode later in this thesis. However, one can also see that at higher wavenumbers, the signal strength increases to higher values than that of the 988 cm^{-1} peak, which was unexpected. In order to confirm if this high point corresponded to another Raman peak other than the ν_1 PO_4^{3-} mode, and if so which one, a new wavenumber spectrum was made from 886.1-1292.1

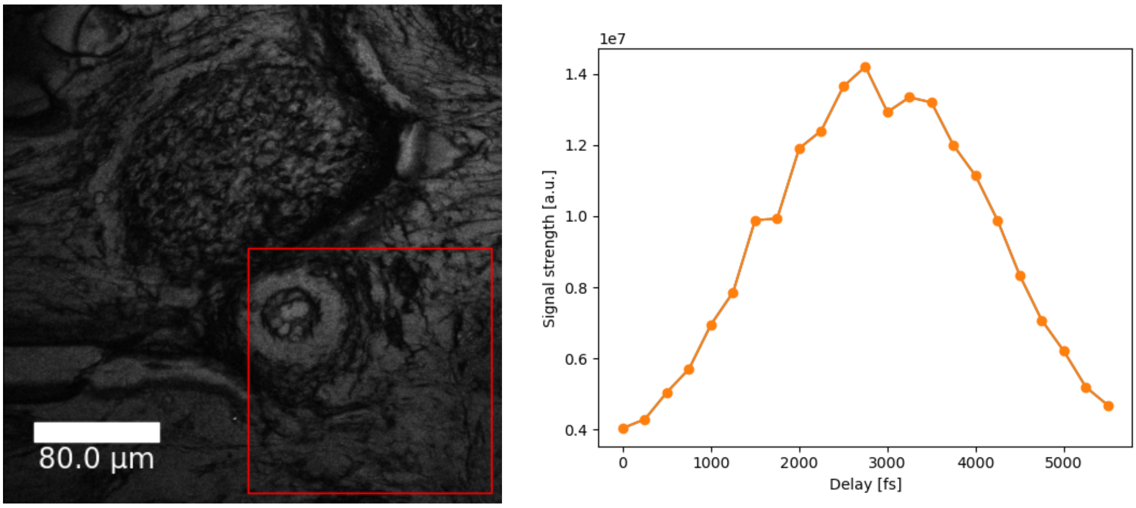

(a) (b)

Figure 4.4.4: **(a)**: CARS imaging of a 7 µm dog jaw section at 2750 fs delay (wavenumber 988 cm^{-1}, λ_{pump} = 935.7 nm, λ_{Stokes} = 1031). **(b)**: A spectrum comparing the signal strength at various values of delay from the area marked in **(a)** using all the different images seen in Figure A.0.2

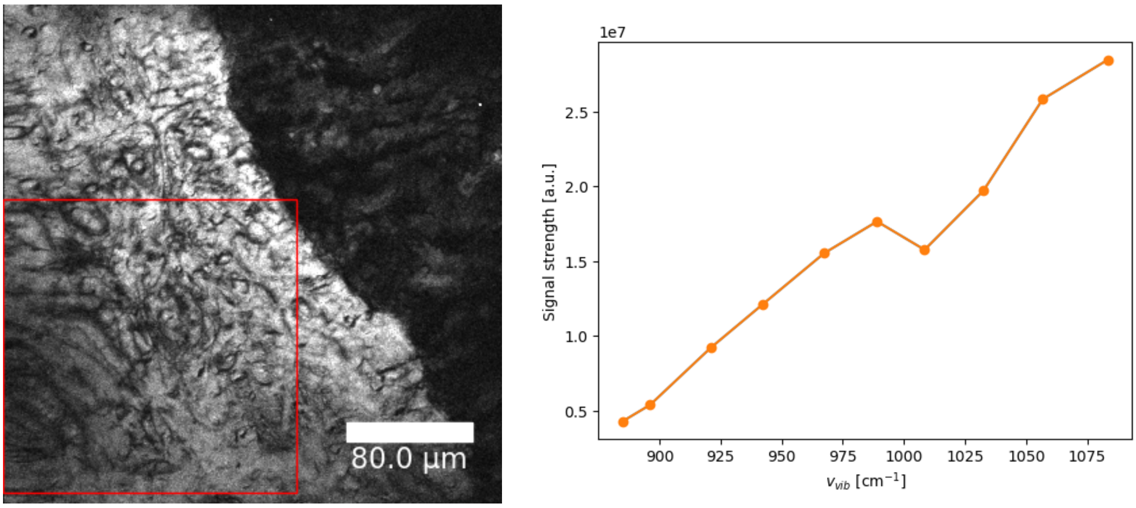

(a) (b)

Figure 4.4.5: **(a)**: CARS imaging of a dog jaw sample at wavenumber 988 cm^{-1} (λ_{pump} = 935.7 nm, λ_{Stokes} = 1031, 2750 fs delay). **(b)**: A spectrum comparing the signal strength at various values of wavenumber from the area marked in **(a)** using all the different images seen in Figure A.0.1

cm^{-1} (λ_{pump} from 909.8 nm to 944.8 nm) using both the 857 ± 15 nm and 832 ± 18 nm filter cubes. This was done after the re-alignment of the lasers. This spectra can be seen in Figure 4.4.6. A very interesting result that can be observed from this spectra is that the ν_1 PO_4^{3-} mode no longer is at 988 cm^{-1}, but instead finds itself at 963.9 cm^{-1}. While this fits more with the literary value for this mode, it is strange that the signal peak has changed its placement. Another peak is also seen, here at 1125.5 cm^{-1}, which might correspond to A-type carbonate. The signal strength is however still increasing with higher wavenumber. It should also

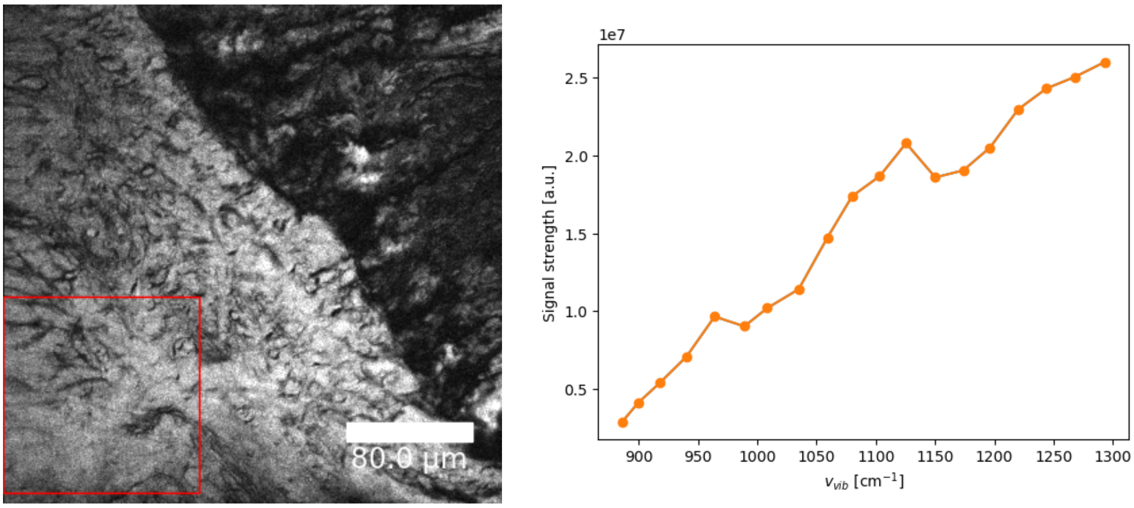

(a) (b)

Figure 4.4.6: **(a)**: CARS imaging of a dog jaw sample at wavenumber 963.9 cm^{-1} (λ_{pump} = 937.8 nm, λ_{Stokes} = 1031, 2750 fs delay). **(b)**: A spectrum comparing the signal strength at various values of wavenumber from the area marked in **(a)** using all the different images seen in Figure A.0.3

be noted that the increase in signal strength seen in Figure 4.4.5b and 4.4.6b is near linear if one ignores the peaks.

As a big part of bone consists of either collagen or structures containing CH-bonds, there would in theory be a possibility of obtaining a CARS signal from CH stretching from the sample. If the correct area were to be scanned, this signal could be stronger than the HAp signal. In order to check if this actually was the case, images were captured of a blood vessel and a nerve bundle with surrounding bone tissue using both wavenumber 988 cm^{-1} and 2845 cm^{-1}, as these were structures where one would expect to find CH-bonds. The results of this can be seen in Figure 4.4.7. The background signals was then removed from the two datasets acquired (as discussed in section 3.4), and they were overlaid on-top of each other. The end result of this can be seen in Figure 4.4.8. Here, one can clearly see that that the area that gives the strongest signal at 2845 cm^{-1} (therefore more CH-bonds) is the nerve bundle, with some signal also coming from the blood vessel, while the area around this bundle, which primarily consist of HAp, gives the strongest signal at 988 cm^{-1} (therefore more calcium phosphate/HAp). These results fit with what one would expect based on the composition of the two tissues. It should however be noted that a weak signal at 988 cm^{-1} still was collected from the blood vessel and nerve bundle, while a weak signal at 2845 cm^{-1} also was collected from the surrounding HAp tissue. As there exists collagen in the calcified matrix, a weak CH-signal from this tissue wasn't unexpected. The 988 cm^{-1} from the nerve bundle and blood vessel was more unexpected, but it has been shown that both blood vessels and nerves both give a weak Raman signal at around 1000 cm^{-1}, so this signal might be from that. Further tests into CH-bonds in bone tissue can be seen in subsection 4.4.3.

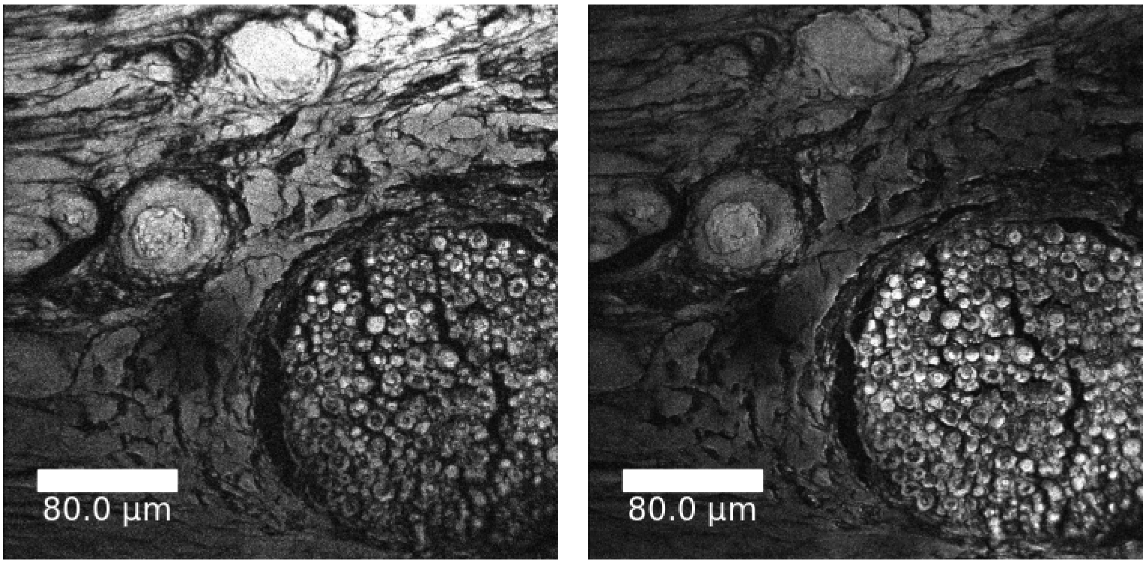

(a) **(b)**

Figure 4.4.7: CARS imaging of a 7 µm dog jaw bone sections done through calcium phosphate signal (wavenumber 988 cm^{-1}, $\lambda_{pump} = 935.7$ nm, 2750 fs delay) (a) and CH-signal (wavenumber 2845 cm^{-1}, $\lambda_{pump} = 979.2$ nm, 0 fs delay) (b). $\lambda_{Stokes} = 1031$ nm.

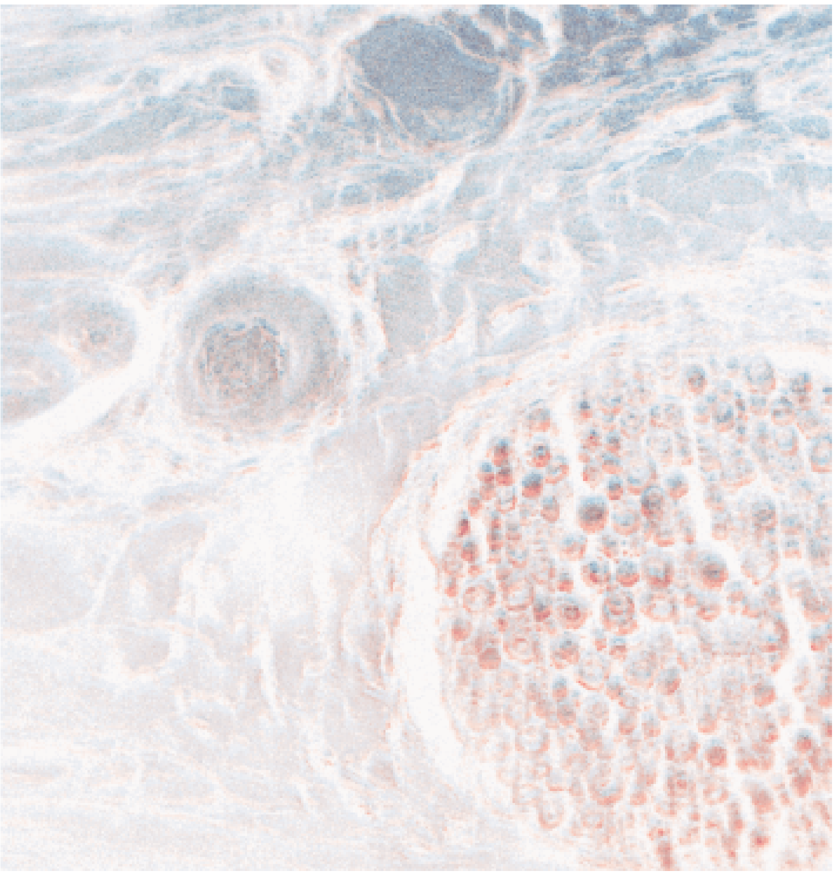

Figure 4.4.8: Comparing the signal strength from calcium phosphate and CH given in Figure 4.4.7. Blue represent calcium phosphate, while red represents CH.

An interesting detail emerged from the imaging of the area seen in Figure 4.4.5a. This area depicts an interface between trabecular bone and cortical in the sample. As cortical bone is more dense than trabecular bone (compact vs spongy), one would expect the cortical bone to give a stronger Raman signal of the two tissues, but that is not the case here. A reason for this might be that the cortical bone is so dense that the lasers weren't able to penetrate as deep into the sample as they could with trabecular bone. It should be noted that a signal did come from the cortical bone, even though it was weaker than the signal from the trabecular bone. This signal was at its strongest at around 967.5 cm^{-1}. At this wavenumber, the structures of this bone were also easier to see, see Figure 4.4.9. In theory, the cortical bone might have given a better epi signal than the trabecular bone, but because of the less than ideal epi-setup, it was difficult to say if the lack of epi signal recorded was because of the sample, or the CARS microscope.

As a typical Raman spectrum for bone shows that the strongest Raman signal usually could be found around 960 cm^{-1}, a delay spectrum was made using this wavenumber (see Figure 4.4.10). Here, the optimal delay was found to be at 2250 fs delay, which was different from the optimal delay for a 988 cm^{-1} signal. When comparing two images captured of the same area (trabecular bone tissue) using either 960 or 988 cm^{-1}, one can see that the 988 cm^{-1} signal was the strongest (see Figure 4.4.11). This was later confirmed by looking at the numerical data used to create the images. While the CARS signal captured was weaker at 960 cm^{-1} than at 988 cm^{-1}, this does show that even though the difference in wavenumber isn't large, and the signal was from the same vibrational mode, there still was a change in optimal delay.

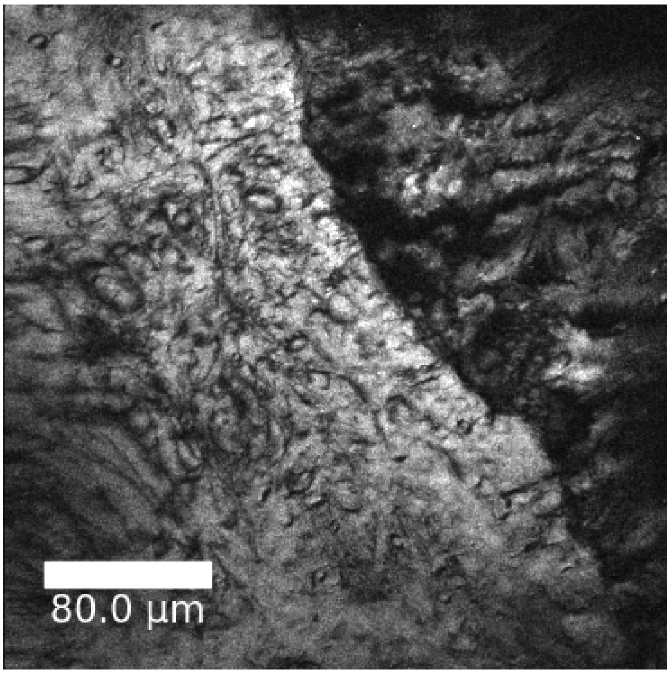

Figure 4.4.9: The interface between trabecular and cortical bone, depicted using CARS at wavenumber 967.5 cm^{-1} ($\lambda_{pump} = 937.5$ nm, $\lambda_{Stokes} = 1031$ nm, 2750 fs delay).

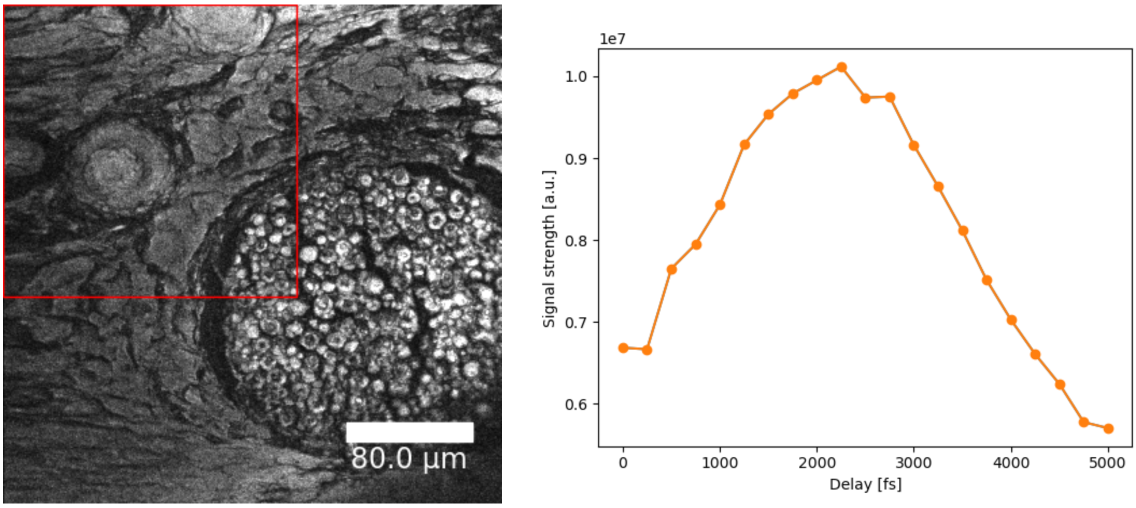

(a) **(b)**

Figure 4.4.10: **(a)**: CARS imaging of a dog jaw section at 2250 fs delay (wavenumber 960 cm^{-1}, $\lambda_{pump} = 938.2$ nm, $\lambda_{Stokes} = 1031$ nm, delay = 2250 fs.). **(b)**: A spectrum comparing the signal strength at various values of wavenumber from the area marked in **(a)** using all the different images seen in Figure A.0.4.

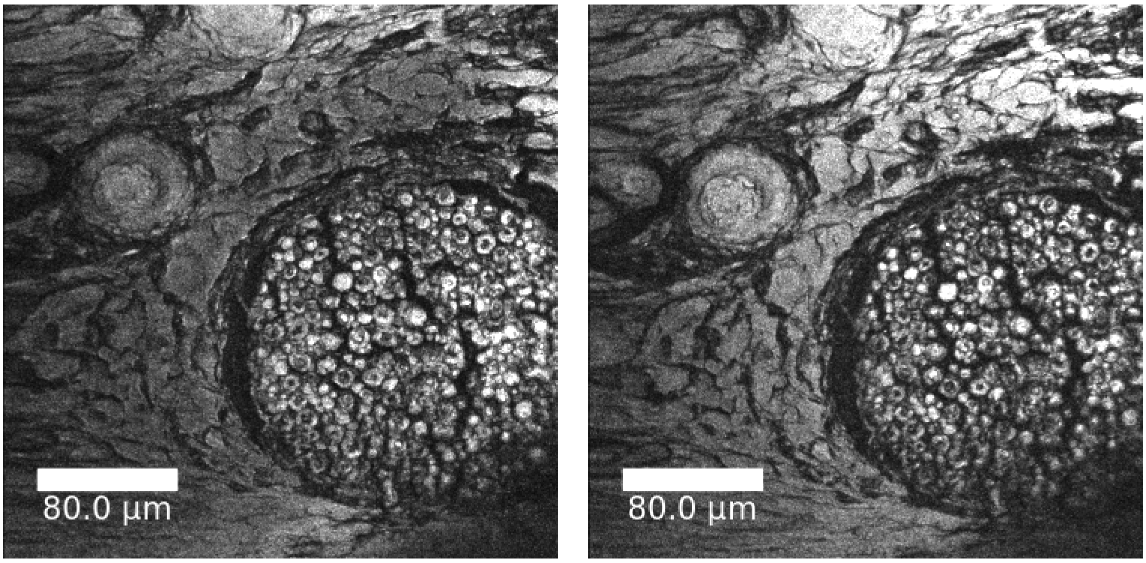

(a) **(b)**

Figure 4.4.11: CARS images acquired of a 7 µm dog jaw section at 960 cm^{-1} ($\lambda_{pump} = 938.2$ nm, $\lambda_{Stokes} = 1031$ nm, 2250 fs delay) **(a)** and 988 cm^{-1} ($\lambda_{pump} = 935.7$ nm, $\lambda_{Stokes} = 1031$ nm, 2750 fs delay) **(b)**.

Though brightfield imaging was attempted of the thicker dog jaw section, no good brightfield images were collected using the optical microscope. This was most likely due to the sample's thickness, as brightfiled imaging is dependent on light passing through the sample. The brightfield camera attached to the CARS was however able to image the sample (see Figure 4.4.12), which may be because the light source for this microscope was a LED light focused on a smaller section of the sample. CARS imaging was then done of the sample. Thought the technique was able to depict structures on the sample's surface (see Figure 4.4.12), the images acquired seemed to be of lower quality than those obtained from the 7 µm section. Looking at the signal strength coming from the sample at different wavenumbers, the spectrum obtained was also different than that from the 7 µm section (see Figure 4.4.13). No clear peak can be seen around 960-990 cm^{-1}, as one would expect based on the typical Raman spectrum for bone. What seems to be a peak can however be seen around 1057 cm^{-1}, which likely corresponded to either ν_3 asymmetric stretching mode of $PO_4{}^{3-}$, or the ν_1 mode of B-type carbonate.

The lack of clear peak around 960-990 cm^{-1}, as well as the lower quality of images acquired, points to either a weaker CARS signal from the sample, or more background signal interfering with the CARS signal. As the biggest differences between this section and the 7 µm one are the thickness of the sample, as well as the thickness of the MMA layer the sections are embedded in (much larger in this sample), one or both of these factors might be in play here. Both a thicker sample and a thicker layer of MMA might have lead to a weaker CARS signal for a multitude of reasons, like by reducing the lasers ability to penetrate deep enough into the sample so that a strong trans signal could be transmitted on the other side, or by absorption of signal by surrounding molecules. The thick MMA layer might also have lead to the creation of more background signal, as MMA also has a Raman peak in the 930-990 cm^{-1} range, as well as in the 1030-1100 cm^{-1}. When the layer of MMA is very thin, the CARS signal created from this layer would be very little when compared to the sample, but when its much thicker, the signal strength would increase, which then would mix with the CARS signal from the sample, muddying the quality of data acquired. This might also explain why there were no clear peak around 960-990 cm^{-1} in the spectra shown in Figure 4.4.13, as here the CARS signal from MMA might have obscured it. Still, imaging of the thicker dog jaw section was possible, and, as already shown by the 7 µm section, there is a possibility that by preparing the sample a little bit differently, the quality of CARS images acquired could increase drastically.

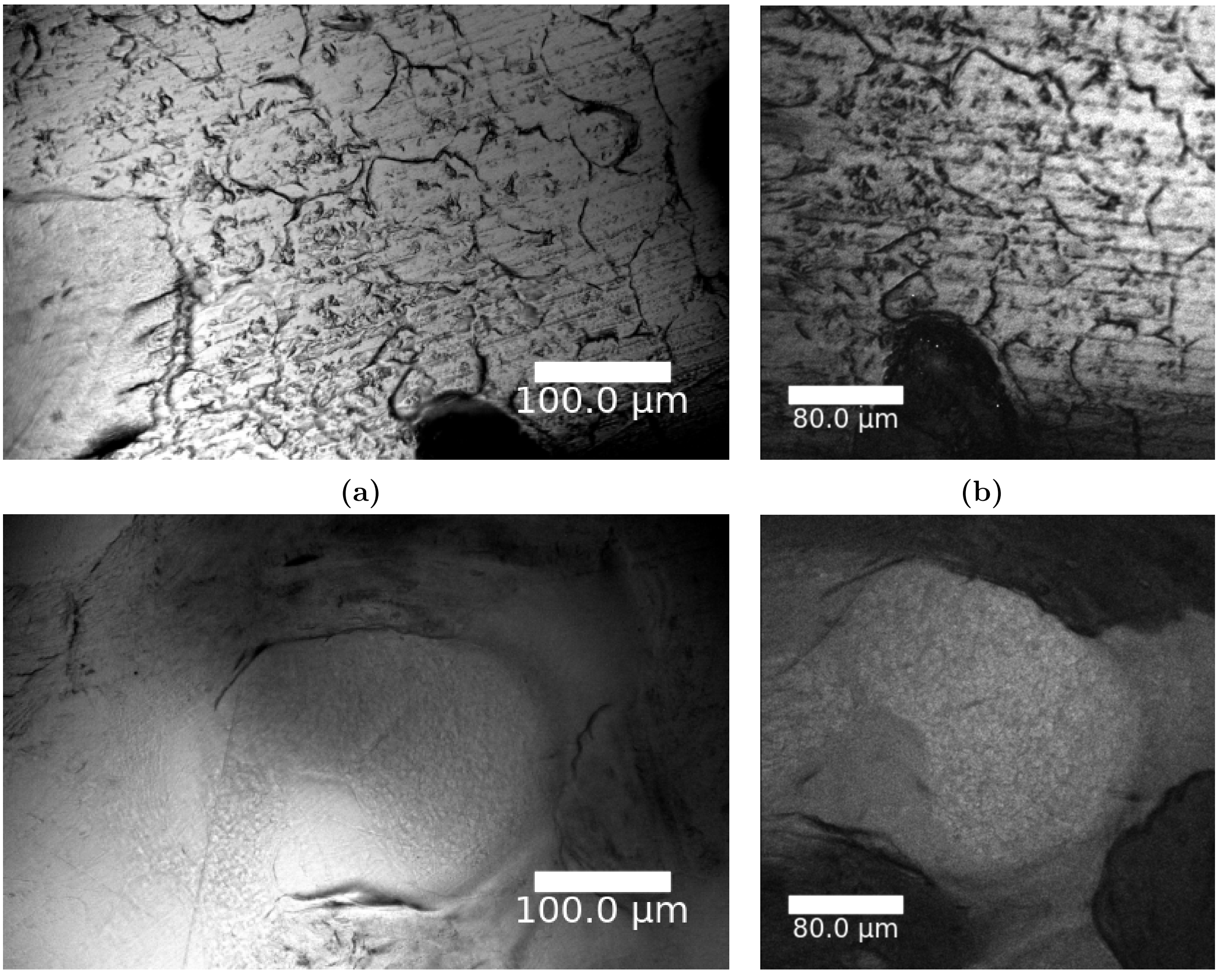

(a) **(b)**

(c) **(d)**

Figure 4.4.12: Brightfield images **(a,c)** and corresponding CARS images **(b,d)** of different areas of a dog jaw section. The CARS images were captured at 988 cm^{-1} ($\lambda_{pump} = 935.7$ nm, $\lambda_{Stokes} = 1031$ nm) and 2750 fs delay.

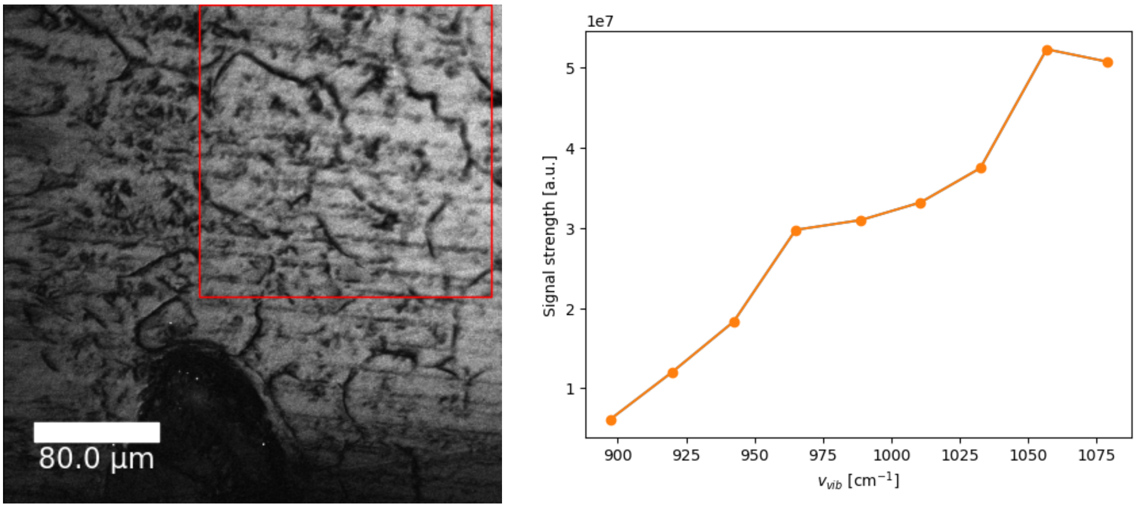

(a)

(b)

Figure 4.4.13: **(a)**: CARS imaging of a dog jaw section at 1057 cm^{-1} (λ_{pump} = 929.7 nm, λ_{Stokes} = 1031 nm) and 2750 fs delay. **(b)**: A spectrum comparing the signal strength at various values of wavenumber from the area marked in **(a)** using all the different images seen in Figure A.0.5.

4.4.3 Decalcified rat jaw

The goal of studying the 5 µm decalcified rat jaw section using CARS was primarily to study the organic component of bone tissue. The reason for this was that the amount of HAp when compared to the rest of the tissue in this sample should be far less than in the other samples thanks to the decalcification (removal of calcified minerals, here HAp), making it much easier to study the organic component. It should be noted that the decalcification didn't remove all HAp in the rat jaw section, so one should still be able to detect traces of it if one were to look.

Before CARS imaging was done on the sample, a overview image was made using a optical brightfield microscope (see Figure 4.4.14). Some of the most important structures seen in this images is described in Figure 4.4.15.

As the rat jaw sample was decalcified, it was primarily studied by focusing on the CH-bindings in bone. As these in theory should be able to produce CH stretching signal somewhere in the interval 2800-3100 cm^{-1}, it was first decided to study which wavenumber in this interval would give the strongest signal. Multiple images were acquired at different values of λ_{pump} from 780.3 nm to 803.2 nm (2750-3116 cm^{-1}), and the corresponding wavenumber was then plotted against the signal strength (see Figure 4.4.16a). Here, there is a clear peak at 2844.6 cm^{-1}.

After finding the best wavelength, the best value for delay was also looked into. Multiple images were acquired at different values of delay between 0 and 10000 fs, with a jump of 250 fs between each image (wavenumber 2844.6 cm^{-1}). Then, the strength of the signal from each image were plotted, which can be seen in Figure 4.4.16b. While a strong signal was recorded at all values of delay, the signal was clearly strongest at around 8000 fs delay. However, at this high of as delay, certain details from the sample was actually lost in the acquired images, possibly from saturation of the detectors. Because of this, it was decided to keep the delay at 0 fs when studying CH stretching, as the CARS signal still was very

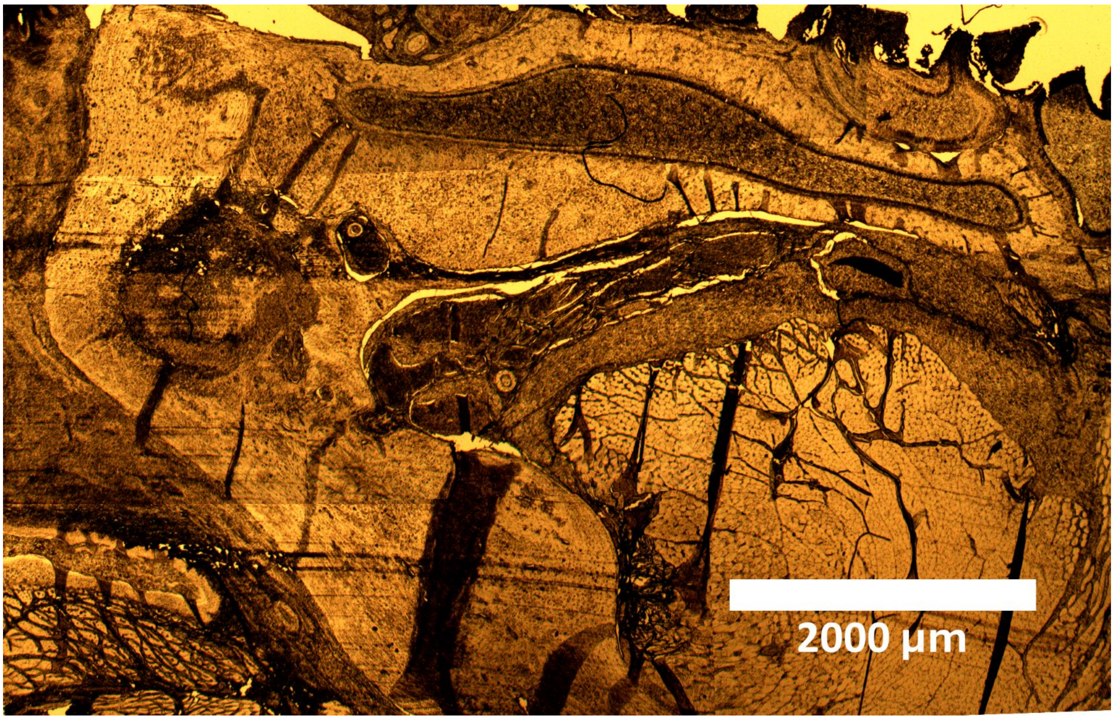

Figure 4.4.14: An overview image of the parts of a decalcified rat jaw section taken using an optical brightfield microscope. The image was made by merging multiple brightfield images.

strong here. For both spectra discussed above, as well as imaging of the area used for the acquisition of the data using both CARS and brightfield, see Figure 4.4.16.

Using wavenumber 2844.6 cm^{-1} and 0 fs delay, the sample was then imaged using the CARS. Some of the images acquired can be seen in Figure 4.4.17. An nerve bundle and arteriole was also imaged at wavenumber 988 cm^{-1} and 2844.6 cm^{-1}, in order to see if a strong enough ν_1 $\text{PO}_4{}^{3\text{-}}$ signal (through HAp) for detection/imaging still could be generated by the sample, and if this was the case, compare this HAp-signal with the signal from CH stretching. Background signal was also tested for by using only the pump laser. As the laser had two different values when testing for either CH stretching (λ_{pump} = 797.2 nm) or ν_1 $\text{PO}_4{}^{3\text{-}}$ (λ_{pump} = 935.7 nm), both were used. The results from this can be seen in Figure 4.4.18. Here, a signal from HAp can be seen, though as a whole it is weaker than the signal coming from CH stretching. This was expected, not only because the sample was decalcified, but also because the area scanned should be high on CH-bonds (arteriole and nerve bundle). The area around the nerve bundle and arteriole however looked to give a stronger ν_1 $\text{PO}_4{}^{3\text{-}}$ signal than a CH-signal. This also makes sense, as this tissue normally would primarily consist of HAp. One can also see that there is a background signal coming from the sample when testing for both CH-bonds and HAp, though this background signal is much weaker than the corresponding CARS signal.

The signals from Figure 4.4.18c and Figure 4.4.18a was then overlaid on-top of each other, in order to compare which area gave the strongest CARS signal from either CH-bonds or HAp. The result of this can be seen in Figure 4.4.19. Here, one gets the strongest CH-signal from the nerve bundle and arteriole, while the

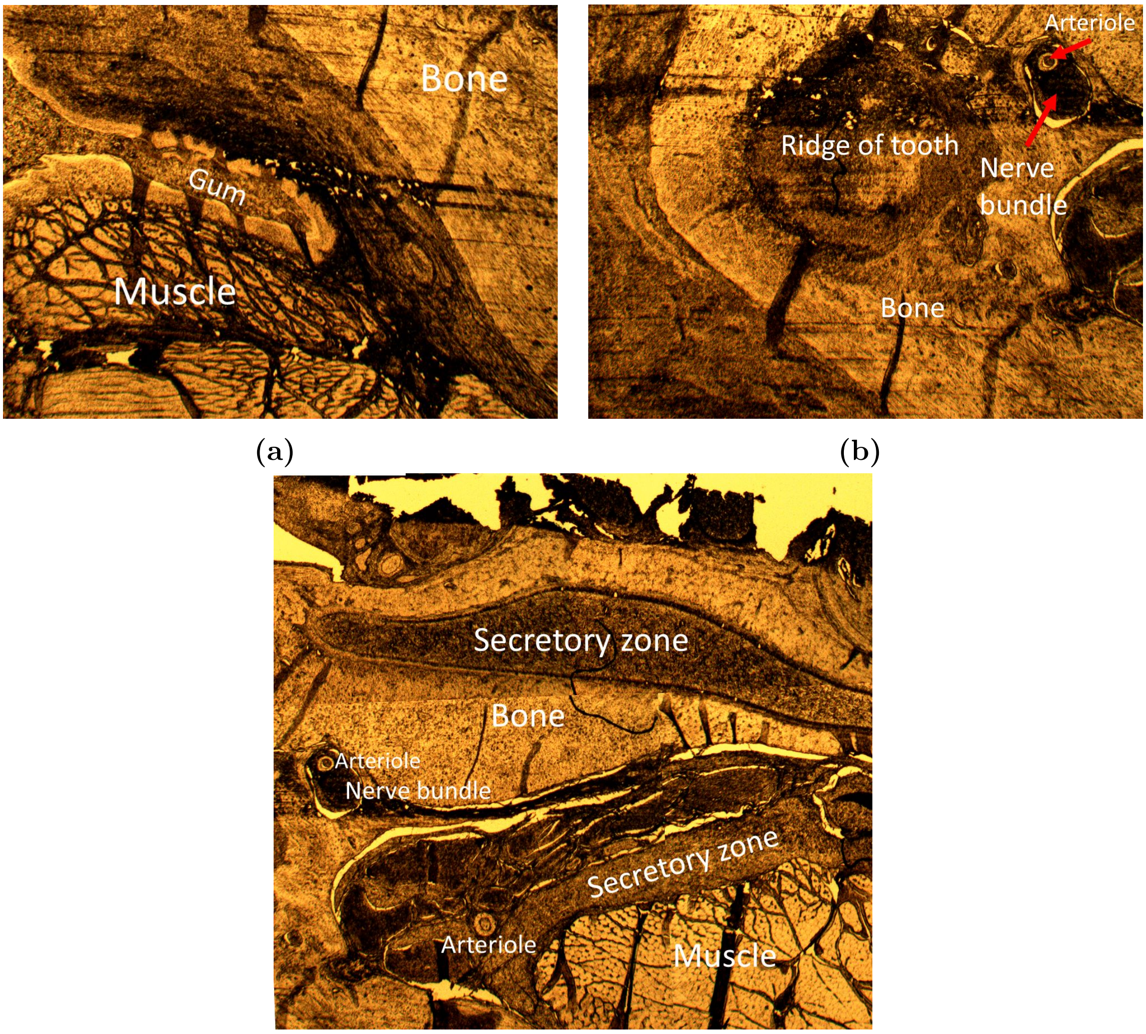

(a) **(b)** **(c)**

Figure 4.4.15: Brightfield image of a decalcified rat jaw section showing the difference between bone, muscle and gum **(a)**; brightfield image of a decalcified rat jaw section showing the ridge of a tooth, a nerve bundle and a arteriole **(b)**; brightfield image of a decalcified rat jaw section showing arterioles, nerve bundles, secretory zones, and muscle **(c).**

strongest HAp-signal comes from the surrounding bone tissue, as well as the bone tissue encapsulating the arteriole. There also seems to be some overlap between the two signals in the tissue directly encapsulating the nerve bundle.

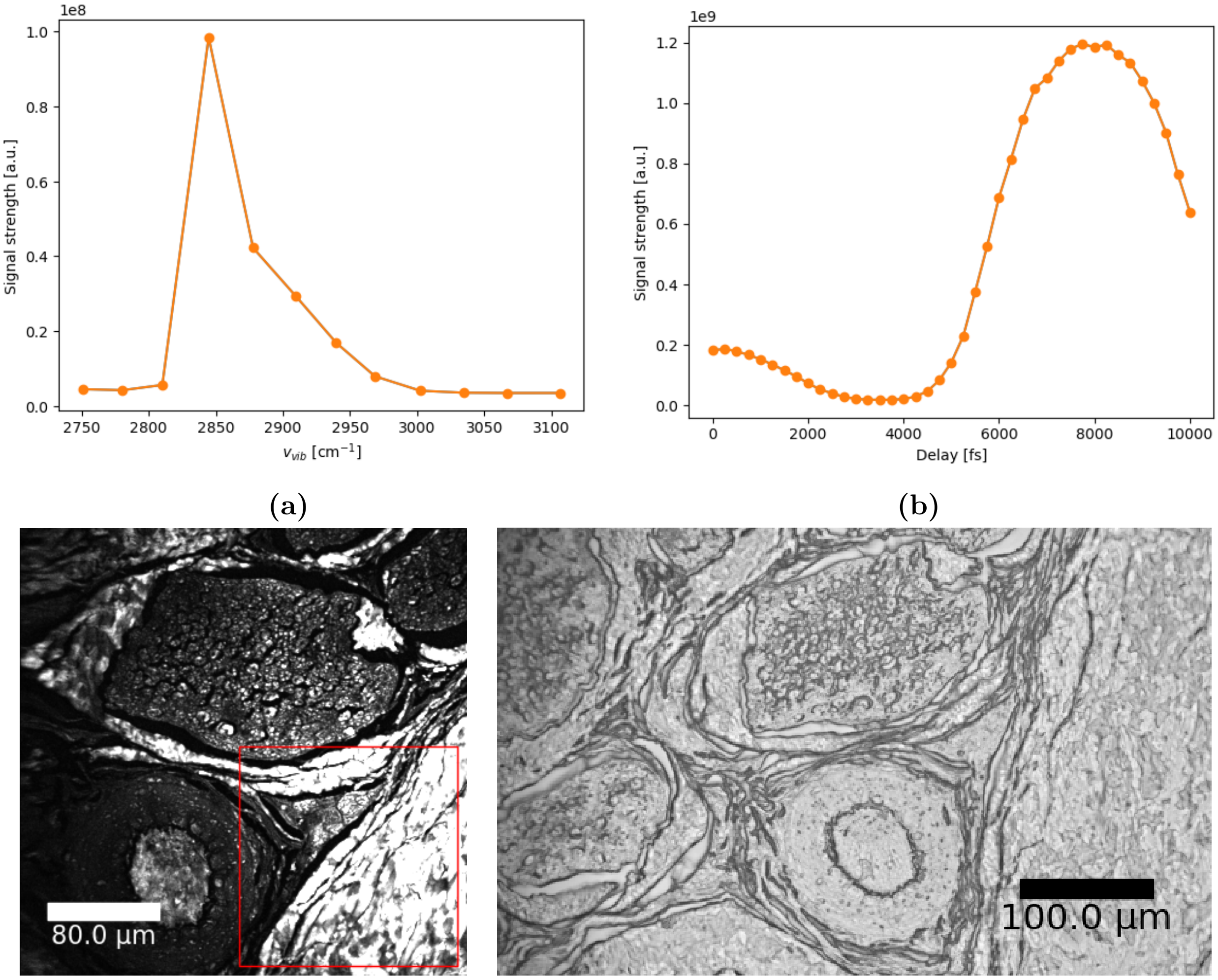

(a) **(b)**

(c) **(d)**

Figure 4.4.16: **(a)**: A spectrum comparing the signal strength at various values of wavenumber from the area marked in **(c)** using all the different images seen in Figure A.0.6. **(b)**: A spectrum comparing the signal strength at various values of delay from the area marked in **(c)** using all the different images seen in Figure A.0.7. **(c)**: CARS imaging of a decalcified rat jaw sample at wavenumber 2844.6 cm^{-1} (λ_{pump} = 797.2 nm, λ_{Stokes} = 1031 nm) and 0 fs delay. **(d)**: Brightfield imaging of decalcified rat jaw.

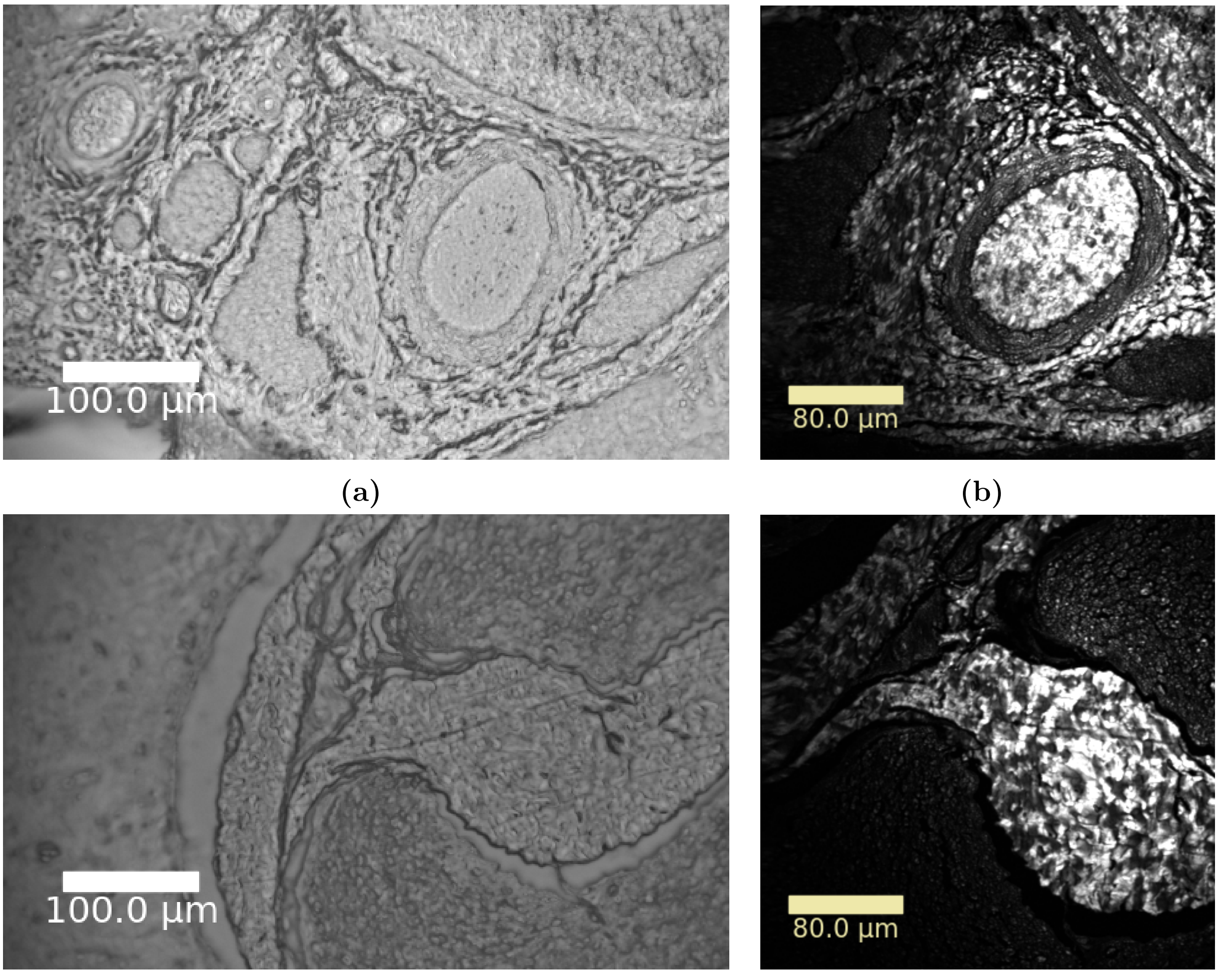

(a) **(b)**

(c) **(d)**

Figure 4.4.17: Brightfield images **(a,c)** and corresponding CARS images **(b,d)** of different areas of a decalcified rat jaw section. CARS images captured at 2844.6 cm^{-1} ($\lambda_{pump} = 797.2$ nm, $\lambda_{Stokes} = 1031$ nm) and 0 fs delay.

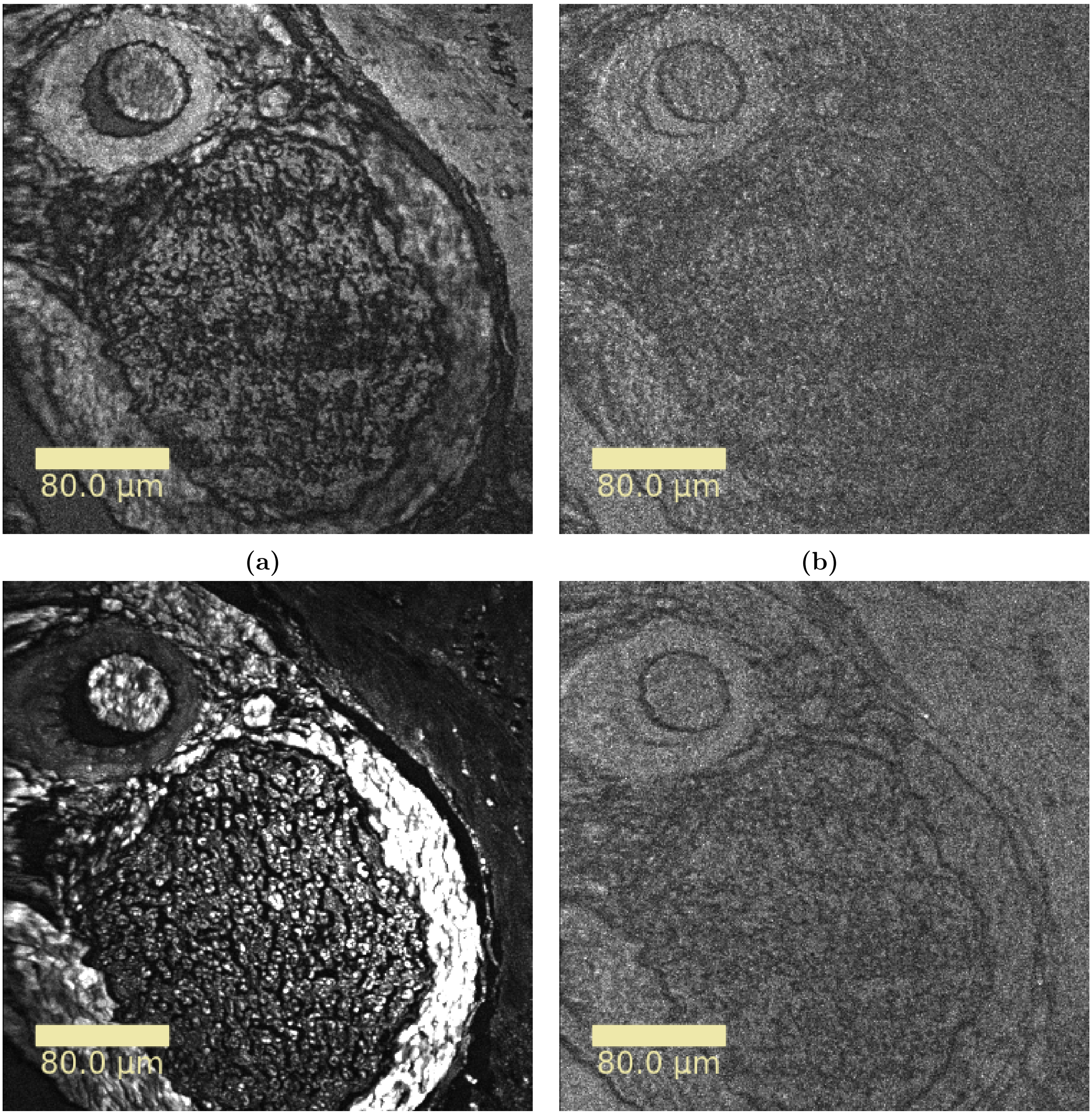

(a) **(b)**

(c) **(d)**

Figure 4.4.18: A CARS imaged captured of a nerve bundle and arteriole in a decalcified rat jaw section at wavenumber 988 cm^{-1} (2750 fs delay) **(a)**, wavenumber 2844.6 cm^{-1} (0 fs delay) **(c)**, and the corresponding background signal detected from the same area **(b, d)**.

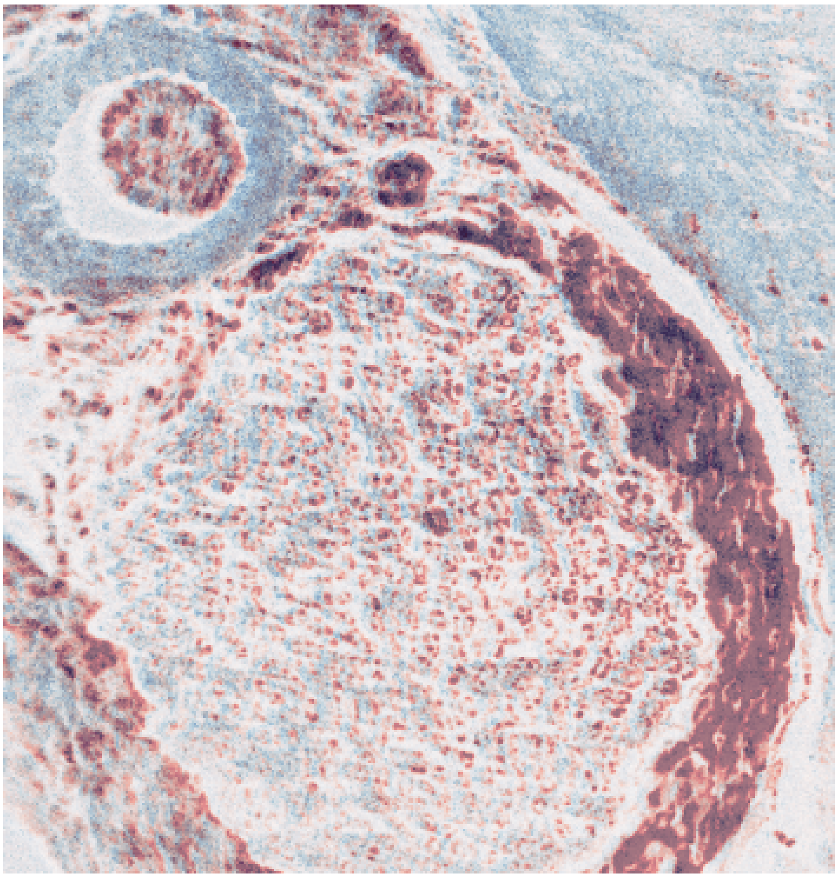

Figure 4.4.19: Comparing the signal strength from CH and HAp given in Figure 4.4.18c and Figure 4.4.18a. Red represents CH-bonds while blue represent HAp.

4.4.4 Rabbit leg embedded in MMA

The rabbit leg section of unknown thickness (though thicker than 10 µm), was also tested under the CARS microscope. As this sample both was from very different bone tissue than the other bone samples (leg-bone instead of jawbone), and was much thicker than most of the other samples (though the exact thickness was unknown), the goal was to see if any of these differences would affect the CARS process. As with earlier samples, and overview images was also taken of this section, and can be seen in Figure 4.4.20.

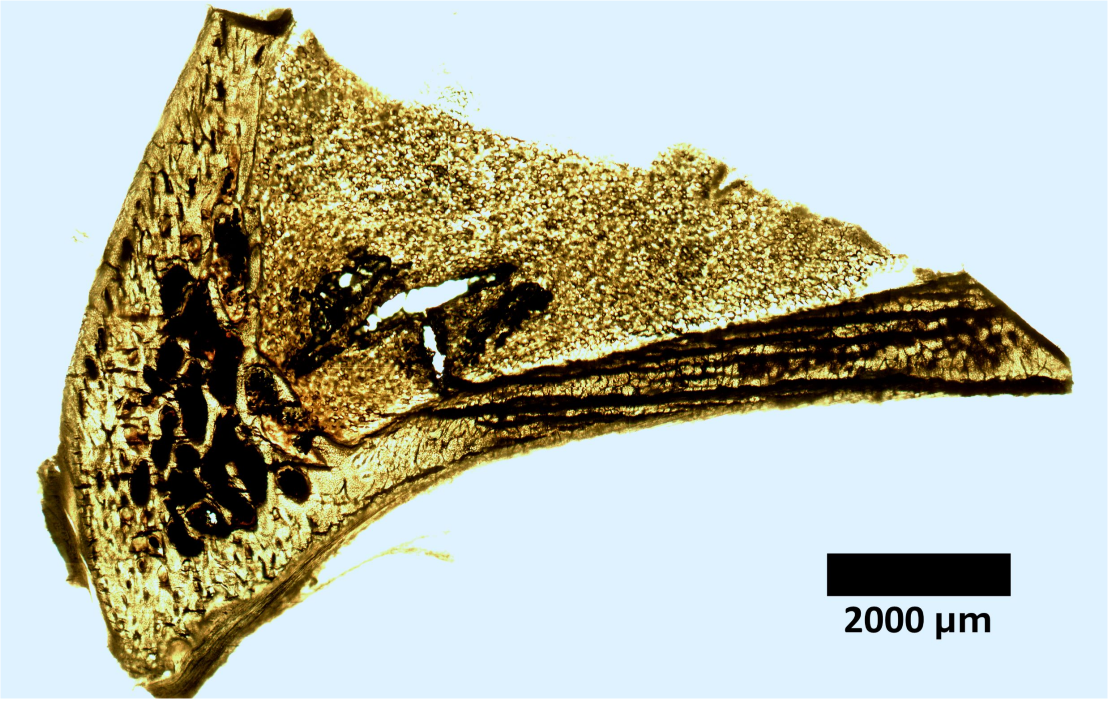

Figure 4.4.20: An overview image of the rabbitleg section taken using an optical brightfield microscope. The image was made by merging multiple brightfield images.

CARS imaging was then done on the sample (see Figure 4.4.21). The quality of the images acquired were not optimal, which pointed to the CARS signal from the sample being weak. Some reasons for this might be the samples thickness, and/or the layer of MMA surrounding the section. As described before, the thickness of a sample can affect the CARS signal from a sample. A thicker layer of MMA could also reduce the signal strength, but might also create a background signal that is stronger than the CARS signal from the sample. No matter the reason, the samples were still able to be imaged with the CARS method, which points to the ability for better imaging of samples like this through better sample preparation.

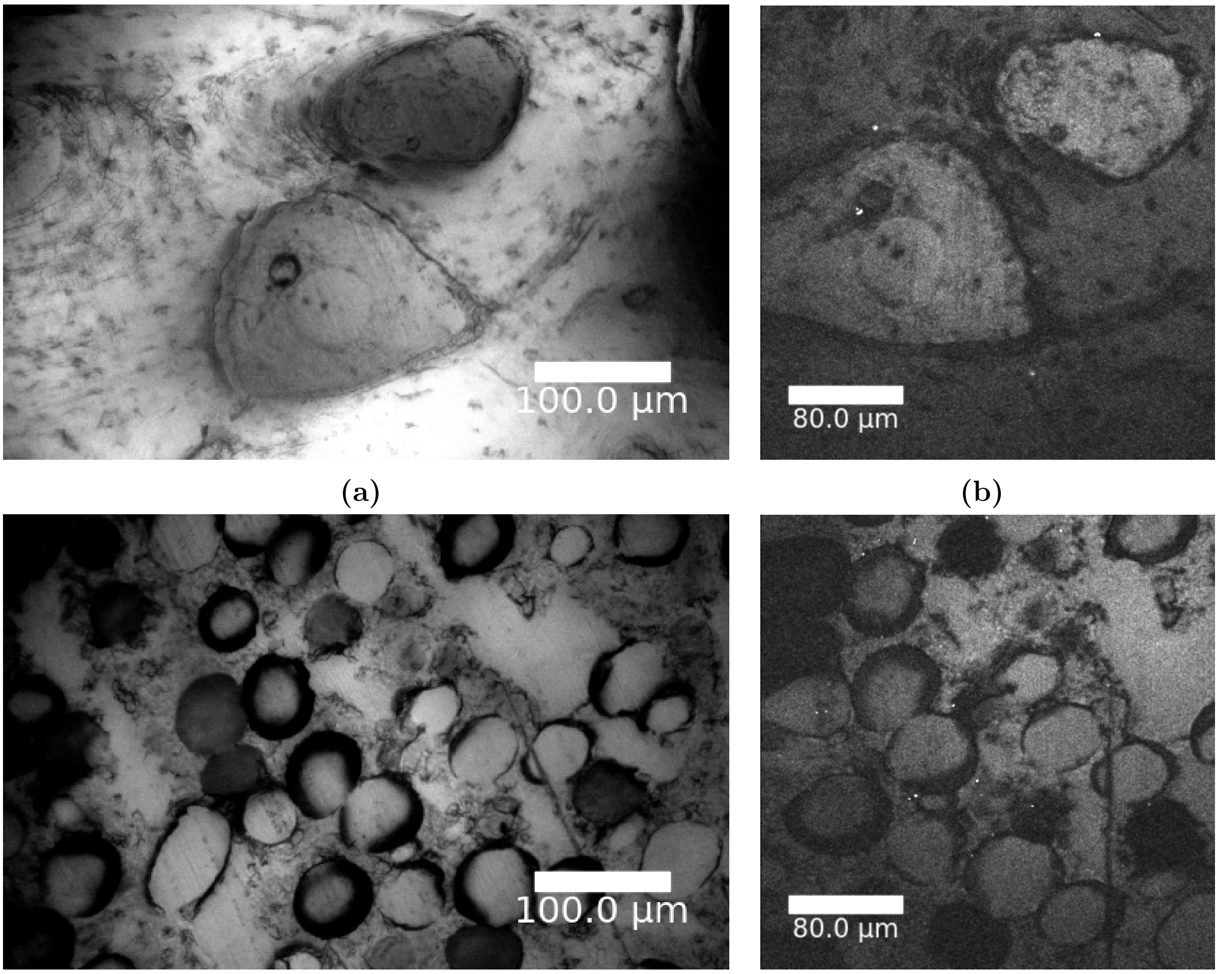

(a) **(b)**

(c) **(d)**

Figure 4.4.21: Brightfield images **(a,c)** and corresponding CARS images **(b,d)** of different areas of a rabitleg section embedded in MMA. CARS images captured at 988 cm^{-1} ($\lambda_{pump} = 935.7$ nm, $\lambda_{Stokes} = 1031$ nm) and 2750 fs delay.

4.4.5 Bone Marrow Biopsies and Bone Nodule

The two bone marrow biopsies with different width, as well as the one bone nodule, were studied using CARS in order to see if there were any difference in the CARS imaging of these types of bone samples when compared to those that came before. Overview images for the biopsies can be seen in Figure 4.3.8 and 4.3.10, while the overview images for the nodule can be seen in Figure 4.4.22.

Here, brightfield images were first taken of areas in the samples where one would expect there to be HAp, and therefore where one would expect to get a CARS signal at 988 cm^{-1}, 2750 fs delay. Then, these areas were scanned over using the CARS, and images acquired. The results of these can be seen in Figure 4.4.23 and 4.4.24 for the bone marrow biopsies, and in Figure 4.4.25 for the nodule. Here, one can clearly see that the structured imaged using brightfield also can be imaged using CARS.

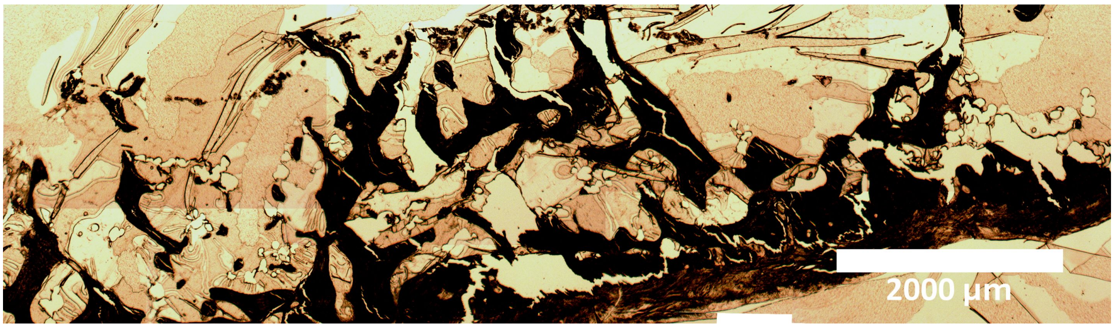

Figure 4.4.22: An overview image a the bone nodule (arthritis 1) taken using an optical brightfield microscope. The image was made by merging multiple brightfield images.

There are however some interesting observations obtained from these results as well. In Figure 4.4.23b, the compact bone surrounding the spongy bone structure depicted gives much less CARS signal than this structure. This again shows that even though the two bone types are just as thick as each other, the denseness of the compact bone leads to less CARS signal in trans direction. Another interesting result is all the spots that give a relatively strong (when compared to the surroundings) CARS signal in Figure 4.4.24b, 4.4.24d and 4.4.24f. While not so easy to see, these do in fact relate to similar spots seen in the corresponding brightfield images (Figure 4.4.24a, 4.4.24c and 4.4.24e). These spots might be areas where the calcified matrix is either thinner or thicker than the rest, though as the exact size thickness of this marrow biopsy hadn't been given (somewhere between 7-20 µm), which one it was is difficult to say. On the same sample, many small dark circles can also be seen in both the brightfield and CARS images (appear brown in the overview image). Because so little signal was received from these areas, as well as their different colouration when compared to the surrounding tissue, these areas were likely to be composed of non-calcified tissue of some kind. As there shouldn't be any fat or fat cells left in the sample after preparation, these might be the remains of blood or bone cells.

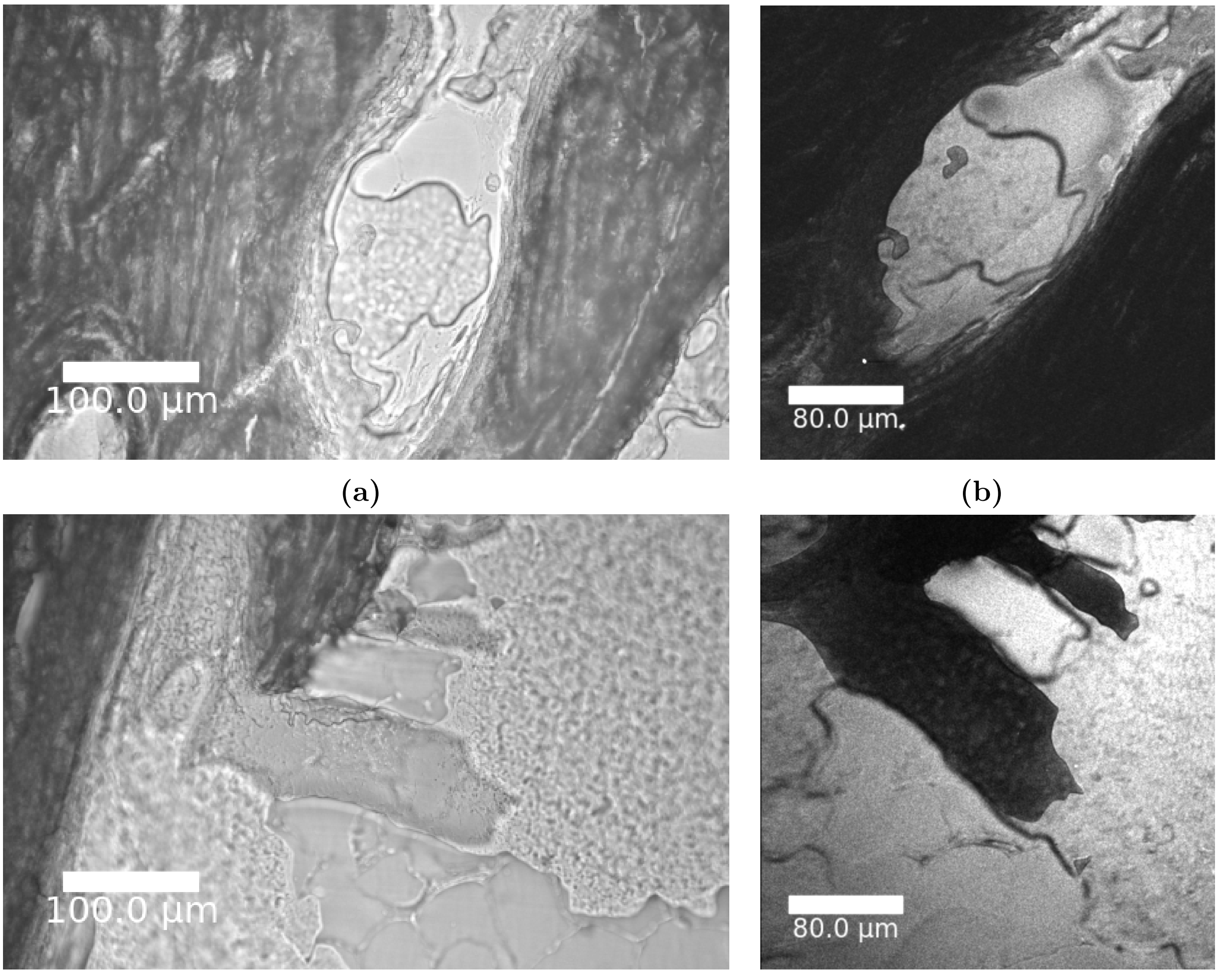

(a) **(b)**

(c) **(d)**

Figure 4.4.23: Brightfield images **(a,c)** and corresponding CARS images **(b,d)** of different areas of a 10 µm bone marrow biopsy. CARS images captured at 988 cm^{-1} ($\lambda_{pump} = 935.7$ nm, $\lambda_{Stokes} = 1031$ nm) and 2750 fs delay.

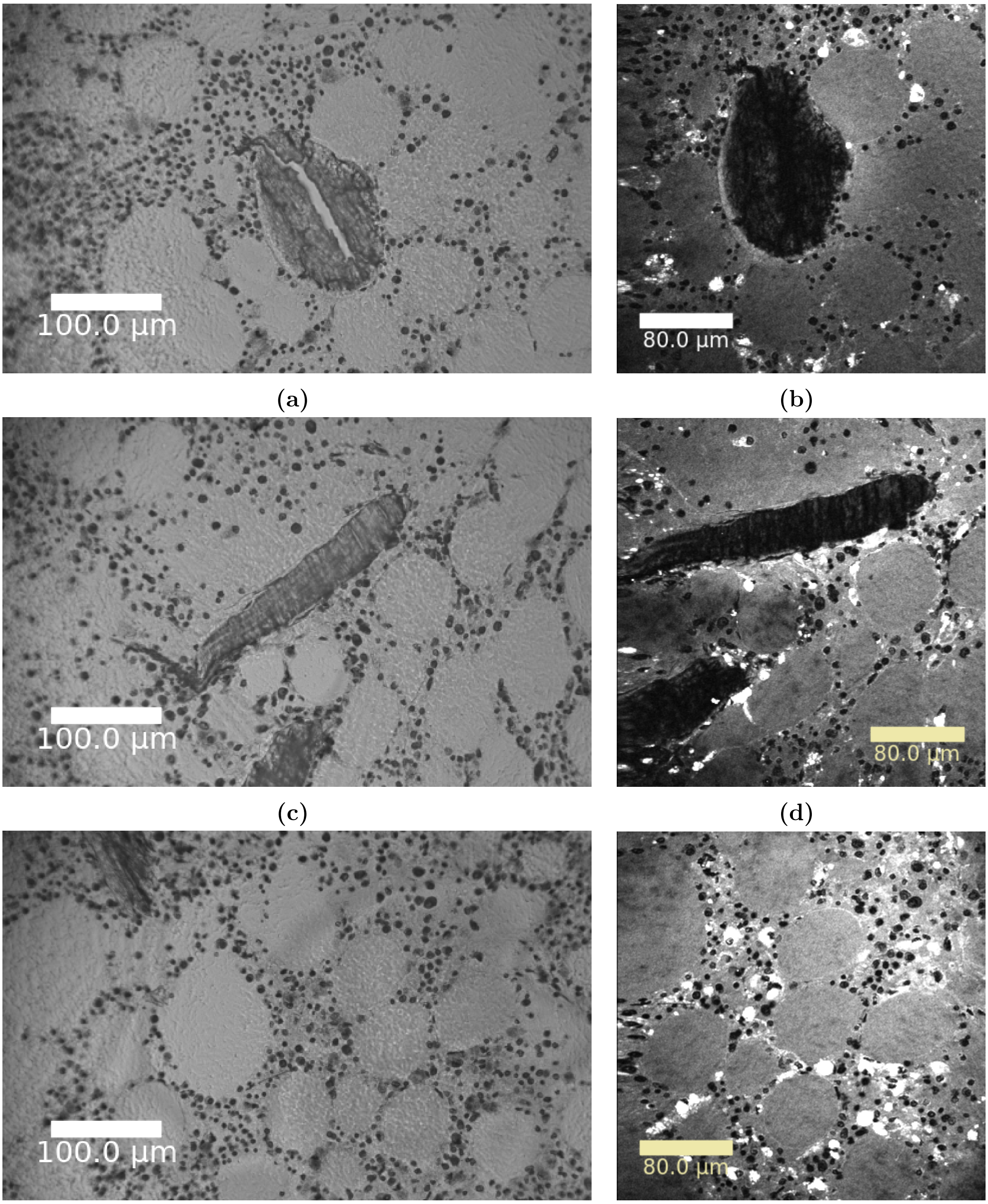

(a) (b) (c) (d) (e) (f)

Figure 4.4.24: Brightfield images **(a,c,e)** and corresponding CARS images **(b,d,f)** of different areas of a 7-20 µm bone marrow biopsy. CARS images captured at 988 cm^{-1} (λ_{pump} = 935.7 nm, λ_{Stokes} = 1031 nm) and 2750 fs delay.

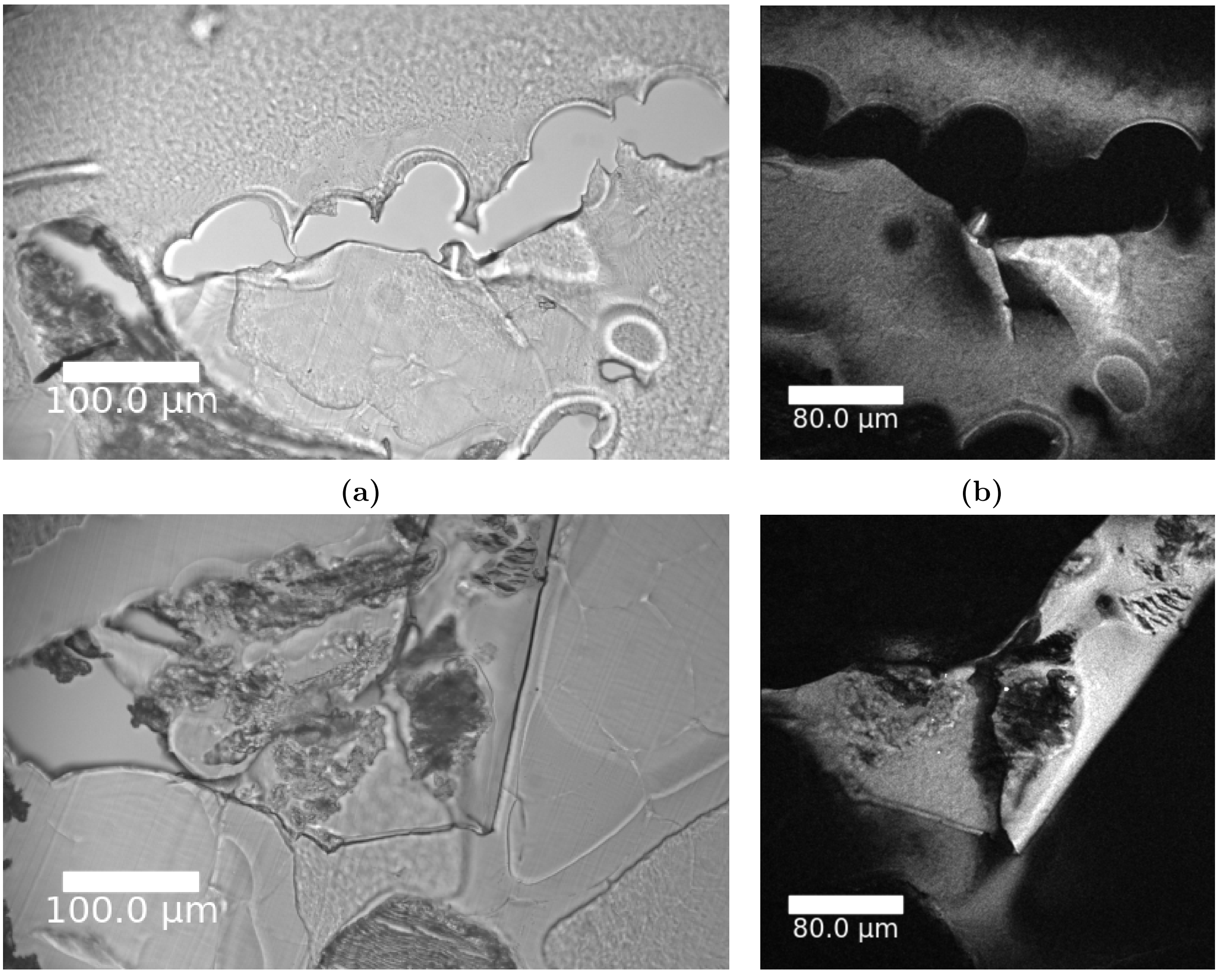

(a) **(b)**

(c) **(d)**

Figure 4.4.25: Brightfield images **(a,c)** and corresponding CARS images **(b,d)** of different areas of a bone nodule (arthritis 1). CARS images captured at 988 cm^{-1} ($\lambda_{pump} = 935.7$ nm, $\lambda_{Stokes} = 1031$ nm) and 2750 fs delay.

4.4.6 Cultured preosteoblasts

In order to confirm that the CARS-signal collected actually came from the calcium phosphate mineral HAp, and not from for example the material the samples were embedded in, two different MC3T3-E1 preosteoblasts samples (which had been cultured for 21/31 days) were tested. One of them was stained using ARS, while the other was not. The goal was to see if CARS-signal could be obtained from the calcified matrix made by the preosteoblasts when no MMA nor paraffin was present.

For the stained sample, the goal was to see if the CARS imaging showed the same structures as those seen with a brightfield microscope, in order to confirm that the CARS actually imaged the HAp found in the sample. An image taken of the stained sample by Marie E. Ullevålseter using an optical brightfield microscope can be seen in Figure 4.4.26. Different areas depicted on this image was then scanned using CARS, the resulting images being displayed in Figure 4.4.27. Here, one can clearly see that the structures depicted in Figure 4.4.27 are the same as the once in Figure 4.4.26, proving that the CARS method depicted the calcium phosphate in the tissue. One can also see structures in the CARS images that were not visible in the brightfield image.

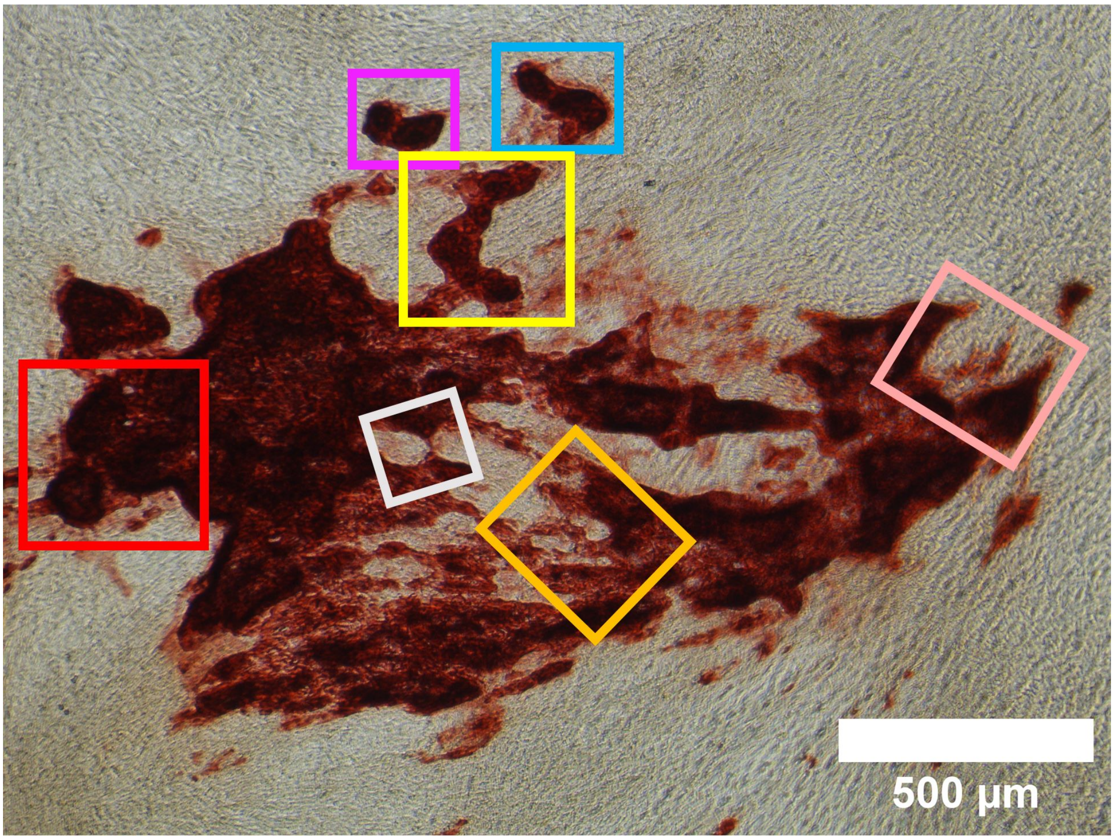

Figure 4.4.26: A brightfield image of stained hydroxyapatite tissue made by preosteoblast. The areas marked were depicted using CARS in Figure 4.4.27. Taken by Marie Eline Ullevålseter from NTNU's Faculty of Natural Sciences

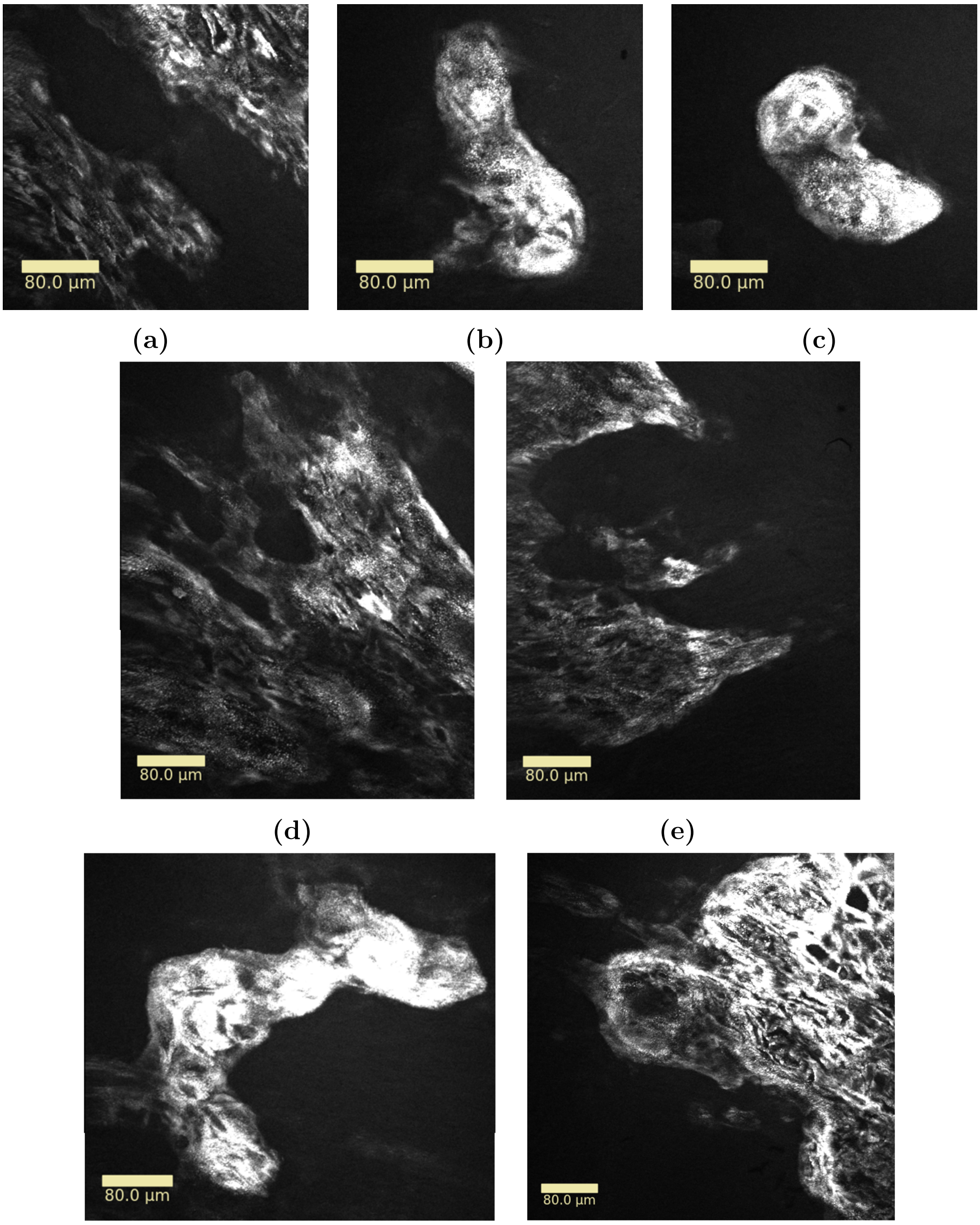

(a) **(b)** **(c)**

(d) **(e)**

(f) **(g)**

Figure 4.4.27: CARS images of stained hydroxyapatite tissue made by preosteoblast seen in Figure 4.4.26. Captured at 988 cm^{-1} (λ_{pump} = 935.7 nm, λ_{Stokes} = 1031 nm) and 2750 fs delay. **(a)** is the grey area, **(b)** is the blue area, **(c)** is the purple area, **(d)** is the orange area, **(e)** is the pink area, **(f)** is the yellow area, and **(g)** is the red area.

The non-stained sample was primarily used in order to find the wavenumber and wavelength where the calcified matrix gave the strongest signal, as had been done before. It was done on this preosteoblast-sample in order to make sure that ARS didn't affect the results. As there was no real structures in the sample (only calcified matrix), no overview image was taken.

For the wavenumber, the interval tested was between 886-1080 cm^{-1}, and for

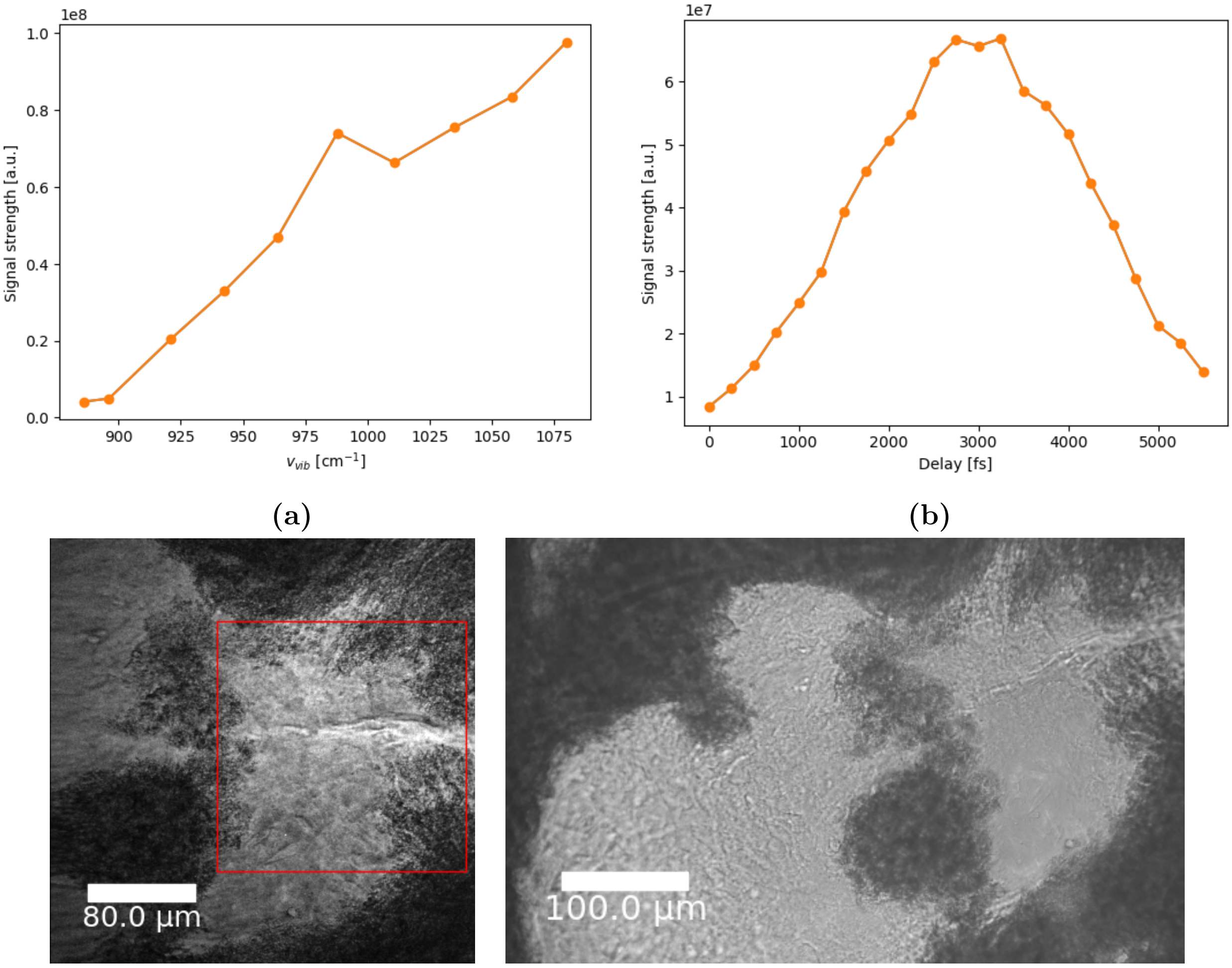

(a) **(b)**

(c) **(d)**

Figure 4.4.28: A spectrum made from preosteoblast tissue comparing the signal strength at various values of wavenumber using all different images seen in Figure A.0.8 (2750 fs delay) **(a)**, and delay using all different images seen in Figure A.0.9 (wavenumber 988 cm^{-1}) **(b)**. **(c)** is a CARS image of the preosteoblast tissue of the relevant area, with the area used to make (a) and (b) marked. **(d)** is a brightfield image of the same area.

the delay, the interval was between 0-5500 fs with jumps of 250 fs between each image acquired. The resulting spectra can be seen in Figure 4.4.28, along with a CARS and brightfield image of the area scanned. From this, one can see that there is a clear peak for signal strength at 988 cm^{-1}, though the signal strength seems to be increasing near linearly with higher wavenumbers. For delay, the strongest signal was acquired somewhere between 2750-3250 fs delay.

After re-alignment of the lasers, a wavenumber spectrum was also made for the stained sample from 884.9-1290.9 cm^{-1} (see Figure 4.4.29). While one can't see any peak at 960-988 cm^{-1}, peaks at around 1080 cm^{-1} (ν_3 PO_4^{3-} asymmetric stretching mode), 1173 cm^{-1} (may correspond to amid III) and 1244 cm^{-1} (amid III) can be seen. The signal strength seemed to increase with the wavenumber, in a near linear fashion, though it looks like this increase might stop at around 1250-1300 cm^{-1}, as the drop in signal strength after the 1244 cm^{-1} peak is larger

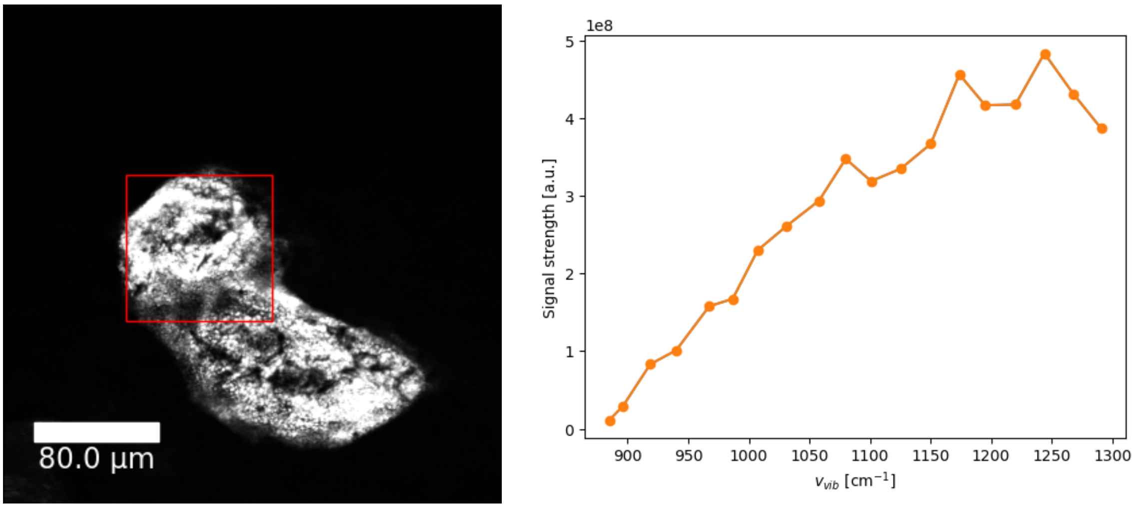

(a) **(b)**

Figure 4.4.29: **(a)**: CARS imaging of a cultured MC3T3-E1 preosteoblasts sample stained with ARS at wavenumber 1080 cm^{-1} ($\lambda_{pump} = 927.7$ nm, $\lambda_{Stokes} = 1031$ nm) and 2750 fs delay. **(b)**: A spectrum comparing the signal strength at various values of wavenumber from the area marked in **(a)** using all the different images seen in Figure A.0.10.

than that seen after the two other peaks.

4.4.7 Background

As the signal strength seemed to be increasing past the ν_1 $PO_4{}^{3-}$ for multiple different samples, and seemingly continued to increase up to at least 1300 cm^{-1} for the 7 µm dog jaw section, it was decided to investigate if this was caused by a background signal created during the CARS process. This was done by making a wavenumber spectrum from 886.1-1292.1 cm^{-1} of an area without any HAp. This was done after the re-alignment of the lasers. As the ARS stained preosteoblast sample gave a clear indication to where there was and wasn't any calcium phosphate (and therefore HAp), this sample was used for this. The spectrum obtained, as well as the area used to make it, can be seen in Figure 4.4.30. Here, one can clearly see an increase in signal strength as the wavenumber increases, even though there is no CARS signal coming from HAp. This means that something else, be it fluorescence or some other source, is creating this background signal. This increase also seem to be near linear, similarly to wavenumber spectra seen earlier.

After collecting the background signal, it was decided to check what kind of results would be obtained if one were to subtract it from a similar spectrum acquired from one of the bone samples. The spectrum chosen for this was the one captured from the 7 µm dog jaw section seen in Figure 4.4.6b. The result is the spectrum seen in Figure 4.4.31. While this spectrum still doesn't perfectly align with a typical bone Raman spectrum, one can still see many improvements from the original wavenumber spectrum. Three peaks can be seen, all corresponding to well known vibrational modes, being the ν_1 $PO_4{}^{3-}$ stretching mode around 960 cm^{-1}, the mode of A-type carbonate around 1125 cm^{-1}, and the mode for amid III at around 1250 cm^{-1}. The 1250 cm^{-1} peak did not appear in the original spectrum.

One can also see that the signal strength in the background subtracted spectrum decrease much more after the 1125 cm^{-1} peak than it did in the original spectrum, and that the signal strength starts to decrease after the 1250 cm^{-1}, something it didn't do in the original spectrum, where the signal strength continued to increase. While the peaks at 1125 cm^{-1} and 1250 cm^{-1} still are larger than the peak at 960 cm^{-1} also in the background subtracted spectrum, it still better represent a typical Raman spectrum for bone.

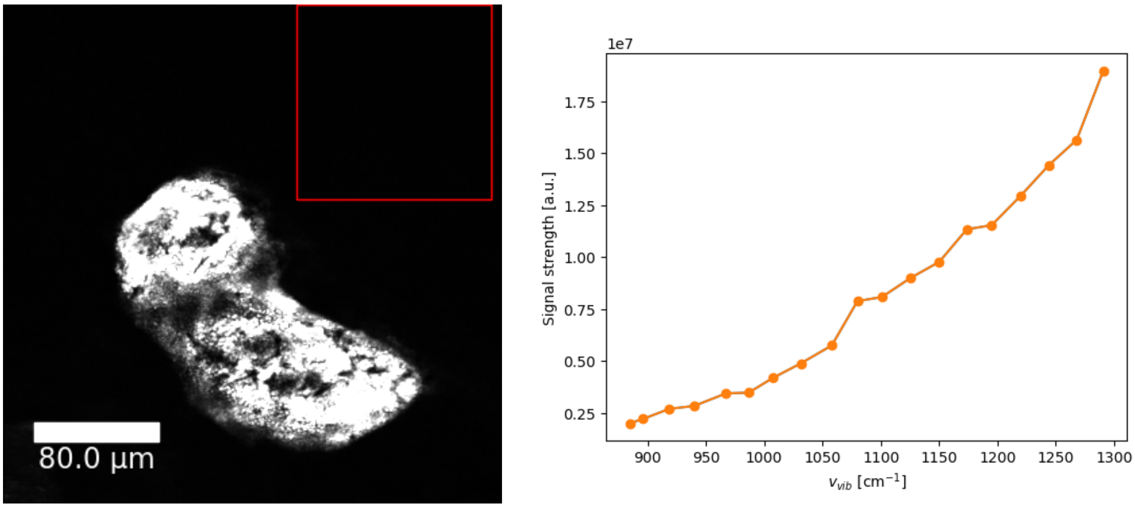

(a) **(b)**

Figure 4.4.30: **(a)**: CARS imaging of a cultured MC3T3-E1 preosteoblasts sample stained with ARS at wavenumber 988 cm^{-1} ($\lambda_{pump} = 935.8$ nm, $\lambda_{Stokes} = 1031$ nm) and 2750 fs delay. **(b)**: A spectrum comparing the signal strength of the background signal at various values of wavenumber from the area marked in **(a)** using all the different images seen in Figure A.0.10.

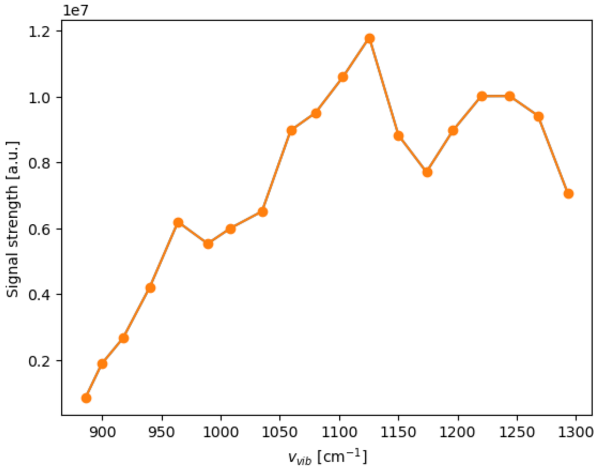

Figure 4.4.31: A wavenumber spectrum made by subtracting the background signal seen in Figure 4.4.29b from the wavenumber spectrum seen in Figure 4.4.6b.

4.4.8 Tooth Sections

Multiple human tooth sections were also tested using the CARS. These sections were the thickest of all of the samples, being around 0.5 mm, and was therefore tested in order to see if any CARS signal could be acquired when samples were this thick.

When scanning the tooth sections using CARS, the strength of the trans signal collected was very weak (see Figure 4.4.32b, e, h). A reason for this was likely the thickness of the sample. As discussed earlier, this might have affected the trans CARS signal in multiple ways:

1. The lasers were not able to penetrate deep enough into the sample so that a strong signal could be transmitted on the other side.
2. More of the laser's energy might have been absorbed by molecules deeper within the sample, and when these molecule released CARS-signal, a lot of the signal might have been absorbed by the material around the molecules.

An epi signal was also acquired from the sections, and though it was stronger than the trans signal, it was still weak (see figure Figure 4.4.32c, f, i). An interesting observation is that the areas of the section that gave an epi signal seems to be the inverse of those which gave a trans signal. In fact, no details from the areas giving epi signal were seen in the brightfield images either. These areas seemed to be corresponding to the pulp chamber of the tooth. Those who had prepared the sample suggested that this might be because of deterioration of the pulp chamber (the reason the tooth was originally extracted), which would have changed the structure of this area, perhaps making it more scattering than in the rest of the tooth. This could explain why the trans signal is virtually non-existent in this area, while the epi signal is at its strongest there. It should be noted that this was the only time an noticeable epi signal was collected with the faulty setup, which means that a better setup might have been able to acquire a much stronger CARS signal in this direction from these samples.

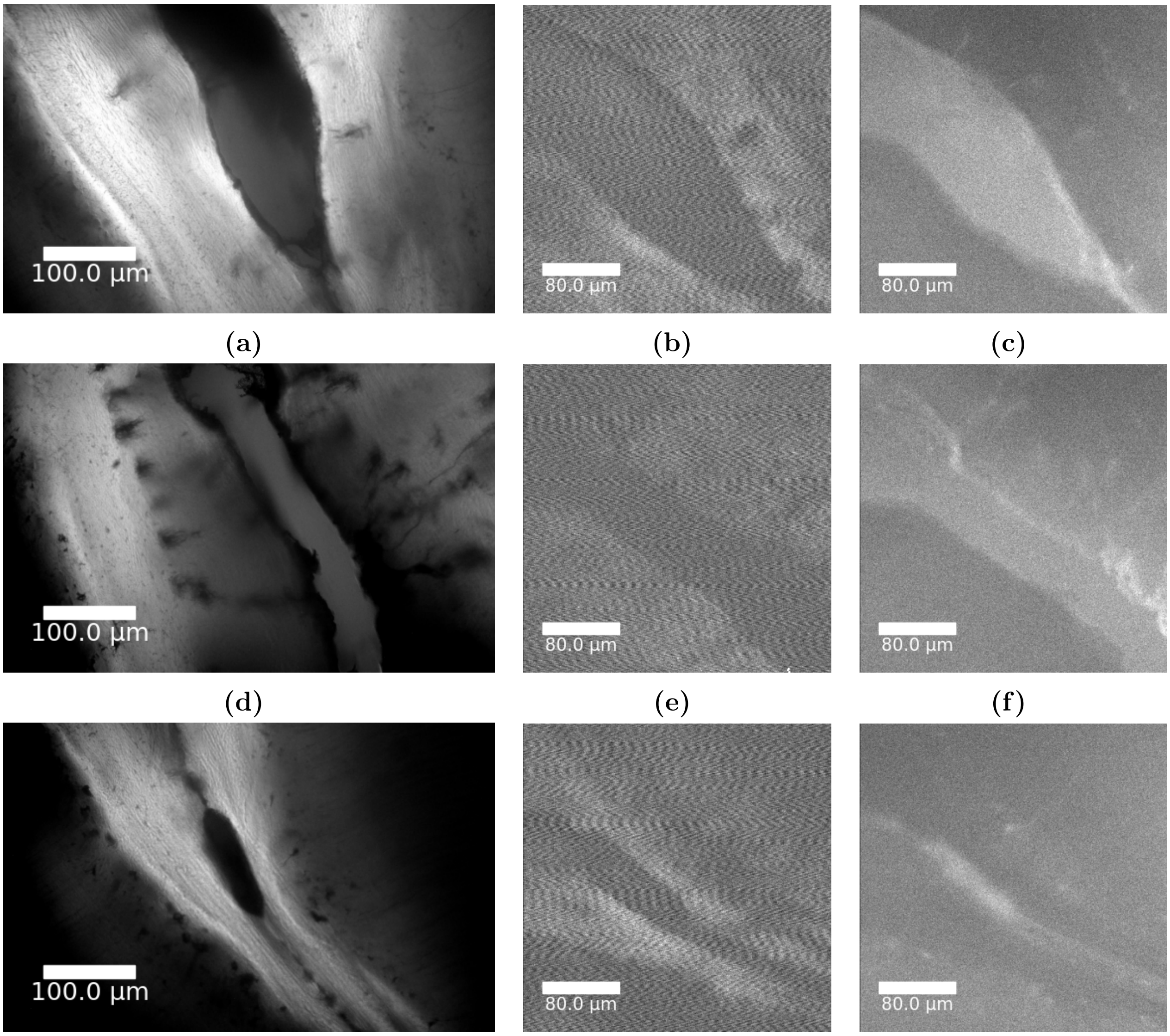

(a) **(b)** **(c)**

(d) **(e)** **(f)**

(g) **(h)** **(i)**

Figure 4.4.32: Images of different tooth sections acquired using brightfield **(a,d,g)**, as well as from CARS-signal in both trans **(b,e,h)** and epi **(c,f,i)** directions. CARS images captured at 988 cm^{-1} (λ_{pump} = 935.7 nm, λ_{Stokes} = 1031 nm) and 2750 fs delay.

CHAPTER FIVE

DISCUSSION

The goal of this master's thesis was to see if CARS could be used to image and study bone samples, primarily by using the Raman signal created by HAp in the tissue, though the Raman signal from CH-bonds was also considered. This was shown to be possible in trans direction using both wavenumber around 960-990 cm^{-1} among others for HAp, as well as for wavenumbers around 2845 for CH-bonds in the organic component. Samples with thickness between 5-20 µm were imaged without issue, while the image quality was noticeably worse for significantly thicker samples (discussed in more detail below). Samples embedded in both MMA and paraffin, as well as samples that wasn't embedded in any material, all were imaged without issue, showing that all three options could be used for bone tissue imaging using CARS. When looking at the Raman spectra collected from the different samples, the embedding material seemed to create some background signal, but at least for the thinner samples this extra signal did not seem to majorly affect the quality of images.

As mentioned above, a limitation with the CARS signal in trans direction was seen when trying to image the thicker samples. Here, the quality of images collected was much worse than those from the thinner samples. For both the thicker dog jaw sample and the rabbit leg sample, much more background signal was also detected from both the Raman spectra collected using the Raman microscope, as well as from the wavenumber spectrum made using the CARS. The source of this background signal may have been either fluorescence and/or non-resonant background signal. The reason the thicker MMA embedded samples creates more background signal may have to be because of the thickness of the sample, and/or the thickness of the embedding layer of MMA. Some of this signal might also have been CARS signal created by the embedding material. As seen by the tooth section, the increased background signal isn't the only reason for the worse signal quality in the trans direction, as the tooth sections weren't embedded in anything. The tooth sections were by far the thickest samples, and gave the worst trans signal out of any of the samples, showing just how much the thickness of the sample can affect the amount of CARS signal generated. This could be because the lasers were not able to penetrate deep enough into the thicker sample, so that a strong signal could be transmitted on the other side, and/or that more of the lasers' energy had been absorbed by molecules deeper within the sample, where much of the released CARS-signal created by these molecules was stopped by the material around them. Unfortunately, as the thickness of the thicker samples wasn't known, and in the case of the tooth sections only assumed based on eye measurements, it is difficult to say at exactly what thickness the CARS signal in trans direction becomes weaker. It should however be noted that even the tooth sections did give some trans signal, even at their relatively large thickness. This shows that the range of thickness in which a trans signal can be created is relatively large. This might also help explain why compact bone tissue, while still giving of a strong Raman signal around 960 cm^{-1} according to the Raman spectra collected, was harder to image using the CARS signal in trans direction when compared to spongy and trabecular bone tissue. As compact bone is much more dense than spongy and trabecular bone, there is the possibility that the lasers simply weren't able to penetrate as deep into the tissue as it would with spongy/trabecular bone.

In theory, when a sample is too thick/too dense to be imaged properly using the CARS signal in the trans direction, one should be able to use the signal created in the epi direction instead. However, little to no CARS signal was acquired in this direction for most of the samples tested, no matter the thickness or denseness of the tissue. A possible reasons for this might have been alignment issues with the lasers. However, as the lasers were re-aligned during the master's, and this still didn't lead to better epi signal, this probably wasn't the reason. Another possible explanation was the instrumental setup, as the filters in the dichroic epi cube had been mounted incorrectly. Unfortunately, there was no time to investigate this any further. No matter the reason, CARS signal in epi direction was collected from the tooth section, although only in small amounts and only from specific parts of the samples. As this was the only time noticeable epi signal was collected with the faulty setup, a better setup might be able to acquire a much stronger CARS signal from these samples in the epi direction. If this is the case, then there is also the possibility that a better setup might be able to collect epi signal from the other bone and preosteoblast samples as well, especially from more dense areas of the samples, like cortical/compact bone, as well as from the thicker samples, as there here would be more molecules which could scatter the CARS signal back in the epi direction. It should however be mentioned that when looking at CARS signal at around 2845 cm^{-1}, no epi signal was collected. Here, the setup of dichroic and filter cubes were the same in both trans and epi direction, so a faulty setup could not be blamed for the lack of signal. The only samples tested around 2845 cm^{-1} were however thinner ones, and only in areas with trabecular bone tissue. While this might suggest that the thinner samples, at least where the tissue was less dense, might not produce any epi signal even with a better setup, this still doesn't count out the possibility that the thicker/denser samples might.

The CARS technique was also show to be able to distinguish between different types of tissue based on the Raman active vibrations. This was done by comparing the signal strength recorded from HAp and CH-bond vibration over the same sample area. This was done for a 7 µm dog jaw section and for a decalcified rat jaw section. For both samples, data was collected from an area that contained a nerve bundle, a arteriole or blood vessel, and HAp matrix. By looking at the resulting images, one could clearly see that the different tissue types gave their strongest Raman signal at different wavenumbers (see Figure 4.4.7 and 4.4.18). To illustrate this further, signals were overlaid using different colours maps as shown in Figure 4.4.8 and 4.4.19. There might however be some limitations to this, as it was difficult to distinguish the blood vessel depicted in the dog jaw section from the surrounding HAp tissue. Another way separation between tissues was done was with the 7-20 µm bone marrow biopsy. When looking at the overview image of the sample (Figure 4.3.10), one could clearly see a brown-coloured tissue that differentiated itself from the surrounding bone tissue. That this tissue indeed was different from the bone tissue was confirmed by the Raman spectra collected from both tissues, as these were very different from one another. When this sample later was imaged using CARS at wavenumber 988 cm^{-1}, the bone tissue was easily depicted thanks to the strong CARS signal, while the brown tissue gave little to no signal at this wavenumber, appearing dark in the CARS images. As the Raman spectrum for the brown tissue had shown no Raman shift around 960 cm^{-1}, this wasn't unexpected. It should also be noted that while the compact bone also gave less signal than the spongy bone in these images, this most likely was due to the compact bone being more dense than the spongy bone, as discussed above.

While the Raman spectra captured using the Raman microscope are similar to that typical for a bone sample, there still was some uncertainty about if the CARS signal collected actually came from HAp, or if it came from another source such as the embedding material. This however was levied by the results obtained from the cultured cells that under specific conditions produced mineralized bone matrix. For the results from the non-stained sample, not only did the Raman spectra collected show Raman active vibrations at many of the same wavenumbers as the different bone samples, but the wavenumber spectrum created by using the CARS signal collected from this sample was also similar to the wavenumber spectra from the other non-decalcified samples. For the results from the stained sample, by comparing the structures seen using brightfield imaging with those seen using CARS imaging, the same structures could be seen using both techniques. As these samples were not embedded in MMA, this seemingly confirmed that it was CARS signal from HAp that was collected during the experiments.

When imaging the HAp tissue in the stained preosteoblast sample using CARS, many more details became visible when compared to the images acquired from the same areas using brightfield. This showed that under the right circumstances, CARS imaging could give better results than brightfield imaging. The difference in image quality between CARS and brightfield was much higher for the stained sample than for the non-stained one. This is most likely because the light from the brightfield microscope was hindered from travelling through the stained sample because of the ARS staining, something that wouldn't be a problem for the non-stained sample. As the CARS technique is based on the molecular vibration created by a the molecules in a sample, CARS imaging wouldn't be affected by the staining in the same way (if at all).

Something that became apparent when looking at the HAp wavenumber spectra collected using CARS, was that they did not match the Raman spectra collected using the Raman microscope. The signal strength was apparently growing as the wavenumber was increasing, leading to what could be considered the base line signal strength passing the height of the ν_1 $\mathrm{PO_4}^{3-}$ stretching peak. Even the thicker dog jaw section, which had more background signal according to its Raman spectrum than the most of the other samples, still had the ν_1 $\mathrm{PO_4}^{3-}$ stretching peak as its highest peak between 900-1080 cm^{-1} (the interval of the wavenumber spectrum made for this sample) in its Raman spectrum. Peaks that should appear in the wavenumber spectra also didn't appear, like the ν_1 PO_4^{3-} stretching peak for the thicker dog jaw section and the stained preosteoblast sample, or the amid III peak for the 7 µm dog jaw section. One explanation for this was with the wavelengths reflected by the dichroic mirror cube. When looking at the Equation 2.15 and Equation 2.17, one can see that a higher λ_{pump} correlates to a higher λ_{CARS}, while also correlating to a lower v_{vib} (wavenumber). This could mean that at higher wavenumbers, more signal with values higher than the expected Raman shift might be reflected by the dichroic mirror cube towards the detector, and that this might have impacted the signal detected. This explanation does however have a few flaws. The biggest one is that it completely ignores the filter placed between the dichroic mirror cube and the detector, whose sole purpose is to stop any excess signal from entering. While one could assume that this filter was flawed in some way, as two different filters (832 ± 18 nm and 857 ± 15 nm) were used, this becomes much more unlikely. Another point against this explanation is that this growth did not appear when creating a wavenumber spectrum for the CH-bonds at 2750-3100 cm^{-1}. If the dichroic mirror cube was to blame, one would expect the growth to appear here to. It should also be noted that this growth did not show up when testing DCPD in the author's specialisation project (TFY4520), which is why it was never mentioned. Here, the same dichroic mirror cubes and filters were used as those used when looking at the CARS signal from HAp.

Another explanation for this phenomena was that this apparent increase in base line signal strength was created by some kind of background signal, be it from fluorescence and/or non-resonant background. While some kind of signal coming from the embedding material had been proposed, the unforeseen growth also appeared in the wavenumber spectrum from the non-stained cultured preosteoblasts, which had not been embedded in anything. In order to find this background signal, a wavenumber spectrum had to be made from an area without any HAp, in the same interval as one of the HAp wavenumber spectra (here 886-1292 cm^{-1}). The area chosen was from the stained preosteoblast sample, as it here was very easy to see where one could and could not find HAp. This spectrum was then subtracted from the HAp wavenumber spectrum made from the 7 µm dog jaw section. The resulting spectrum made from this (see Figure 4.4.6b) was much more similar to what one would expect from a bone Raman spectrum. The A type carbonate peak was much clearer (higher drops in signal strength around it), which fit well with what was seen in the Raman spectrum corresponding to the 7 µm dog jaw section. The amid III peak also appeared here, and the signal strength even seemed to drop off at the higher wavenumbers, instead of just continuously growing as seen in the original wavenumber spectrum for the dog jaw section. While there still was discrepancies between the new wavenumber spectrum and its corresponding Raman spectrum, with the A carbonate and amid III peaks still being higher than the ν_1 PO_4^{3-} stretching peak, it did seem to work as proof for there indeed being a background signal which too was captured when using the CARS. A thought was to look at the weird Raman spectrum collected from what was believed to be some kind of background signal, obtained from the two dog jaw sections, and see if this might come from the source of the background signal seen in the wavenumber spectra. While this spectrum did show an increase in base line signal strength that might be similar to the one seen in the wavenumber spectra, many more peaks appeared in this spectrum than did in the wavenumber spectrum collected from the same sample. Whatever created this Raman spectrum therefore most likely wasn't the main source of the background signal. More work should therefore be done in order to not only find the source of the already collected background signal, but also in order to find the source of the other discrepancies not explained by this background signal.

Many interesting results were found when the different Raman spectra collected from the different samples were compared with each other. One of these related to the peak seen around 810-890 cm^{-1} in many of the spectra collected from the MMA embedded bone samples. This peak had originally been assumed to correspond to vibrations coming from proline/hydroxyproline, as these amino acids had their Raman active vibrational peak at around this wavenumber. For all the samples embedded in MMA however, the strength of this signal was much higher than one would expect when compared to the typical Raman spectrum for bone. While proline/hydroxyproline primarily is found in the collagen, which is found within the bone matrix, the surrounding HAp might prohibit the creation of much signal from these amino acids, which explains why a typical Raman spectrum usually shows the proline/hydroxyproline peak as really small. This however raises the question as to why this signal is so strong for the embedded bone samples. Looking at the spectra from the decalcified rat jaw section might provide some answers. The spectrum collected from a nerve bundle shows a peak at 890 cm^{-1}, though its size when compared to the other peaks is much smaller. As collagen can be found in the extracellular matrix surrounding the surface of Schwann cell/axon units, as well as arterioles and blood/lymphatic vessels, it makes sense for these types of tissues to give off a proline/hydroxyproline Raman signal. Here one however see that the peaks from A and B-type carbonate, amid III and CH bending should be larger than that of proline/hydroxyproline. This further raises the question as to why this isn't the case for the MMA embedded bone samples. There is however one big difference (other than the decalcification) between the MMA embedded bone samples and the decalcified rat jaw section, and that is that the rat jaw section was embedded in paraffin. MMA does have a Raman active vibrational peak at around 850 cm^{-1}, and this might help explain why the 810-890 cm^{-1} peaks are so much larger than one would expect in the MMA embedded bone samples, but not in the rat jaw section. This is further supported when looking at the spectra collected from the non-stained cultured preosteoblast sample and the tooth section. Non of these were embedded in MMA, and their corresponding Raman spectra did not show any peaks around 810-890 cm^{-1}. This might also explain some other discrepancies between a typical bone Raman spectrum and those collected from the MMA embedded bone samples. In all these samples, the CH bending peak is shown as larger than the ν_1 $\text{PO}_4{}^{3-}$ stretching peak. This is not the case for the spectra collected from the non-stained cultured preosteoblast sample and the tooth section, where this peak is much smaller. The spectrum from the decalcified rat jaw section also show this peak as smaller than the A and B-type carbonate peaks and the amid III peak. MMA also have a Raman active vibrational peak at around 1450-1480 cm^{-1}, and might therefore have affected the Raman spectra collected from the samples embedded in the material. While it was attempted to capture a Raman spectrum from the MMA, in order to see at what wavenumbers the MMA signal might have had an effect on the collected Raman spectra, no spectrum relating to MMA was obtained.

Another unexpected result seen in every Raman spectra collected, was the size of the CH stretching peak. While a CH-signal is consistent with the sample morphology, it should, according to a typical bone Raman spectrum, be much weaker than the ν_1 PO_4^{3-} stretching signal, but that is simply not the case for the Raman spectra collected. As this discrepancy appear in all Raman spectra, also those which wasn't embedded, this discrepancy is not the fault of the embedding material. In fact, the relation between the CH streaching peak and the PO_4^{3-} stretching peak was closer to what one would expect in the Raman spectrum collected from the bone nodule (embedded in MMA) than in the spectrum collected from the non-stained preosteoblast sample (not embedded). The exact reason for this observed difference is therefore unclear However, even if not all the signal received at 2700-3000 cm^{-1} is from the sample itself, one can still use these wavenumbers to depict and analyse the samples using CARS. As seen when analysing both the 7 µm dog jaw section and the decalcified rat jaw section at 2844.6 cm^{-1}, is that the CARS signal created from nerve bundles and arterioles is much stronger than the signal created from the surrounding HAp tissue. This signal was also able to image the samples in these areas without any noticeable problems.

CHAPTER

SIX

CONCLUSIONS

In this master's thesis, it was tested if CARS spectroscopy could be used for imaging and further study of bone and bone like samples. Imaging was done using both the Raman signal acquired from HAp in the sample tissues, as well as from CH-bonds. Many different samples were tested here, including dog jaw sections of different thickness, a decalcified rat jaw section, a rabbit leg section, two bone marrow biopsies of different thickness, a bone nodule, two samples consisting of mineralized bone matrix produced by cultured preosteoblasts (one which had been stained by ARS), and tooth sections.

While there were few problems collecting CARS signal in the trans direction from the samples (with the exception of the tooth sections), almost no epi signal was collected from any of the samples. The exact reason for this is unknown, but can have been because of a faulty filter setup. Either way, some epi signal was collected from the tooth sections, showing that it was possible to collect epi signal from tissue similar to bone.

In order to confirm that the signal thought to come from HAp, actually came from this tissue, a sample consisting of mineralized bone matrix produced by cultured preosteoblasts, and stained using ARS, was used. By comparing images captured of the stained tissue using an optical brightfield microscope, with those seen through CARS imaging of the same tissue, one could confirm that the same structures were seen in both.

Multiple Raman spectra were collected from each sample used. These were made in order to confirm at what wavenumbers would give Raman active vibrations from the different samples, compare these spectra with that of a typical bone Raman spectrum, and than later compare these results with the results from CARS microscopy.

The signal strength at different values of both wavenumber and delay were tested for the signal from both HAp and CH-bonds. For CH-bonds, the signal strength was at its strongest around 2844.6 cm^{-1} and 8000 fs delay, thought the signal also was strong around 0 fs delay. 2844.6 cm^{-1} and 0 fs delay was then chosen as the values used for imaging using the CH-bond signal from the samples. For the HAp signal, it seemed to be strongest somewhere between 2250-3250 based on either the sample tested (dog jaw section or cultured cells that under specific conditions produced mineralized bone matrix) or the wavenumber (960 or 988 cm^{-1}). For the wavenumber which gave the strongest CARS signal, the results weren't as conclusive, but seemed to show a signal strength peak at either 960 or 988 cm^{-1}. 2750 fs delay and 988 cm^{-1} was chosen as the primary values used for imaging using signal from the HAp-tissue.

While testing the HAp-signal strength at different wavenumbers, the spectra collected showed an unexpected increase in base line signal strength corresponding to the increase in wavenumber. This made the signal strength spectra collected very different from the Raman-spectra collected from the same samples. In order to test if this might have been because of some kind of background signal creeated by the samples, a signal strength spectrum (at different wavenumbers) was made from an area without any HAp. This spectrum was then subtracted from a 7 µm dog jaw spectrum made using the same wavenumbers. The resulting spectrum was much closer to both the Raman spectrum collected from the dog jaw section, and to a typical bone Raman spectrum, showing that there most likely that some background signal indeed was present. The exact source of this background signal was however unknown.

In order to see if the CARS technique could differentiate between different types of tissues, three different types of samples, a 7 µm dog jaw section, a 5 µm rat jaw section, and a 7-20 µm bone marrow biopsy, was used. For the bone marrow biopsy, bone tissue was tested up against an unknown tissue in the sample. The bone tissue was easily imaged using CARS at 988 cm^{-1}, while the unknown tissue was not. Raman spectra from both tissues were also obtained, which confirmed that they indeed were different. For the 7 µm dog jaw section and the 5 µm rat jaw section, signal was collected at 988 and 2845 cm^{-1} (signal from HAp and CH-bonds respectively). In both instances, the signal was collected from an area which included both HAp-tissue, a nerve bundle and an arteriole/blood vessel. These signals was later overlaid in order to easier compare what tissue gave the strongest signal of each type. In both instances, one could clearly see a stronger HAp-signal coming from the HAp-tissue, while a stronger CH-signal came from the nerve bundle and arteriole.

While not all the results obtained were as expected, and there still were some questions the remained unanswered, CARS was still able to image most of the samples used without any problems. With the technique also being able to differentiate between different types of tissues, and detect background signal if one knows where to look, CARS shows great promise as a future method for the analysis of bone and bone-like samples.

CHAPTER
SEVEN

FUTURE WORK

There is still work that could be done in order to improve the imaging of bone and bone-like samples using CARS. Firstly, the filter setup for the CARS signal in epi direction should be fixed. Then, the samples should be tested again, here with the focus of collecting an epi signal if possible. This should especially be done for the thicker samples, as well as for areas in the thinner samples where the bone tissue was denser (primarily compact bone).

Finding the exact source of the background signal detected when analysing the HAp-signal could also help us better understand how the CARS technique interacts with the samples, and perhaps also how to mitigate this background signal. It should also be looked into explaining the other discrepancies between the wavenumbner spectra and the Raman spectra that wasn't caused by this background signal.

If possible, the Raman spectrum for the embedding MMA should be collected, so that it can be compared with the other results collected. One should also see if the source of the weird Raman spectrum (obtained from the dog jaw sections) originally thought to be a background signal can be located. One should also see if it was possible to find the reason as to why the Raman signal collected around 2800-3000 cm^{-1} was so much larger than expected. This might again further help us understand how the CARS technique interacts with the samples, so that we can further improve upon it.

REFERENCES

[1] André Konarboland. “Understanding nanoscale processes in bone mineralisation to create breakthroughs in tissue engineering: Coherent Anti-Stokes Raman Scattering Microscopy (CARS) of calcium phosphate minerals”. Specialisation project (TFY4520). NTNU, 2023.

[2] Miriam Filippi et al. “Natural Polymeric Scaffolds in Bone Regeneration”. eng. In: *Frontiers in bioengineering and biotechnology* 8 (2020), pp. 474–474. ISSN: 2296-4185.

[3] Office of the Surgeon General (US). *Bone Health and Osteoporosis: A Report of the Surgeon General*. URL: https://www.ncbi.nlm.nih.gov/books/NBK45515/ (visited on Dec. 4, 2023).

[4] Wen-Feng Li et al. “Genetics of osteoporosis: accelerating pace in gene identification and validation”. eng. In: *Human genetics* 127.3 (2010), pp. 249–285. ISSN: 0340-6717.

[5] “High-power picosecond fiber source for coherent Raman microscopy”. eng. In: *Optics letters* 34.13 (2009), pp. 2051–2053. ISSN: 0146-9592.

[6] Eric O. Potma et al. “Real-time visualization of intracellular hydrodynamics in single living cells”. eng. In: *Proceedings of the National Academy of Sciences - PNAS* 98.4 (2001), pp. 1577–1582. ISSN: 0027-8424.

[7] T.U. Habibah, D.V. Amlani, and M. Brizuela. *Hydroxyapatite Dental Material*. Last updated: 2022-09-12. URL: https://www.ncbi.nlm.nih.gov/books/NBK513314/.

[8] Yujie Zhang and Lars Rehmmann. “Chapter 19 - Extraction of high-value compounds from marine biomass via ionic liquid-based techniques”. In: *Innovative and Emerging Technologies in the Bio-marine Food Sector*. Ed. by Marco Garcia-Vaquero and Gaurav Rajauria. Academic Press, 2022, pp. 417–439. ISBN: 978-0-12-820096-4. DOI: https://doi.org/10.1016/B978-0-12-820096-4.00002-X.

[9] Leslie P Gartner. *Textbook of histology*. eng. 4. ed, international ed. Philadelphia, Pennsylvania: Elsevier, 2017. ISBN: 9780323355636.

[10] Werner Schmidt. *Optical spectroscopy in chemistry and life sciences*. eng. Weinheim: Wiley-VCH, 2005. ISBN: 9783527299119.

[11] Jeanne L McHale. *Molecular spectroscopy*. eng. Upper Saddle River, N.J: Prentice Hall. ISBN: 0132290634.

[12] Halina Abramczyk. *Introduction to Laser Spectroscopy*. eng. 1st ed. San Diego: Elsevier Science, 2005. ISBN: 9780080455259.

[13] Douglas A. Skoog. *Principles of instrumental analysis*. eng. 6th ed., international student ed. Belmont, Calif: Thomson, 2007. ISBN: 9780495012016.

[14] David Harvey. "10.1: Overview of Spectroscopy". In: *Northeastern University*. LibreText Chemestry. URL: https://chem.libretexts.org/Courses/Northeastern_University/10%3A_Spectroscopic_Methods/10.1%3A_Overview_of_Spectroscopy (visited on May 4, 2024).

[15] Edmund Optics. *All About Diffraction Gratings*. URL: https://www.edmundoptics.com/knowledge-center/application-notes/optics/all-about-diffraction-gratings/ (visited on May 4, 2024).

[16] Edinburgh Instruments. *What is Raman Spectroscopy?* URL: https://www.edinst.com/blog/what-is-raman-spectroscopy/ (visited on Dec. 17, 2023).

[17] Pavan M.V. Raja and Andrew R. Barron. "4.3: Raman Spectroscopy". In: *Physical Methods in Chemistry and Nano Science*. Rice University. URL: https://chem.libretexts.org/Bookshelves/Analytical_Chemistry/Physical_Methods_in_Chemistry_and_Nano_Science_(Barron)/04%3A_Chemical_Speciation/4.03%3A_Raman_Spectroscopy (visited on Dec. 17, 2023).

[18] Richard Banks, Gaurav Sinha, and Charles Chu. "Introduction to Vibrations". In: *Vibrational Spectroscopy*. LibreText Chemistry. URL: https://chem.libretexts.org/Bookshelves/Physical_and_Theoretical_Chemistry_Textbook_Maps/Supplemental_Modules_(Physical_and_Theoretical_Chemistry)/Spectroscopy/Vibrational_Spectroscopy/Vibrational_Modes/Introduction_to_Vibrations (visited on Dec. 17, 2023).

[19] Kristin Kowolik. "Normal Modes". In: *Vibrational Spectroscopy*. LibreText Chemistry. URL: https://chem.libretexts.org/Bookshelves/Physical_and_Theoretical_Chemistry_Textbook_Maps/Supplemental_Modules_(Physical_and_Theoretical_Chemistry)/Spectroscopy/Vibrational_Spectroscopy/Vibrational_Modes/Normal_Modes (visited on Dec. 17, 2023).

[20] Michael Mansfield. *Understanding physics*. eng. Third edition. Chichester: Wiley, 2020. ISBN: 9781119519508.

[21] Samuel J. Ling, Jeff Sanny, and William Moebs. *University Physics Volume 3*. Houston, Texas: OpenStax, Sept. 2016. URL: https://openstax.org/books/university-physics-volume-3/pages/7-5-the-quantum-harmonic-oscillator.

[22] Peter Kelly. "5.3: The Harmonic Oscillator Approximates Molecular Vibrations". In: *Physical Chemistry (LibreTexts)*. LibreText Chemistry. URL: https://chem.libretexts.org/Bookshelves/Physical_and_Theoretical_Chemistry_Textbook_Maps/Physical_Chemistry_%28LibreTexts%29/05%3A_The_Harmonic_Oscillator_and_the_Rigid_Rotor/5.03%3A_The_Harmonic_Oscillator_Approximates_Vibrations (visited on Dec. 17, 2023).

[23] Hannah Toru Shay and Alexandra Holmes. "13.5: Vibrational Overtones". In: *Quantum Chemistry*. LibreText Chemistry. URL: `https://chem.libretexts.org/Courses/Pacific_Union_College/Quantum_Chemistry/13%3A_Molecular_Spectroscopy/13.05%3A_Vibrational_Overtones` (visited on Dec. 17, 2023).

[24] Seymour Blinder. "Harmonic Oscillator". In: *Quantum Mechanics*. LibreText Chemistry. URL: `https://chem.libretexts.org/Bookshelves/Physical_and_Theoretical_Chemistry_Textbook_Maps/Supplemental_Modules_(Physical_and_Theoretical_Chemistry)/Quantum_Mechanics/06._One_Dimensional_Harmonic_Oscillator/Harmonic_Oscillator` (visited on Dec. 17, 2023).

[25] Nathir Al-Rawashdeh. "Current Achievement and Future Potential of Fluorescence Spectroscopy". In: June 2012. ISBN: 978-953-51-0664-7. DOI: `10.5772/48034`.

[26] Thomas Wenzel. "5: Raman Spectroscopy". In: *Molecular and Atomic Spectroscopy*. Bates College. URL: `https://chem.libretexts.org/Bookshelves/Analytical_Chemistry/Molecular_and_Atomic_Spectroscopy_(Wenzel)/5%3A_Raman_Spectroscopy` (visited on Dec. 17, 2023).

[27] Eric C. Le Ru and Pablo G. Etchegoin. "Chapter 2 - Raman spectroscopy and related optical techniques". In: *Principles of Surface-Enhanced Raman Spectroscopy*. Ed. by Eric C. Le Ru and Pablo G. Etchegoin. Amsterdam: Elsevier, 2009, pp. 29–120. ISBN: 978-0-444-52779-0. DOI: `https://doi.org/10.1016/B978-0-444-52779-0.00008-8`. URL: `https://www.sciencedirect.com/science/article/pii/B9780444527790000088`.

[28] Anton Paar. *Basics of Raman spectroscopy*. URL: `https://wiki.anton-paar.com/en/basics-of-raman-spectroscopy/#c34004` (visited on May 3, 2024).

[29] Angus Unruh. "2.9: Raman spectroscopy". In: *CHEM1130 Principles in Chemistry I*. Northern Alberta Institute of Technology. URL: `https://chem.libretexts.org/Courses/Northern_Alberta_Institute_of_Technology/CHEM1130_Principles_in_Chemistry_I/2%3A_Quantum_Mechanical_Picture_of_the_Atom/2.09%3A_Raman_spectroscopy`.

[30] "Micro-Raman Spectroscopy of Nanostructures". eng. In: *Raman Spectroscopy for Nanomaterials Characterization*. Berlin, Heidelberg: Springer Berlin Heidelberg, pp. 417–444. ISBN: 3642206190.

[31] Raman For Life. *Glass Raman Spectrum*. URL: `https://ramanlife.com/library/glass-raman/` (visited on Oct. 12, 2023).

[32] S. Quillard et al. "Raman and Infrared Studies of Substituted β-TCP". In: *Key Engineering Materials* 493-494 (Oct. 2011), pp. 225–230. DOI: `10.4028/www.scientific.net/KEM.493-494.225`.

[33] Mohammad Alrefeai et al. "Application of β-Tricalcium Phosphate in Adhesive Dentin Bonding". In: *Polymers* 13 (Aug. 2021), p. 2855. DOI: `10.3390/polym13172855`.

[34] Peteh Mehdi Nkebiwe et al. “Detection of calcium phosphate species in soil by confocal µ-Raman spectroscopy”. eng. In: *Journal of plant nutrition and soil science* 185.2 (2022), pp. 221–231. ISSN: 1436-8730.

[35] Elmar Schmälzlin et al. “Raman imaging with a fiber-coupled multichannel spectrograph”. eng. In: *Sensors (Basel, Switzerland)* 14.11 (2014), pp. 21968–21980. ISSN: 1424-8220.

[36] K J Thomas et al. “Raman spectra of polymethyl methacrylate optical fibres excited by a 532 nm diode pumped solid state laser”. eng. In: *Journal of optics. A, Pure and applied optics* 10.5 (2008), p. 055303. ISSN: 1464-4258.

[37] Raman For Life. *Polymethyl Methacrylate Raman Spectrum*. URL: https://ramanlife.com/library/pmma/ (visited on May 27, 2024).

[38] Mas Rosemal et al. “FT-IR and FT-Raman Spectra and Normal Coordinate Analysis of Poly methyl methacrylate”. In: *Der Pharma Chemica* 2 (Jan. 2010).

[39] Jiayao Chen et al. “The Glass-Transition Temperature of Supported PMMA Thin Films with Hydrogen Bond/Plasmonic Interface”. In: *Polymers* 11 (Apr. 2019), p. 601. DOI: 10.3390/polym11040601.

[40] Frederick R. van de Voort, Jacqueline Sedman, and Ted Russin. “Lipid analysis by vibrational spectroscopy”. eng. In: *European journal of lipid science and technology* 103.12 (2001), pp. 815–826. ISSN: 1438-7697.

[41] Edinburgh Instruments. *What is Confocal Raman Microscopy?* URL: https://www.edinst.com/blog/what-is-confocal-raman-microscopy/ (visited on Dec. 17, 2023).

[42] MKS Newport. *Fundamentals of Spatial Filtering*. URL: https://www.newport.com/n/spatial-filters (visited on Dec. 17, 2023).

[43] A.W.S. Tarrant. “Chapter 28 - Optical Measurements”. In: *Instrumentation Reference Book (Fourth Edition)*. Ed. by Walt Boyes. Fourth Edition. Boston: Butterworth-Heinemann, 2010, pp. 499–519. ISBN: 978-0-7506-8308-1. DOI: https://doi.org/10.1016/B978-0-7506-8308-1.00028-0. URL: https://www.sciencedirect.com/science/article/pii/B9780750683081000280.

[44] Ji-Xin Cheng, Andreas Volkmer, and X. Sunney Xie. “Theoretical and experimental characterization of coherent anti-Stokes Raman scattering microscopy”. In: *J. Opt. Soc. Am. B* 19.6 (June 2002), pp. 1363–1375. DOI: 10.1364/JOSAB.19.001363. URL: https://opg.optica.org/josab/abstract.cfm?URI=josab-19-6-1363.

[45] Almar F Palonpon et al. “Raman and SERS microscopy for molecular imaging of live cells”. eng. In: *Nature protocols* 8.4 (2013), pp. 677–692. ISSN: 1754-2189.

[46] K.L.A. Chan and P.L.V. Fale. “8 - Label-free optical imaging of live cells”. In: *Biophotonics for Medical Applications*. Ed. by Igor Meglinski. Woodhead Publishing Series in Biomaterials. Woodhead Publishing, 2015, pp. 215–241. ISBN: 978-0-85709-662-3. DOI: https://doi.org/10.1016/B978-0-85709-662-3.00008-7.

[47] Christian W. Freudiger et al. “Label-Free Biomedical Imaging with High Sensitivity by Stimulated Raman Scattering Microscopy”. In: *Science* 322.5909 (2008), pp. 1857–1861. DOI: `10.1126/science.1165758`.

[48] Stefanie Degenhartt. *An Introduction to CARS Microscopy.* Nov. 4, 2011. URL: `https://www.leica-microsystems.com/science-lab/life-science/an-introduction-to-cars-microscopy/`.

[49] Conor L. Evans et al. “Chemical Imaging of Tissue in Vivo with Video-Rate Coherent Anti-Stokes Raman Scattering Microscopy”. eng. In: *Proceedings of the National Academy of Sciences - PNAS* 102.46 (2005), pp. 16807–16812. ISSN: 0027-8424.

[50] Shaowei Li et al. “Coherent Anti-Stokes Raman Scattering Microscopy and Its Applications”. eng. In: *Frontiers in physics* 8 (2020). ISSN: 2296-424X.

[51] Jennifer P. Ogilvie et al. “Time-delayed coherent Raman spectroscopy”. eng. In: *Molecular physics* 106.2-4 (2008), pp. 587–594. ISSN: 0026-8976.

[52] Edward Gurr. *Synthetic dyes in biology, medicine and chemistry.* eng. London, 1971.

[53] Holde Puchtler, Susan N. Meloan, and Mary S. Terry. “ON THE HISTORY AND MECHANISM OF ALIZARIN AND ALIZARIN RED S STAINS FOR CALCIUM”. In: *Journal of Histochemistry & Cytochemistry* 17.2 (1969). PMID: 4179464, pp. 110–124. DOI: `10.1177/17.2.110`.

[54] Aline Bernar et al. “Optimization of the Alizarin Red S Assay by Enhancing Mineralization of Osteoblasts”. eng. In: *International journal of molecular sciences* 24.1 (2022), p. 723. ISSN: 1422-0067.

[55] Carl A Gregory et al. “An Alizarin red-based assay of mineralization by adherent cells in culture: comparison with cetylpyridinium chloride extraction”. eng. In: *Analytical biochemistry* 329.1 (2004), pp. 77–84. ISSN: 0003-2697.

[56] Pascal Rauthe et al. “Excited State Dynamics of Alizarin Red S Nanoparticles in Solution”. eng. In: *Molecules (Basel, Switzerland)* 28.15 (2023), p. 5633. ISSN: 1420-3049.

[57] Olivier Thomas and Marine Brogat. “Chapter 4 - Organic constituents”. In: *UV-Visible Spectrophotometry of Waters and Soils.* Ed. by Olivier Thomas and Christopher Burgess. Third edition. Elsevier, 2022, pp. 95–160. ISBN: 978-0-323-90994-5.

[58] J. Gordon Betts et al. *Anatomy and Physiology.* 2e. Houston, Texas: OpenStax, 2022. URL: `https://openstax.org/books/anatomy-and-physiology-2e/pages/6-3-bone-structure`.

[59] Alizae Marny Mohamed. “An Overview of Bone Cells and their Regulating Factors of Differentiation”. eng. In: *The Malaysian journal of medical sciences* 15.1 (2008), pp. 4–12.

[60] Xu Feng. “Chemical and Biochemical Basis of Cell-Bone Matrix Interaction in Health and Disease”. In: *Current chemical biology* 3 (May 2009), pp. 189–196. URL: `https://www.ncbi.nlm.nih.gov/pmc/articles/PMC2790195/`.

[61] J. Casale and J. S. Crane. *Biochemistry, Glycosaminoglycans*. Last updated: 2023-03-27. URL: `https://pubmed.ncbi.nlm.nih.gov/31335015/`.

[62] M. Peckham. *Extracellular Matrix - 'Ground substance'*. URL: `https://www.histology.leeds.ac.uk/tissue_types/connective/connective_groundS.php` (visited on Apr. 16, 2024).

[63] Jinyan Si et al. "Osteopontin in Bone Metabolism and Bone Diseases". eng. In: *Medical science monitor* 26 (2020), e919159–e919159. ISSN: 1234-1010.

[64] Masaki Noda and David T. Denhardt. "Chapter 18 - Osteopontin". In: *Principles of Bone Biology (Third Edition)*. Ed. by John P. Bilezikian, Lawrence G. Raisz, and T. John Martin. Third Edition. San Diego: Academic Press, 2008, pp. 351–366. ISBN: 978-0-12-373884-4. DOI: `https://doi.org/10.1016/B978-0-12-373884-4.00037-9`. URL: `https://www.sciencedirect.com/science/article/pii/B9780123738844000379`.

[65] Sawittree Rujitanapanich, Pitoon Kumpapan, and Panthong Wanjanoi. "Synthesis of Hydroxyapatite from Oyster Shell via Precipitation". eng. In: *Energy procedia* 56 (2014), pp. 112–117. ISSN: 1876-6102.

[66] Eric M. Rivera-Muñoz. "Hydroxyapatite-Based Materials: Synthesis and Characterization". In: *Biomedical Engineering*. Ed. by Reza Fazel-Rezai. Rijeka: IntechOpen, 2011. Chap. 4. DOI: `10.5772/19123`. URL: `https://doi.org/10.5772/19123`.

[67] H. Ou-Yang et al. "Infrared Microscopic Imaging of Bone: Spatial Distribution of CO32". eng. In: *Journal of bone and mineral research* 16.5 (2001), pp. 893–900. ISSN: 0884-0431.

[68] E. Landi et al. "Carbonated hydroxyapatite as bone substitute". eng. In: *Journal of the European Ceramic Society* 23.15 (2003), pp. 2931–2937. ISSN: 0955-2219.

[69] Stanislas Von Euw et al. "Bone mineral: new insights into its chemical composition". eng. In: *Scientific reports* 9.1 (2019), pp. 8456–8456. ISSN: 2045-2322.

[70] H Clarke Anderson. "Matrix vesicles and calcification". eng. In: *Current rheumatology reports* 5.3 (2003), pp. 222–226. ISSN: 1523-3774.

[71] Suwimon Boonrungsiman et al. "The role of intracellular calcium phosphate in osteoblast-mediated bone apatite formation". eng. In: *Proceedings of the National Academy of Sciences - PNAS* 109.35 (2012), pp. 14170–14175.

[72] Rinaldo Florencio-Silva et al. "Biology of Bone Tissue: Structure, Function, and Factors That Influence Bone Cells". eng. In: *BioMed research international* 2015 (2015), pp. 421746–17. ISSN: 2314-6133.

[73] NCI Dictionaries. *bone marrow*. URL: `https://www.cancer.gov/publications/dictionaries/cancer-terms/def/bone-marrow` (visited on Apr. 23, 2024).

[74] Tomasz Buchwald et al. "Identifying compositional and structural changes in spongy and subchondral bone from the hip joints of patients with osteoarthritis using Raman spectroscopy". In: *Journal of biomedical optics* 17.1 (Jan. 2012), p. 017007. ISSN: 1083-3668. DOI: `10.1117/1.JBO.17.1.017007`.

[75] G. Penel et al. “Composition of bone and apatitic biomaterials as revealed by intravital Raman microspectroscopy”. eng. In: *Bone (New York, N.Y.)* 36.5 (2005), pp. 893–901.

[76] Bruce G. Frushour and Jack L. Koenig. “Raman scattering of collagen, gelatin, and elastin”. In: *Biopolymers* 14.2 (1975), pp. 379–391. DOI: https://doi.org/10.1002/bip.1975.360140211.

[77] Manon Fraulob et al. “Multimodal characterization of the bone-implant interface using Raman spectroscopy and nanoindentation”. eng. In: *Medical engineering & physics* 84 (2020), pp. 60–67. ISSN: 1350-4533.

[78] Mohamed Khalid et al. “Raman Spectroscopy detects changes in Bone Mineral Quality and Collagen Cross-linkage in Staphylococcus Infected Human Bone”. eng. In: *Scientific reports* 8.1 (2018), pp. 9417–9. ISSN: 2045-2322.

[79] Jerilyn A. Timlin, Angela Carden, and Michael D. Morris. “Chemical Microstructure of Cortical Bone Probed by Raman Transects”. In: *Applied Spectroscopy* 53.11 (1999), pp. 1429–1435. DOI: https://doi.org/10.1366/0003702991945786.

[80] O de Carmejane et al. “Bone chemical structure response to mechanical stress studied by high pressure Raman spectroscopy”. eng. In: *Calcified tissue international* 76.3 (2005), pp. 207–213. ISSN: 0171-967X.

[81] Takeo Minamikawa, Yoshinori Harada, and Tetsuro Takamatsu. “Ex vivo peripheral nerve detection of rats by spontaneous Raman spectroscopy”. eng. In: *Scientific reports* 5.1 (2015), pp. 17165–17165. ISSN: 2045-2322.

[82] Besim Ben-Nissan. *Advances in Calcium Phosphate Biomaterials*. eng. 2014th ed. Vol. 2. Springer Series in Biomaterials Science and Engineering. Berlin, Heidelberg: Springer Berlin / Heidelberg, 2014. ISBN: 3642539793.

[83] Minh Khai Le Thieu et al. “Immunohistochemical comparison of lateral bone augmentation using a synthetic TiO2 block or a xenogeneic graft in chronic alveolar defects”. eng ; nor. In: *Clinical implant dentistry and related research* 25.1 (2023), pp. 57–67. ISSN: 1523-0899.

[84] Oscar Villa et al. “Proline-Rich Peptide Mimics Effects of Enamel Matrix Derivative on Rat Oral Mucosa Incisional Wound Healing”. eng. In: *Journal of periodontology (1970)* 86.12 (2015), pp. 1386–1395. ISSN: 0022-3492.

[85] Dimitri Boiroux et al. “Pixel timing correction in time-lapsed calcium imaging using point scanning microscopy”. eng. In: *Journal of neuroscience methods* 237 (2014), pp. 60–68. ISSN: 0165-0270.

APPENDICES

A - FULL SPECTRES

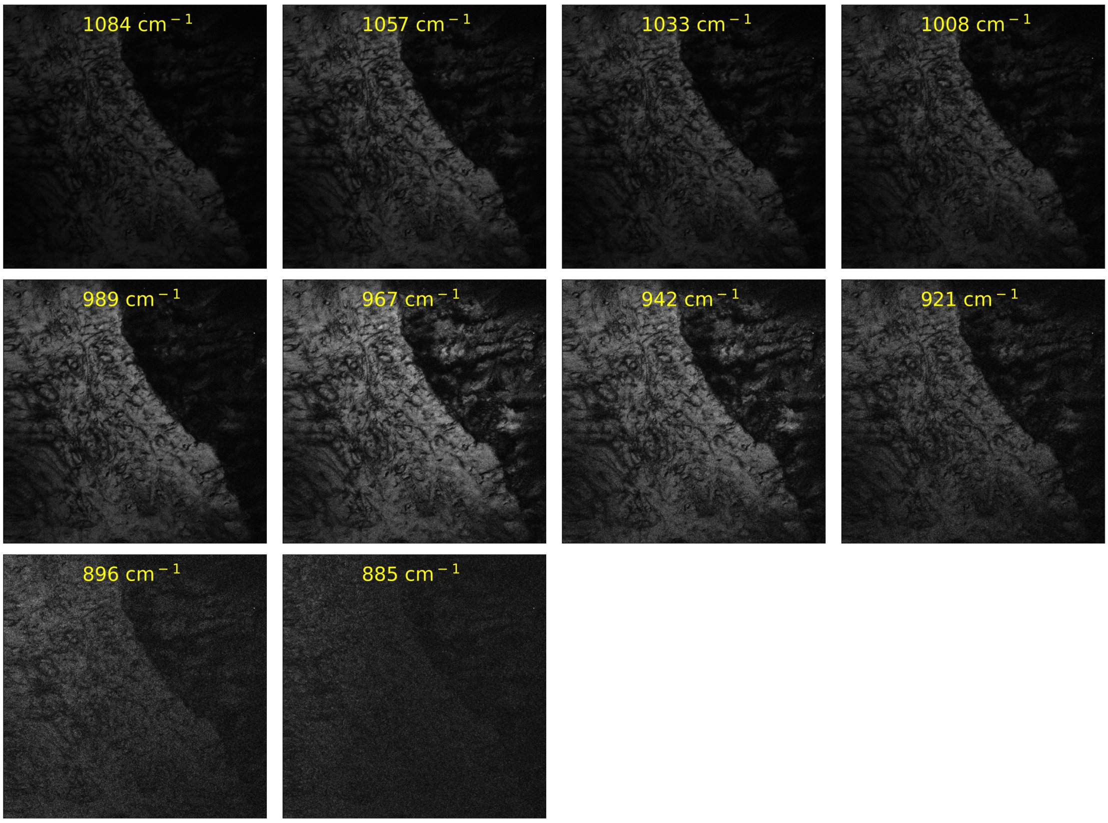

Figure A.0.1: All images captured in order to create the spectrum seen in Figure 4.4.5. Aspect ratio 320×320 µm.

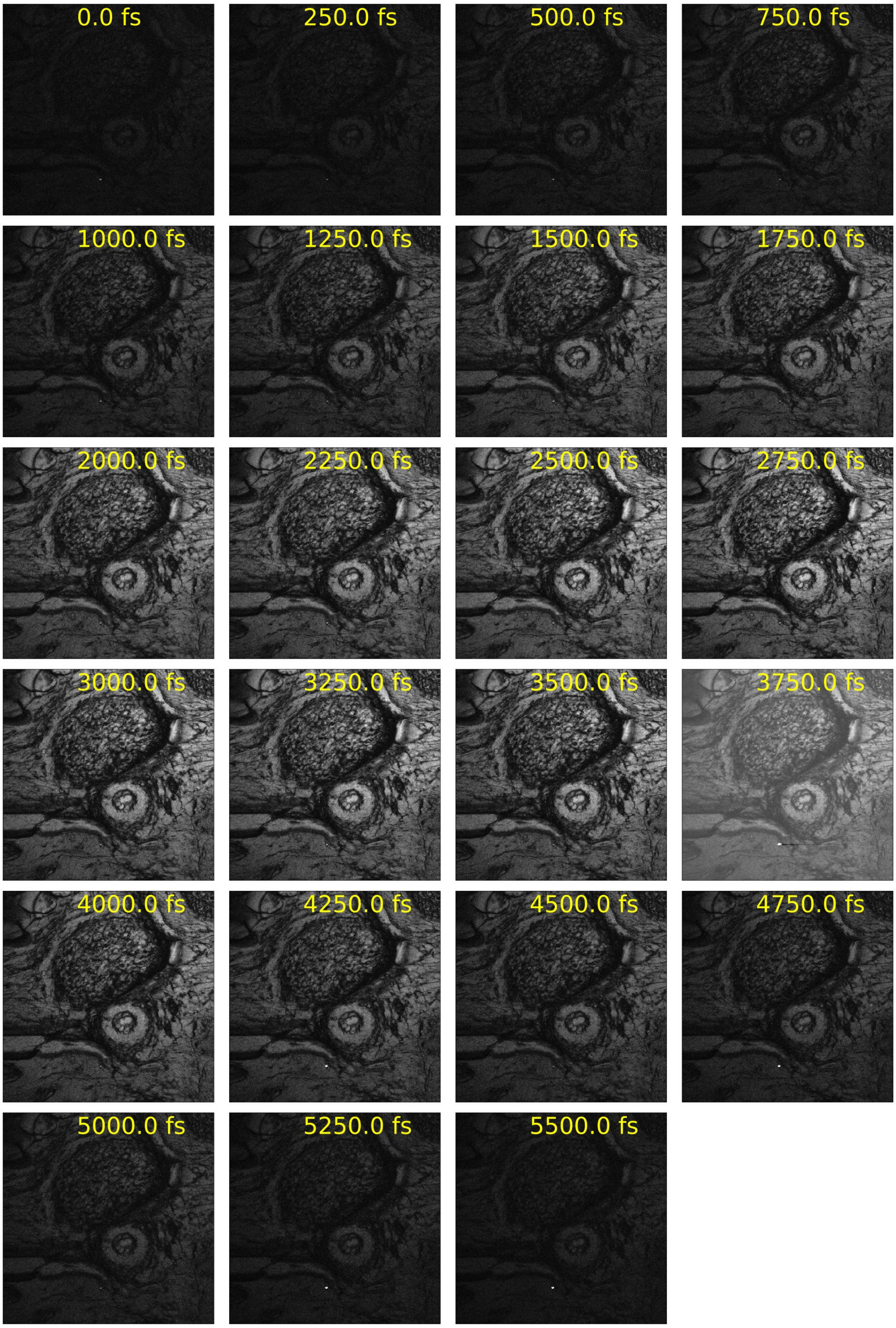

Figure A.0.2: All images captured in order to create the spectrum seen in Figure 4.4.4. Aspect ratio 320×320 µm

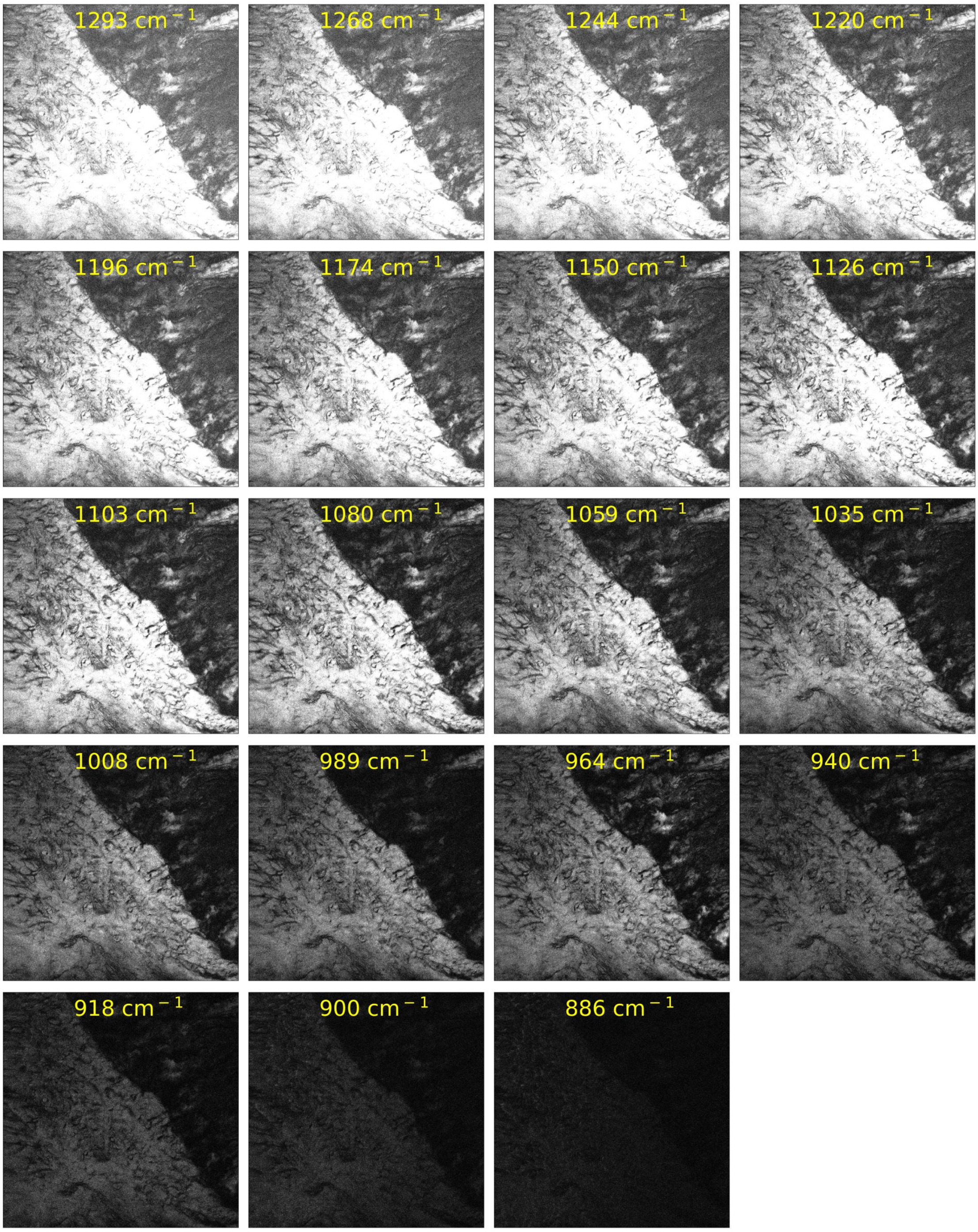

Figure A.0.3: All images captured in order to create the spectrum seen in Figure 4.4.6. Aspect ratio 320×320 µm

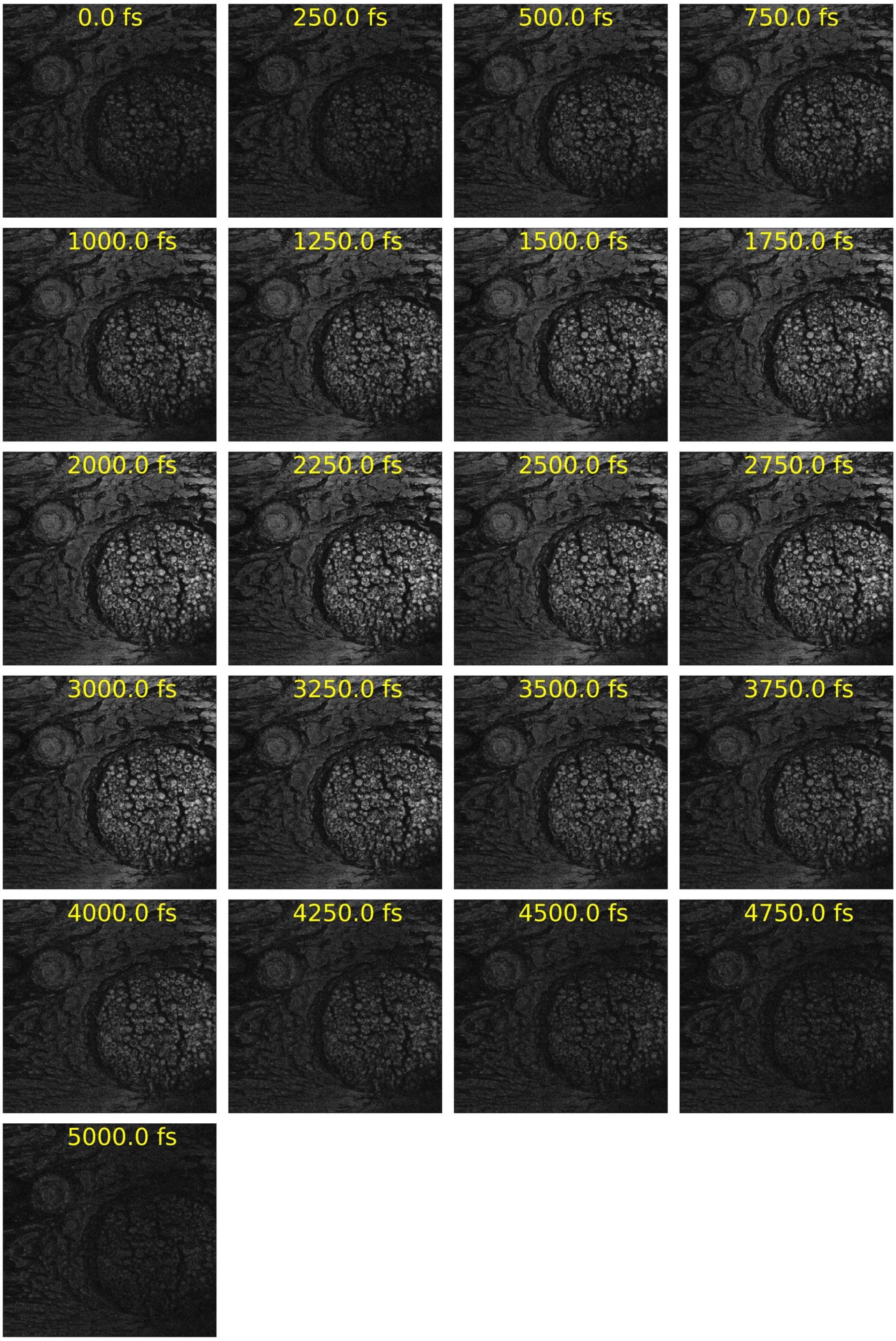

Figure A.0.4: All images captured in order to create the spectrum seen in Figure 4.4.10. Aspect ratio 320×320 µm

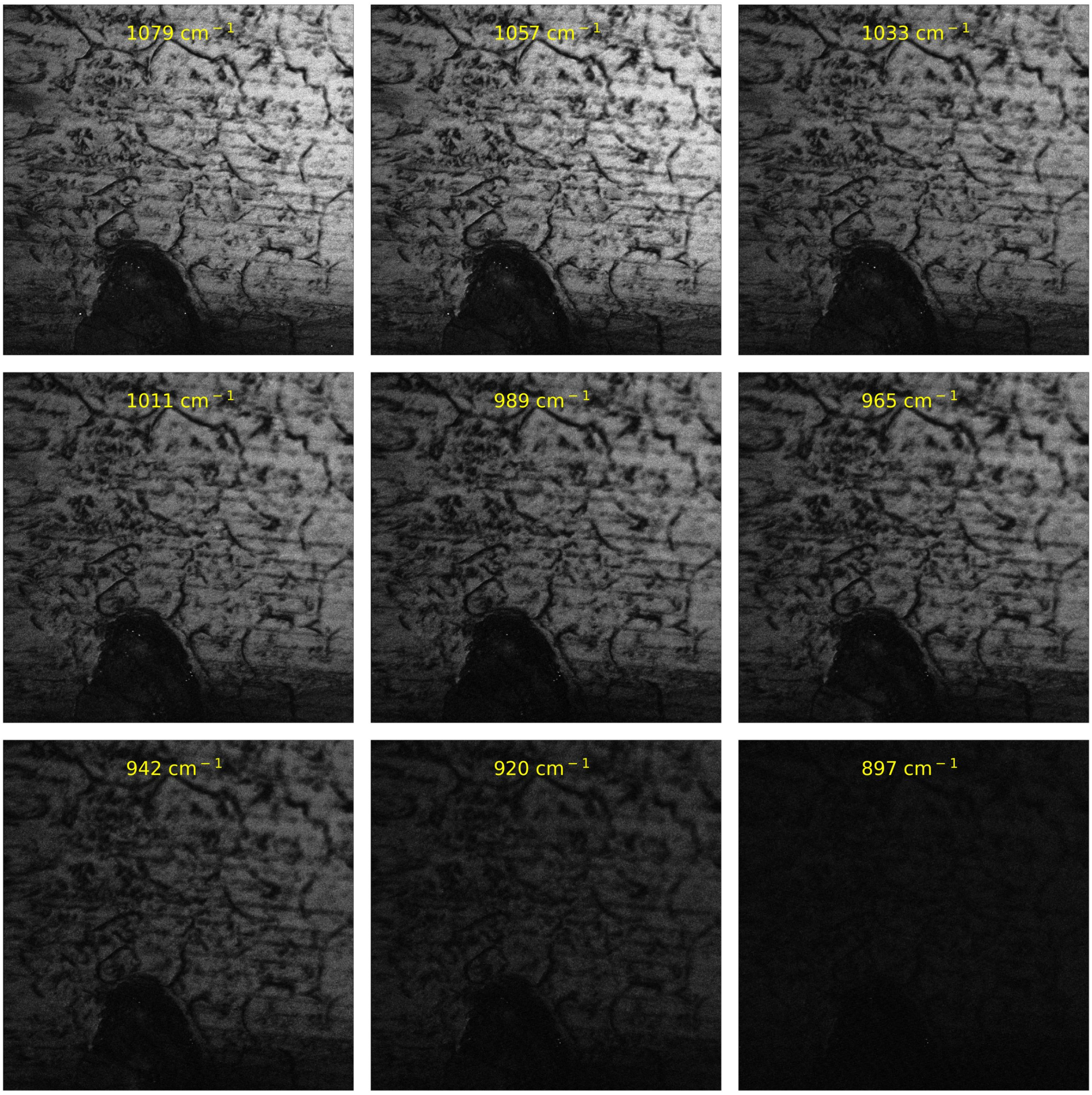

Figure A.0.5: All images captured in order to create the spectrum seen in Figure 4.4.13. Aspect ratio 320×320 µm.

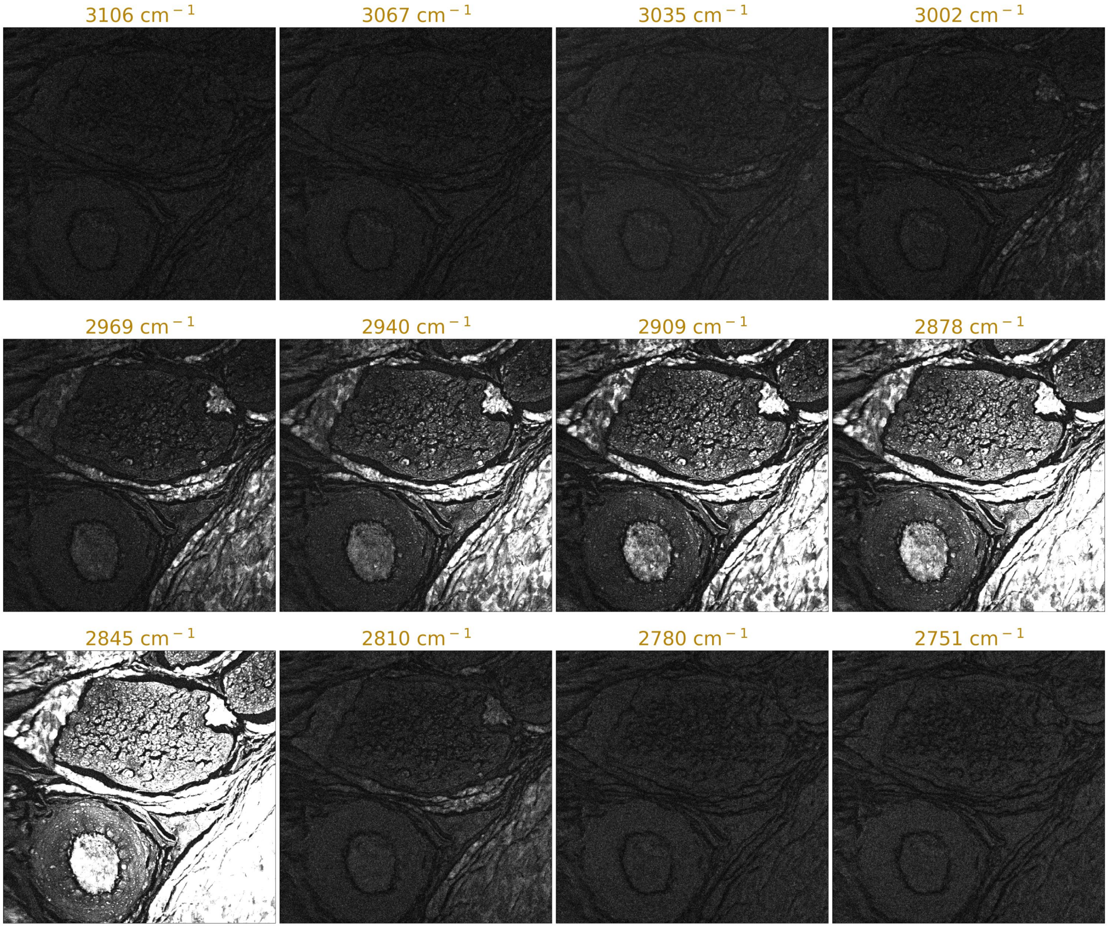

Figure A.0.6: All images captured in order to create the spectrum seen in Figure 4.4.16a. Aspect ratio 320×320 µm.

Figure A.0.7: All images captured in order to create the spectrum seen in Figure 4.4.16b. Aspect ratio 320×320 µm.

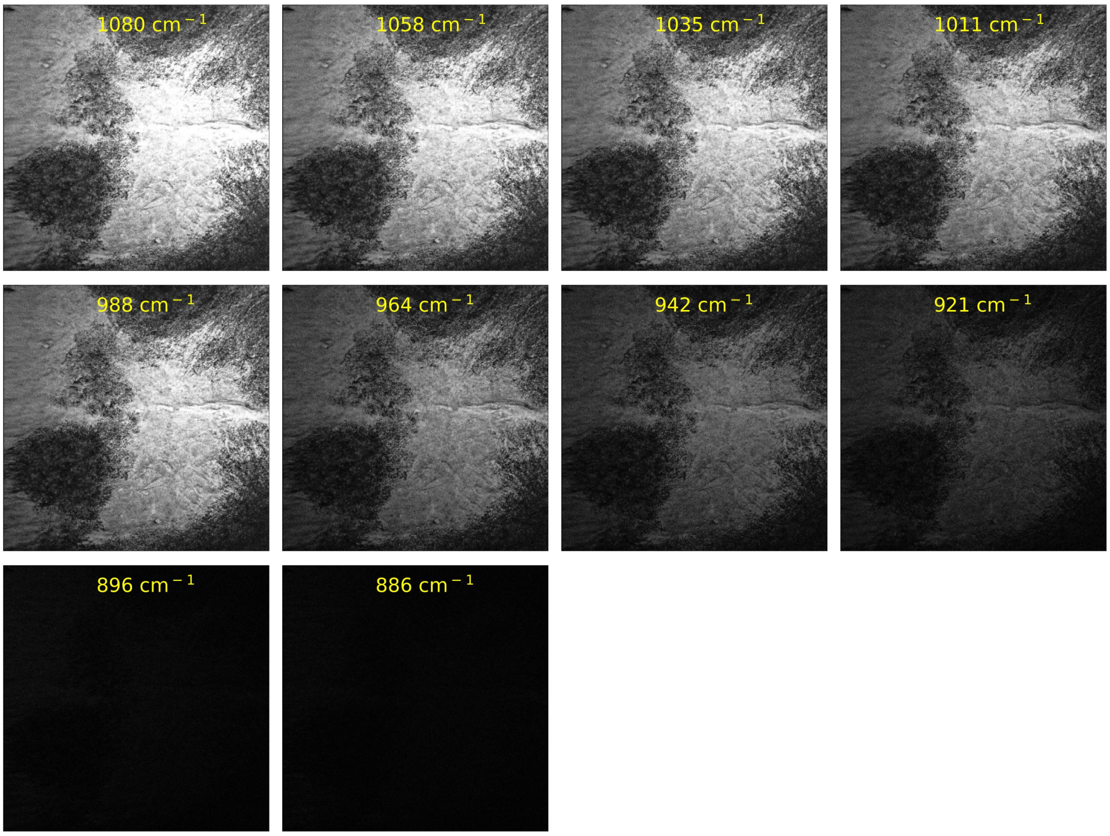

Figure A.0.8: All images captured in order to create the spectrum seen in Figure 4.4.28a. Aspect ratio 320×320 µm.

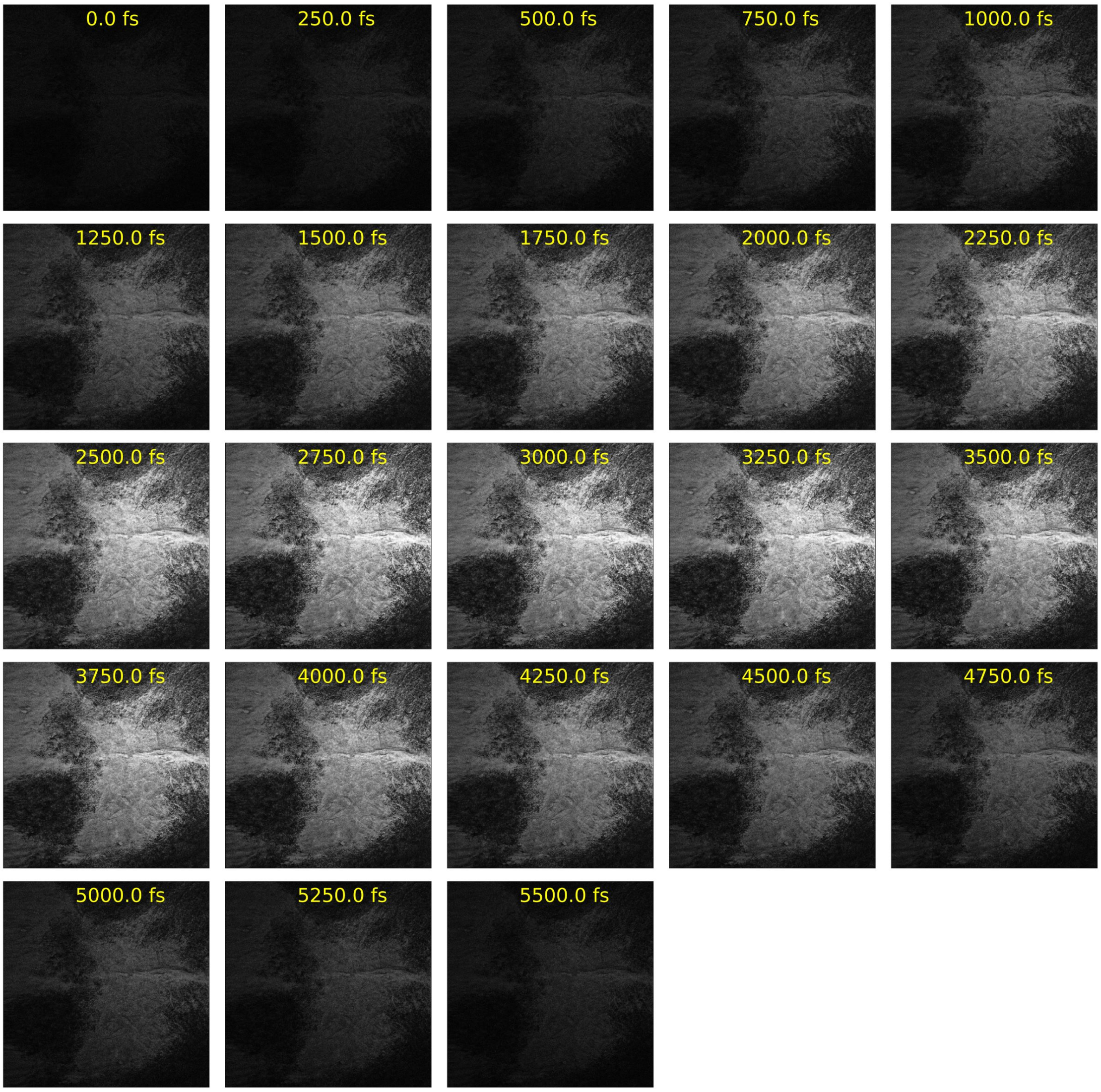

Figure A.0.9: All images captured in order to create the spectrum seen in Figure 4.4.28b. Aspect ratio 320×320 µm.

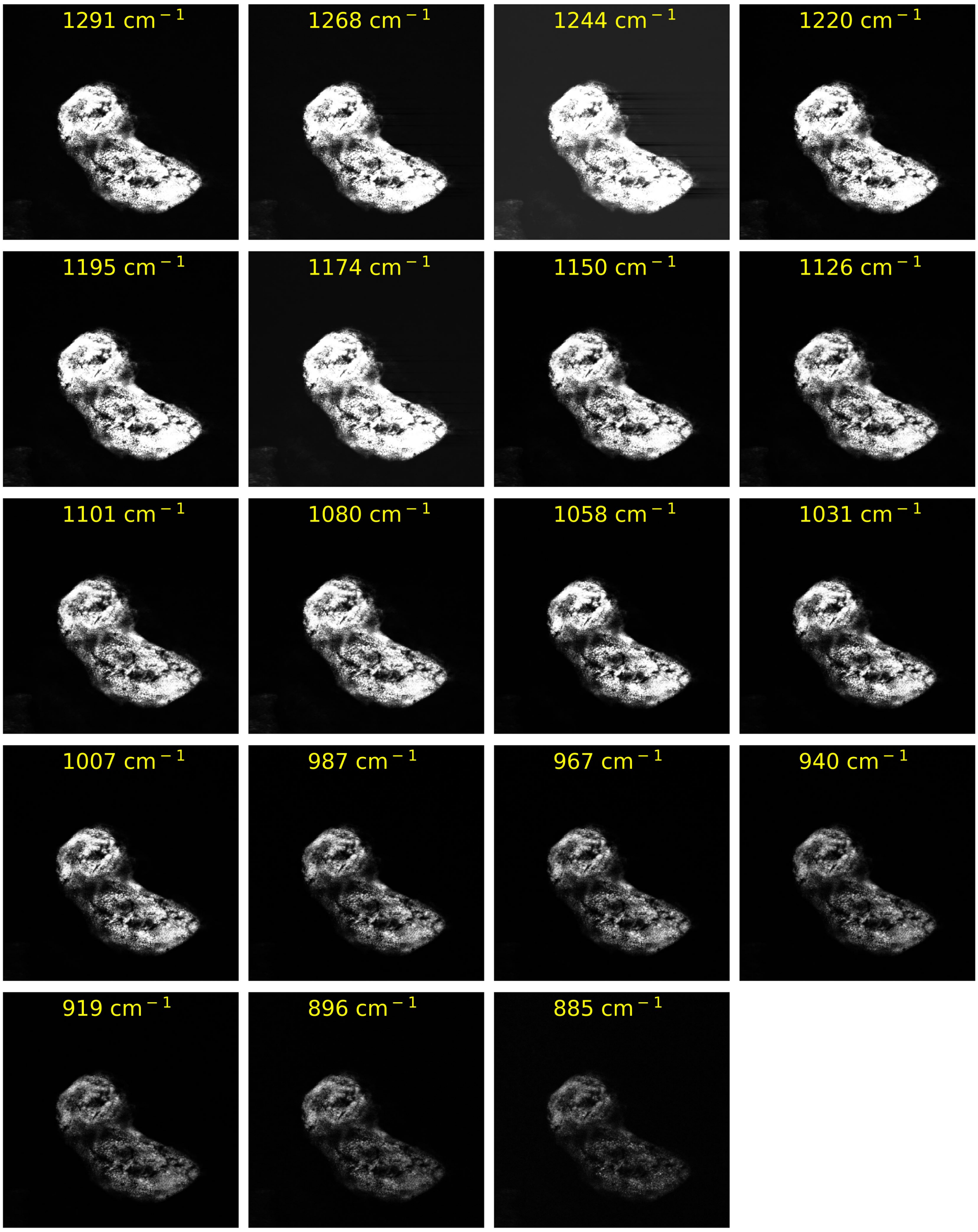

Figure A.0.10: All images captured in order to create the spectrum seen in Figure 4.4.30. Aspect ratio 320×320 µm.

B - SOME CALCULATIONS

Here, how to arrive at Equation 2.17 from Equation 2.16 is shown.

$$\hbar = \frac{h}{2\pi}$$

$$\frac{\omega c}{\lambda} = \hbar w$$

$$\longrightarrow \omega = \frac{2\pi c}{\lambda}$$

$$\omega_{CARS} = 2\omega_{pump} - \omega_{stokes}$$

$$\longrightarrow \frac{2\pi c}{\lambda_{CARS}} = \frac{4\pi c}{\lambda_{pump}} - \frac{2\pi c}{\lambda_{Stokes}}$$

$$\longrightarrow \frac{1}{\lambda_{CARS}} = \frac{2}{\lambda_{pump}} - \frac{1}{\lambda_{Stokes}}$$

$$\longrightarrow \lambda_{CARS} = \frac{1}{\frac{2}{\lambda_{pump}} - \frac{1}{\lambda_{stokes}}}$$

C - IMAGE LICENSE

CCC | Marketplace

This is a License Agreement between André Konarboland ("User") and Copyright Clearance Center, Inc. ("CCC") on behalf of the Rightsholder identified in the order details below. The license consists of the order details, the Marketplace Permissions General Terms and Conditions below, and any Rightsholder Terms and Conditions which are included below.

All payments must be made in full to CCC in accordance with the Marketplace Permissions General Terms and Conditions below.

Order Date	07-May-2024	**Type of Use**	Republish in a thesis/dissertation
Order License ID	1481280-1	**Publisher**	SPIE; S P I E (INTL SOC FOR OPTICAL)
ISSN	1083-3668	**Portion**	Image/photo/illustration

LICENSED CONTENT

Publication Title	Journal of Biomedical Optics	**Rightsholder**	SPIE
Article Title	Identifying compositional and structural changes in spongy and subchondral bone from the hip joints of patients with osteoarthritis using Raman spectroscopy.	**Publication Type**	Journal
		Start Page	017007
		Issue	1
Author/Editor	Society of Photo-optical Instrumentation Engineers., International Biomedical Optics Society.	**Volume**	17
		URL	https://www.spiedigitallibrary.org/journal...
Date	01/01/1996		
Language	English		
Country	United States of America		

REQUEST DETAILS

Portion Type	Image/photo/illustration	**Distribution**	Worldwide
Number of Images / Photos / Illustrations	1	**Translation**	Original language of publication
Format (select all that apply)	Electronic	**Copies for the Disabled?**	No
Who Will Republish the Content?	Academic institution	**Minor Editing Privileges?**	Yes
Duration of Use	Life of current edition	**Incidental Promotional Use?**	No
Lifetime Unit Quantity	Up to 499	**Currency**	EUR
Rights Requested	Main product		

NEW WORK DETAILS

Title	Coherent Anti-Stokes Raman Scattering Microscopy (CARS) of calcium phosphate minerals and bone samples	**Institution Name**	NTNU
		Expected Presentation Date	2024-06-10
Instructor Name	Pawel Sikorski		

ADDITIONAL DETAILS

The Requesting Person / Organization to Appear on the License	André Konarboland

REQUESTED CONTENT DETAILS

Title, Description or Numeric Reference of the Portion(s)	Figure 3	**Title of the Article / Chapter the Portion Is From**	Identifying compositional and structural changes in spongy and subchondral bone from the hip joints of patients with osteoarthritis using Raman spectroscopy.
Editor of Portion(s)	Buchwald, Tomasz; Niciejewski, Krzysztof; Kozielski, Marek; Szybowicz, Mirosław; Siatkowski, Marcin; Krauss, Hanna	**Author of Portion(s)**	Buchwald, Tomasz; Niciejewski, Krzysztof; Kozielski, Marek; Szybowicz, Mirosław; Siatkowski, Marcin; Krauss, Hanna
Volume / Edition	17		
Page or Page Range of Portion	017007	**Publication Date of Portion**	2012-01-01

Marketplace Permissions General Terms and Conditions

The following terms and conditions ("General Terms"), together with any applicable Publisher Terms and Conditions, govern User's use of Works pursuant to the Licenses granted by Copyright Clearance Center, Inc. ("CCC") on behalf of the applicable Rightsholders of such Works through CCC's applicable Marketplace transactional licensing services (each, a "Service").

1) **Definitions.** For purposes of these General Terms, the following definitions apply:

"License" is the licensed use the User obtains via the Marketplace platform in a particular licensing transaction, as set forth in the Order Confirmation.

"Order Confirmation" is the confirmation CCC provides to the User at the conclusion of each Marketplace transaction. "Order Confirmation Terms" are additional terms set forth on specific Order Confirmations not set forth in the General Terms that can include terms applicable to a particular CCC transactional licensing service and/or any Rightsholder-specific terms.

"Rightsholder(s)" are the holders of copyright rights in the Works for which a User obtains licenses via the Marketplace platform, which are displayed on specific Order Confirmations.

"Terms" means the terms and conditions set forth in these General Terms and any additional Order Confirmation Terms collectively.

"User" or "you" is the person or entity making the use granted under the relevant License. Where the person accepting the Terms on behalf of a User is a freelancer or other third party who the User authorized to accept the General Terms on the User's behalf, such person shall be deemed jointly a User for purposes of such Terms.

"Work(s)" are the copyright protected works described in relevant Order Confirmations.

2) **Description of Service.** CCC's Marketplace enables Users to obtain Licenses to use one or more Works in accordance with all relevant Terms. CCC grants Licenses as an agent on behalf of the copyright rightsholder identified in the relevant Order Confirmation.

3) **Applicability of Terms.** The Terms govern User's use of Works in connection with the relevant License. In the event of any conflict between General Terms and Order Confirmation Terms, the latter shall govern. User acknowledges that Rightsholders have complete discretion whether to grant any permission, and whether to place any limitations on any grant, and that CCC has no right to supersede or to modify any such discretionary act by a Rightsholder.

4) **Representations; Acceptance.** By using the Service, User represents and warrants that User has been duly authorized by the User to accept, and hereby does accept, all Terms.

6) **General Payment Terms.** User may pay at time of checkout by credit card or choose to be invoiced. If the User chooses to be invoiced, the User shall: (i) remit payments in the manner identified on specific invoices, (ii) unless otherwise specifically stated in an Order Confirmation or separate written agreement, Users shall remit payments upon receipt of the relevant invoice from CCC, either by delivery or notification of availability of the invoice via the Marketplace platform, and (iii) if the User does not pay the invoice within 30 days of receipt, the User may incur a service charge of 1.5% per month or the maximum rate allowed by applicable law, whichever is less. While User may exercise the rights in the License immediately upon receiving the Order Confirmation, the License is automatically revoked and is null and void, as if it had never been issued, if CCC does not receive complete payment on a timely basis.

7) **General Limits on Use.** Unless otherwise provided in the Order Confirmation, any grant of rights to User (i) involves only the rights set forth in the Terms and does not include subsequent or additional uses, (ii) is non-exclusive and non-transferable, and (iii) is subject to any and all limitations and restrictions (such as, but not limited to, limitations on duration of use or circulation) included in the Terms. Upon completion of the licensed use as set forth in the Order Confirmation, User shall either secure a new permission for further use of the Work(s) or immediately cease any new use of the Work(s) and shall render inaccessible (such as by deleting or by removing or severing links or other locators) any further copies of the Work. User may only make alterations to the Work if and as expressly set forth in the Order Confirmation. No Work may be used in any way that is unlawful, including without limitation if such use would violate applicable sanctions laws or regulations, would be defamatory, violate the rights of third parties (including such third parties' rights of copyright, privacy, publicity, or other tangible or intangible property), or is otherwise illegal, sexually explicit, or obscene. In addition, User may not conjoin a Work with any other material that may result in damage to the reputation of the Rightsholder. Any unlawful use will render any licenses hereunder null and void. User agrees to inform CCC if it becomes aware of any infringement of any rights in a Work and to cooperate with any reasonable request of CCC or the Rightsholder in connection therewith.

8) **Third Party Materials.** In the event that the material for which a License is sought includes third party materials (such as photographs, illustrations, graphs, inserts and similar materials) that are identified in such material as having been used by permission (or a similar indicator), User is responsible for identifying, and seeking separate licenses (under this Service, if available, or otherwise) for any of such third party materials; without a separate license, User may not use such third party materials via the License.

9) **Copyright Notice.** Use of proper copyright notice for a Work is required as a condition of any License granted under the Service. Unless otherwise provided in the Order Confirmation, a proper copyright notice will read substantially as follows: "Used with permission of [Rightsholder's name], from [Work's title, author, volume, edition number and year of copyright]; permission conveyed through Copyright Clearance Center, Inc." Such notice must be provided in a reasonably legible font size and must be placed either on a cover page or in another location that any person, upon gaining access to the material which is the subject of a permission, shall see, or in the case of republication Licenses, immediately adjacent to the Work as used (for example, as part of a by-line or footnote) or in the place where substantially all other credits or notices for the new work containing the republished Work are located. Failure to include the required notice results in loss to the Rightsholder and CCC, and the User shall be liable to pay liquidated damages for each such failure equal to twice the use fee specified in the Order Confirmation, in addition to the use fee itself and any other fees and charges specified.

10) **Indemnity.** User hereby indemnifies and agrees to defend the Rightsholder and CCC, and their respective employees and directors, against all claims, liability, damages, costs, and expenses, including legal fees and expenses, arising out of any use of a Work beyond the scope of the rights granted herein and in the Order Confirmation, or any use of a Work which has been altered in any unauthorized way by User, including claims of defamation or infringement of rights of copyright, publicity, privacy, or other tangible or intangible property.

11) **Limitation of Liability.** UNDER NO CIRCUMSTANCES WILL CCC OR THE RIGHTSHOLDER BE LIABLE FOR ANY DIRECT, INDIRECT, CONSEQUENTIAL, OR INCIDENTAL DAMAGES (INCLUDING WITHOUT LIMITATION DAMAGES FOR LOSS OF BUSINESS PROFITS OR INFORMATION, OR FOR BUSINESS INTERRUPTION) ARISING OUT OF THE USE OR INABILITY TO USE A WORK, EVEN IF ONE OR BOTH OF THEM HAS BEEN ADVISED OF THE POSSIBILITY OF SUCH DAMAGES. In any event, the total liability of the Rightsholder and CCC (including their respective employees and directors) shall not exceed the total amount actually paid by User for the relevant License. User assumes full liability for the actions and omissions of its principals, employees, agents, affiliates, successors, and assigns.

12) **Limited Warranties.** THE WORK(S) AND RIGHT(S) ARE PROVIDED "AS IS." CCC HAS THE RIGHT TO GRANT TO USER THE RIGHTS GRANTED IN THE ORDER CONFIRMATION DOCUMENT. CCC AND THE RIGHTSHOLDER DISCLAIM ALL OTHER WARRANTIES RELATING TO THE WORK(S) AND RIGHT(S), EITHER EXPRESS OR IMPLIED, INCLUDING WITHOUT LIMITATION IMPLIED WARRANTIES OF MERCHANTABILITY OR FITNESS FOR A PARTICULAR PURPOSE. ADDITIONAL RIGHTS MAY BE REQUIRED TO USE ILLUSTRATIONS, GRAPHS, PHOTOGRAPHS, ABSTRACTS, INSERTS, OR OTHER PORTIONS OF THE WORK (AS OPPOSED TO THE ENTIRE WORK) IN A MANNER CONTEMPLATED BY USER; USER UNDERSTANDS AND AGREES THAT NEITHER CCC NOR THE RIGHTSHOLDER MAY HAVE SUCH ADDITIONAL RIGHTS TO GRANT.

13) **Effect of Breach.** Any failure by User to pay any amount when due, or any use by User of a Work beyond the scope of the License set forth in the Order Confirmation and/or the Terms, shall be a material breach of such License. Any breach not cured within 10 days of written notice thereof shall result in immediate termination of such License without further notice. Any unauthorized (but licensable) use of a Work that is terminated immediately upon notice thereof may be liquidated by payment of the Rightsholder's ordinary license price therefor; any unauthorized (and unlicensable) use that is not terminated immediately for any reason (including, for example, because materials containing the Work cannot reasonably be recalled) will be subject to all remedies available at law or in equity, but in no event to a payment of less than three times the Rightsholder's ordinary license price for the most closely analogous licensable use plus Rightsholder's and/or CCC's costs and expenses incurred in collecting such payment.

14) **Additional Terms for Specific Products and Services.** If a User is making one of the uses described in this Section 14, the additional terms and conditions apply:

a) ***Print Uses of Academic Course Content and Materials (photocopies for academic coursepacks or classroom handouts).*** For photocopies for academic coursepacks or classroom handouts the following additional terms apply:

i) The copies and anthologies created under this License may be made and assembled by faculty members individually or at their request by on-campus bookstores or copy centers, or by off-campus copy shops and other similar entities.

ii) No License granted shall in any way: (i) include any right by User to create a substantively non-identical copy of the Work or to edit or in any other way modify the Work (except by means of deleting material immediately preceding or following the entire portion of the Work copied) (ii) permit "publishing ventures" where any particular anthology would be systematically marketed at multiple institutions.

iii) Subject to any Publisher Terms (and notwithstanding any apparent contradiction in the Order Confirmation arising from data provided by User), any use authorized under the academic pay-per-use service is limited as follows:

A) any License granted shall apply to only one class (bearing a unique identifier as assigned by the institution, and thereby including all sections or other subparts of the class) at one institution;

B) use is limited to not more than 25% of the text of a book or of the items in a published collection of essays, poems or articles;

C) use is limited to no more than the greater of (a) 25% of the text of an issue of a journal or other periodical or (b) two articles from such an issue;

D) no User may sell or distribute any particular anthology, whether photocopied or electronic, at more than one institution of learning;

E) in the case of a photocopy permission, no materials may be entered into electronic memory by User except in order to produce an identical copy of a Work before or during the academic term (or analogous period) as to which any particular permission is granted. In the event that User shall choose to retain materials that are the subject of a photocopy permission in electronic memory for purposes of producing identical copies more than one day after such retention (but still within the scope of any permission granted), User must notify CCC of such fact in the applicable permission request and such retention shall constitute one copy actually sold for purposes of calculating permission fees due; and

F) any permission granted shall expire at the end of the class. No permission granted shall in any way include any right by User to create a substantively non-identical copy of the Work or to edit or in any other way modify the Work (except by means of deleting material immediately preceding or following the entire portion of the Work copied).

iv) Books and Records; Right to Audit. As to each permission granted under the academic pay-per-use Service, User shall maintain for at least four full calendar years books and records sufficient for CCC to determine the numbers of copies made by User under such permission. CCC and any representatives it may designate shall have the right to audit such books and records at any time during User's ordinary business hours, upon two days' prior notice. If any such audit shall determine that User shall have underpaid for, or underreported, any photocopies sold or by three percent (3%) or more, then User shall bear all the costs of any such audit; otherwise, CCC shall bear the costs of any such audit. Any amount determined by such audit to have been underpaid by User shall immediately be paid to CCC by User, together with interest thereon at the rate of 10% per annum from the date such amount was originally due. The provisions of this paragraph shall survive the termination of this License for any reason.

b) ***Digital Pay-Per-Uses of Academic Course Content and Materials (e-coursepacks, electronic reserves, learning management systems, academic institution intranets).*** For uses in e-coursepacks, posts in electronic reserves, posts in learning management systems, or posts on academic institution intranets, the following additional terms apply:

i) The pay-per-uses subject to this Section 14(b) include:

A) **Posting e-reserves, course management systems, e-coursepacks for text-based content,** which grants authorizations to import requested material in electronic format, and allows electronic access to this material to members of a designated college or university class, under the direction of an instructor designated by the college or university, accessible only under appropriate electronic controls (e.g., password);

B) **Posting e-reserves, course management systems, e-coursepacks for material consisting of photographs or other still images not embedded in text,** which grants not only the authorizations described in Section 14(b)(i)(A) above, but also the following authorization: to include the requested material in course materials for use consistent with Section 14(b)(i)(A) above, including any necessary resizing, reformatting or modification of the resolution of such requested material (provided that such modification does not alter the underlying editorial content or meaning of the requested material, and provided that the resulting modified content is used solely within the scope of, and in a manner consistent with, the particular authorization described in the Order Confirmation and the Terms), but not including any other form of manipulation, alteration or editing of the requested material;

C) **Posting e-reserves, course management systems, e-coursepacks or other academic distribution for audiovisual content,** which grants not only the authorizations described in Section 14(b)(i)(A) above, but also the following authorizations: (i) to include the requested material in course materials for use consistent with Section 14(b)(i)(A) above; (ii) to display and perform the requested material to such members of such class in the physical classroom or remotely by means of streaming media or other video formats; and (iii) to "clip" or reformat the requested material for purposes of time or content management or ease of delivery, provided that such "clipping" or reformatting does not alter the underlying editorial content or meaning of the requested material and that the resulting material is used solely within the scope of, and in a manner consistent with, the particular authorization described in the Order Confirmation and the Terms. Unless expressly set forth in the relevant Order Conformation, the License does not authorize any other form of manipulation, alteration or editing of the requested material.

ii) Unless expressly set forth in the relevant Order Confirmation, no License granted shall in any way: (i) include any right by User to create a substantively non-identical copy of the Work or to edit or in any other way modify the Work (except by means of deleting material immediately preceding or following the entire portion of the Work copied or, in the case of Works subject to Sections 14(b)(1)(B) or (C) above, as described in such Sections) (ii) permit "publishing ventures" where any particular course materials would be systematically marketed at multiple institutions.

iii) Subject to any further limitations determined in the Rightsholder Terms (and notwithstanding any apparent contradiction in the Order Confirmation arising from data provided by User), any use authorized under the electronic course content pay-per-use service is limited as follows:

A) any License granted shall apply to only one class (bearing a unique identifier as assigned by the institution, and thereby including all sections or other subparts of the class) at one institution;

B) use is limited to not more than 25% of the text of a book or of the items in a published collection of essays, poems or articles;

C) use is limited to not more than the greater of (a) 25% of the text of an issue of a journal or other periodical or (b) two articles from such an issue;

D) no User may sell or distribute any particular materials, whether photocopied or electronic, at more than one institution of learning;

E) electronic access to material which is the subject of an electronic-use permission must be limited by means of electronic password, student identification or other control permitting access solely to students and instructors in the class;

F) User must ensure (through use of an electronic cover page or other appropriate means) that any person, upon gaining electronic access to the material, which is the subject of a permission, shall see:

- a proper copyright notice, identifying the Rightsholder in whose name CCC has granted permission,
- a statement to the effect that such copy was made pursuant to permission,
- a statement identifying the class to which the material applies and notifying the reader that the material has been made available electronically solely for use in the class, and
- a statement to the effect that the material may not be further distributed to any person outside the class, whether by copying or by transmission and whether electronically or in paper form, and User must also ensure that such cover page or other means will print out in the event that the person accessing the material chooses to print out the material or any part thereof.

G) any permission granted shall expire at the end of the class and, absent some other form of authorization, User is thereupon required to delete the applicable material from any electronic storage or to block electronic access to the applicable material.

iv) Uses of separate portions of a Work, even if they are to be included in the same course material or the same university or college class, require separate permissions under the electronic course content pay-per-use Service. Unless otherwise provided in the Order Confirmation, any grant of rights to User is limited to use completed no later than the end of the academic term (or analogous period) as to which any particular permission is granted.

v) Books and Records; Right to Audit. As to each permission granted under the electronic course content Service, User shall maintain for at least four full calendar years books and records sufficient for CCC to determine the numbers of copies made by User under such permission. CCC and any representatives it may designate shall have the right to audit such books and records at any time during User's ordinary business hours, upon two days' prior notice. If any such audit shall determine that User shall have underpaid for, or underreported, any electronic copies used by three percent (3%) or more, then User shall bear all the costs of any such audit; otherwise, CCC shall bear the costs of any such audit. Any amount determined by such audit to have been underpaid by User shall immediately be paid to CCC by User, together with interest thereon at the rate of 10% per annum from the date such amount was originally due. The provisions of this paragraph shall survive the termination of this license for any reason.

c) ***Pay-Per-Use Permissions for Certain Reproductions (Academic photocopies for library reserves and interlibrary loan reporting) (Non-academic internal/external business uses and commercial document delivery).*** The License expressly excludes the uses listed in Section (c)(i)-(v) below (which must be subject to separate license from the applicable Rightsholder) for: academic photocopies for library reserves and interlibrary loan reporting; and non-academic internal/external business uses and commercial document delivery.

i) electronic storage of any reproduction (whether in plain-text, PDF, or any other format) other than on a transitory basis;

ii) the input of Works or reproductions thereof into any computerized database;

iii) reproduction of an entire Work (cover-to-cover copying) except where the Work is a single article;

iv) reproduction for resale to anyone other than a specific customer of User;

v) republication in any different form. Please obtain authorizations for these uses through other CCC services or directly from the rightsholder.

Any license granted is further limited as set forth in any restrictions included in the Order Confirmation and/or in these Terms.

d) ***Electronic Reproductions in Online Environments (Non-Academic-email, intranet, internet and extranet).*** For "electronic reproductions", which generally includes e-mail use (including instant messaging or other electronic transmission to a defined group of recipients) or posting on an intranet, extranet or Intranet site (including any display or performance incidental thereto), the following additional terms apply:

i) Unless otherwise set forth in the Order Confirmation, the License is limited to use completed within 30 days for any use on the Internet, 60 days for any use on an intranet or extranet and one year for any other use, all as measured from the "republication date" as identified in the Order Confirmation, if any, and otherwise from the date of the Order Confirmation.

ii) User may not make or permit any alterations to the Work, unless expressly set forth in the Order Confirmation (after request by User and approval by Rightsholder); provided, however, that a Work consisting of photographs or other still images not embedded in text may, if necessary, be resized, reformatted or have its resolution modified without additional express permission, and a Work consisting of audiovisual content may, if necessary, be "clipped" or reformatted for purposes of time or content management or ease of delivery (provided that any such resizing, reformatting, resolution modification or "clipping" does not alter the underlying editorial content or meaning of the Work used, and that the resulting material is used solely within the scope of, and in a manner consistent with, the particular License described in the Order Confirmation and the Terms.

15) **Miscellaneous.**

a) User acknowledges that CCC may, from time to time, make changes or additions to the Service or to the Terms, and that Rightsholder may make changes or additions to the Rightsholder Terms. Such updated Terms will replace the prior terms and conditions in the order workflow and shall be effective as to any subsequent Licenses but shall not apply to Licenses already granted and paid for under a prior set of terms.

b) Use of User-related information collected through the Service is governed by CCC's privacy policy, available online at www.copyright.com/about/privacy-policy/.

c) The License is personal to User. Therefore, User may not assign or transfer to any other person (whether a natural person or an organization of any kind) the License or any rights granted thereunder; provided, however, that, where applicable, User may assign such License in its entirety on written notice to CCC in the event of a transfer of all or substantially all of User's rights in any new material which includes the Work(s) licensed under this Service.

d) No amendment or waiver of any Terms is binding unless set forth in writing and signed by the appropriate parties, including, where applicable, the Rightsholder. The Rightsholder and CCC hereby object to any terms contained in any writing prepared by or on behalf of the User or its principals, employees, agents or affiliates and purporting to govern or otherwise relate to the License described in the Order Confirmation, which terms are in any way inconsistent with any Terms set forth in the Order Confirmation, and/or in CCC's standard operating procedures, whether such writing is prepared prior to, simultaneously with or subsequent to the Order Confirmation, and whether such writing appears on a copy of the Order Confirmation or in a separate instrument.

e) The License described in the Order Confirmation shall be governed by and construed under the law of the State of New York, USA, without regard to the principles thereof of conflicts of law. Any case, controversy, suit, action, or proceeding arising out of, in connection with, or related to such License shall be brought, at CCC's sole discretion, in any federal or state court located in the County of New York, State of New York, USA, or in any federal or state court whose geographical jurisdiction covers the location of the Rightsholder set forth in the Order Confirmation. The parties expressly submit to the personal jurisdiction and venue of each such federal or state court.

Last updated October 2022

Figure C.0.1: License for the use of Figure 2.10.1

NTNU

Norwegian University of
Science and Technology